

Universidade Federal de Minas Gerais

Instituto de Ciências Exatas

Departamento de Química

CARLOS ALBERTO AMAYA VARGAS

**Development of Heterogeneous Catalysts Based on Porous Silica Material
and Lanthanide Ions for the Hydrolysis of Phosphodiester**

Belo Horizonte

2019

UFMG/ICEx/DQ. 1.329

T. 605

CARLOS ALBERTO AMAYA VARGAS

**Development of Heterogeneous Catalysts Based on Porous Silica Material
and Lanthanide Ions for the Hydrolysis of Phosphodiester**

Tese apresentada ao Departamento de Química do Instituto de Ciências Exatas da Universidade Federal de Minas Gerais, como requisito parcial para a obtenção do grau de Doutor em Química.

Belo Horizonte

2019

Ficha Catalográfica

V287d Vargas, Carlos Alberto Amaya
2019 Development of heterogeneous catalysts based on
T porous silica material and lanthanide ions for the
hydrolysis of phosphodiester [manuscrito] /Carlos
Alberto Amaya Vargas. 2019.
[xi], 114 f.: il.

Orientador: Tiago Antônio da Silva Brandão.
Coorientadora: Maria Helena de Araujo.

Tese (doutorado) - Universidade Federal de Minas
Gerais - Departamento de Química.
Inclui bibliografia.

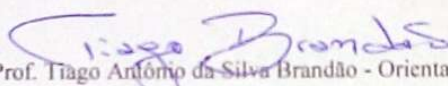
1. Química orgânica - Teses 2. Sílica - Teses 3.
Hidrólise - Teses 4. Catálise - Teses I. Brandão,
Tiago Antonio da Silva - Orientador II. Araujo, Maria
Helena de. III. Título

CDU 043

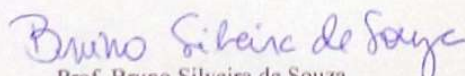
"Development of Heterogeneous Catalysts Based on Porous Silica Material and Lanthanide Ions for the Hydrolysis of Phosphodiester"

Carlos Alberto Amaya Vargas

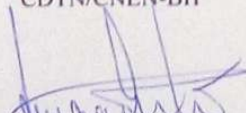
Tese aprovada pela banca examinadora constituída pelos Professores:

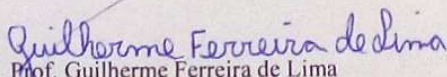

Prof. Tiago Antônio da Silva Brandão - Orientador
UFMG


Prof. Maria Helena de Araujo - Coorientadora
UFMG


Prof. Bruno Silveira de Souza
UFSC


Prof. José Domingos Ardisson
CDTN/CNEN-BH


Prof. Luciano Andrey Montoro
UFMG


Prof. Guilherme Ferreira de Lima
UFMG

Agradecimientos

Al terminar un proceso tan arduo y lleno de dificultades como la elaboración de una tesis doctoral es inevitable que te aborde un muy humano, egocentrismo, que te lleva a concentrar la mayor parte del mérito en la participación que has hecho. Sin embargo, el análisis imparcial te muestra inmediatamente que la dimensión de ese aporte hubiese sido imposible sin la participación de personas e instituciones que han facilitado las cosas para que este trabajo llegue a un feliz término. Por ello, es para mí un verdadero placer utilizar este espacio para expresar mis agradecimientos.

Debo agradecer de manera especial y sincera al Profesor Tiago A. da Silva Brandão por aceptarme para realizar esta tesis doctoral bajo su dirección. Su apoyo y confianza en mi trabajo, al igual que su capacidad para guiar ideas ha sido un aporte invaluable, no solamente en el desarrollo de esta tesis, sino también en mi formación como investigador. A pesar de las diferencias y acaloradas discusiones redundaran benéficamente tanto a nivel científico como personal.

Quiero expresar también mi más sincero agradecimiento a la profesora Maria Helena de Araújo por su importante aporte y participación activa en el desarrollo de esta tesis. Debo destacar, por encima de todo, su disponibilidad y paciencia sin las cuales este proceso no hubiera llegado a una conclusión satisfactoria. No cabe duda que su participación ha enriquecido el trabajo realizado y, además, ha significado el surgimiento de una amistad.

Entre los profesores miembros de nuestro grupo de investigación, a pesar que con todos he tenido una excelente relación, debo destacar el caso del Profesor Adolfo Henrique de Moraes Silva, para quien va un agradecimiento especial. Las escasas veces que sostuvimos discusiones de carácter científico y personal, generalmente improvisadas, se vieron claramente compensadas por la calidad de las mismas, altamente enriquecedoras. Muchas gracias.

Para mis compañeros de grupo, doctorandos/as, masters y IC, tengo sólo palabras de agradecimiento, especialmente por aquellos momentos en los que pude ser inferior a sus expectativas: fue un camino muy largo y duro en el que, algunas veces, la fijación por lograr tus objetivos te hace olvidar la importancia del contacto humano. Compañeros: Mozart, Raquel, Julia, Thais, Verônica, Aline, ¡mil y mil gracias!

Quiero expresar mi agradecimiento especial a Sami quien es mi compañera en este camino tan arduo. No existen palabras que permitan expresar a totalidad lo agradecido que estoy de haber encontrado un ser humano que me complementa de tal manera. Y, por supuesto, el agradecimiento más especial va para mi familia. Sin su apoyo, habría sido imposible llevar a cabo esta ardua travesía. A mis padres, por su ejemplo de lucha; a mi hermana Angela por su paciencia, inteligencia y generosidad y a mi hermana Natalia por su apoyo ¡por ellos y para ellos!

Finalmente, debo agradecer a la organización de estados americanos (OEA) y al grupo Coímbra, por haber financiado mis estudios doctorales otorgándome una beca a partir de la convocatoria del año 2015.

ABSTRACT

Silica is abundant and structurally malleable for numerous applications. In this work, we applied mesoporous silica and its functionalized forms for catalysis of phosphodiester hydrolysis. Hybrid materials were obtained by post-grafting with carboxyl and amine groups, which were anchor points for lanthanide (III) ions. Materials were characterized regarding their composition, morphology and properties using infrared spectroscopy, thermo gravimetric analysis (TGA), differential scanning calorimetry (DSC), elemental analysis, total-reflection X-ray fluorescence (TXRF), nitrogen adsorption, scanning and transmission electron microscopy, X-ray powder diffraction (XRD), and zeta potential. Functionalization and coordination were effective, and the hybrid material kept the mesoporous structure with small surface area reduction. The organometallic silica was an effective heterogeneous catalyst for the hydrolysis of the prototypical phosphodiester *bis*(2,4-dinitrophenyl)phosphate at different pH and 25°C. In the first use the catalytic proficiencies were between 10 to 50-fold relative to the uncatalyzed hydrolysis. All materials showed higher catalytic activity upon hydrated reuse, which was caused by structural changes on the silica surface. The reuse of PSiM-NH₂La on hydrated conditions at pH 8.1 followed a first-order rate constant with $k_{obs} = 8.4 \times 10^{-3} \text{ min}^{-1}$, corresponding to a catalytic proficiency of about 600-fold. We observed that hydration (and the hydration method) of the surface is fundamental for the catalytic properties of the material. The complete hydrolysis does not follow a simple two consecutive first-order kinetics, and we used a model that takes into account the Avrami kinetic model, which describes how solids transform from one phase (state of matter) to another at constant temperature. The phase change was characterized by X-ray powder diffraction, nitrogen adsorption, transmission electron microscopy, zeta potential, and solid-state nuclear magnetic resonance. The importance of the nature of functionalization (carboxyl and amino) was evaluated in different pH showing that BDNPP hydrolysis is accomplished in different ways but with similar catalytic proficiencies.

Keywords: Mesoporous Silica, hydrolysis, phosphodiester, Kinect, Lanthanide

RESUMO

A sílica é abundante e estruturalmente maleável para inúmeras aplicações. Neste trabalho, aplicamos a sílica mesoporosa e suas formas funcionalizadas como catalisadores na hidrólise da ligação fosfodiéster. Materiais híbridos foram obtidos por pós-funcionalização com grupos carboxila e amina, que eram pontos de ancoragem para íons lantanídeos (III). Os materiais foram caracterizados em relação a composição, a morfologia e propriedades usando espectroscopia de infravermelho, Análise termogravimétrica (TGA), calorimetria diferencial de varredura (DSC), análise elementar, a fluorescência total-reflexão de raios-X (TXRF), adsorção de nitrogênio, de e a microscopias electrónicas de transmissão e de varredura, Difração de raios X (XRD) e potencial zeta. A funcionalização e coordenação foram eficazes, e o material híbrido manteve a estrutura mesoporosa com pequena redução da área superficial. A sílica organometálica é um catalisador heterogêneo eficaz para a hidrólise de um modelo de fosfodiéster *bis*(2,4-dinitrofenil) fosfato a diferentes pH e 25 ° C. No primeiro uso, as eficiências catalíticas obtidas estão entre 10 a 50 vezes em relação à hidrólise não catalisada. Todos os materiais apresentaram maior atividade catalítica quando reutilizados em sua forma hidratada, efeito causado por alterações estruturais na superfície da sílica. A reuso de PSiM-NH₂La em condições hidratadas em pH 8,1 segue um perfil de primeira ordem com uma constante $k_{obs} = 8,4 \times 10^{-3} \text{ min}^{-1}$, o que corresponde a uma eficiência catalítica de cerca de 600 vezes. Observamos que a hidratação (e o método de hidratação) da superfície é fundamental para as propriedades catalíticas do material. A hidrólise completa não segue duas cinéticas de primeira ordem consecutivas simples, e desenvolvemos um modelo que leva em conta o modelo cinético de Avrami, que descreve como os sólidos de se converte de uma fase (estado da matéria) para outra a uma temperatura constante. A mudança de fase foi caracterizada por difração de raios-X em pó, adsorção de nitrogênio, microscopia electrónica de transmissão, potencial zeta, ressonância magnética nuclear de silício no estado sólido. A importância da natureza da funcionalização (carboxila e amino) foi avaliada em diferentes pH mostrando que a hidrólise de BDNPP é realizada por caminhos diferentes, mas com uma eficiência catalítica semelhante.

Palavras Chaves: Sílica Mesoporosa, Hidrólise, Fosfodiéster, Cinética, Lantanideo

INDEX

ABSTRACT.....	I
RESUMO.....	II
Abbreviations.....	VI
List of Figures.....	VII
List of Schemes.....	X
Lists of tables.....	XI
1. INTRODUCTION.....	1
1.1 Motivation and Goals.....	2
1.2 Literature review.....	3
1.2.1 Chemistry of phosphoesters.....	3
1.2.2 Basic concepts about the chemistry of the lanthanide series.....	10
1.2.3 Heterogeneous catalysis in the hydrolysis of phosphate esters.....	16
1.2.4 Mesoporous molecular sieves MCM-41.....	17
1.2.5 Physical Chemistry and Chemical Physics of Mesoporous Silica.....	27
2. EXPERIMENTAL SECTION.....	31
2.1 Materials.....	31
2.2 Synthetic procedures.....	31
2.2.1 Synthesis of <i>bis</i> (2,4-dinitrophenyl)phosphate (BDNPP).....	31
2.2.2 Synthesis of the non-functionalized Porous Silica Material (PSiM) used for preparing the heterogeneous catalyst.....	31
2.2.3 Functionalization of PSiM.....	32
2.2.4 Hydrolysis of the isocyanate group on the surface of the PSiM-NCO.....	34
2.2.5 Hydrolysis of the cyanate group on the surface of the PSiM-CN.....	34
2.2.6 Lanthanide (III) coordination to PSiM-NH ₂ and PSiM-COOH.....	34
2.3 Characterization.....	35
2.3.1 Infrared spectroscopy.....	35
2.3.2 Thermal Analysis.....	35
2.3.3 Elemental Analysis Carbon, Hydrogen, Nitrogen (CHN).....	35
2.3.4 Total-reflection X-ray fluorescence.....	36
2.3.5 Powder X-ray diffraction (XRD).....	36
2.3.6 Nitrogen Adsorption-Desorption at 77 K (BET analysis).....	36
2.3.7 Electron Microscopy.....	36
2.3.8 Particle size, zeta potential and conductivity.....	37
2.3.9 Solid-State Nuclear Magnetic Resonance (NMR).....	37
2.4 Kinetic studies.....	37

2.4.1	Catalyst Reuse	40
2.4.2	Activation (hydration) of PSiM	41
RESULTS AND DISCUSSION		42
3	PSiM functionalized with amino groups and adorned with La (III)	43
3.1	Characterization of the PSiM and its amino and lanthanum forms.....	43
3.1.1	Infrared spectroscopy	43
3.1.2	Thermo gravimetric analysis (TGA)	45
3.1.3	Differential Scanning Calorimetry (DSC)	46
3.1.4	Elemental analysis.....	49
3.1.5	Total-reflection X-ray fluorescence (TXRF).....	49
3.1.6	Determination of the surface area by adsorption of N ₂ using the BET method	51
3.1.7	Scanning electron microscopy	53
3.1.8	Transmission electron microscopy.....	56
3.1.9	X-ray Power Diffraction (XRD)	57
3.1.10	Zeta potential and conductivity	58
3.2	Kinetic studies	59
3.2.1	Evaluation of the catalytic activity of the PSiM hybrid material on the hydrolysis of BDNPP 60	
3.2.2	Evaluation of the reusability of PSiM-NH ₂ La on the hydrolysis of BDNPP	62
3.2.3	pH-rate profile for the catalytic activity of PSiM-NH ₂ La on the hydrolysis of BDNPP 64	
3.3	Conclusion	67
4	Structural changes in the PSiM structure and its role to catalysts.	68
4.1	Structural characterization.....	69
4.1.1	X-ray Power Diffraction (XRD) in function of time	69
4.1.2	Transmission electron microscopy.....	70
4.1.3	Determination of the surface area by adsorption of N ₂ using the BET method	72
4.1.4	Solid-State Nuclear Magnetic Resonance (NMR).....	73
4.1.5	Zeta potential	75
4.2	Kinetic studies	75
4.2.1	Use and reuse of PSiM as catalyst on the hydrolysis of BDNPP.....	76
4.2.2	Activation of PSiM prior its use on the hydrolysis of BDNPP	77
4.2.3	Activation of the PSiM on the flow system	78
4.2.4	Development of a mathematic model to describe the effect of the structural changes of PSiM-NH ₂ La on the hydrolysis of BDNPP	80
4.3	Conclusion	85

5	PSiM functionalized with carboxyl group adorned with Ln (III).....	85
5.1	Characterization of the PSiM-COOH and PSiM-COOLn.....	86
5.1.1	Infrared spectroscopy	86
5.1.2	Thermo gravimetric analysis (TGA)	87
5.1.3	Elemental analysis.....	89
5.1.4	Total-reflection X-ray fluorescence (TXRF).....	89
5.1.5	Determination of the surface area by adsorption of N ₂ using the BET method	91
5.1.6	Transmission electron microscopy for the PSiM-COOLn.....	92
5.1.7	Zeta potential and particles size.....	93
5.2	Catalytic studies	94
5.2.1	Reuse and thermal resilience of PSiM-COOLn on the hydrolysis of BDNPP	96
5.2.2	pH-rate profile for the catalytic activity of PSiM-COOLn on the hydrolysis of BDNPP 97	97
5.3	Conclusion	100
6	GENERAL CONCLUSION AND PERSPECTIVES.....	101
7	References	103

Abbreviations

BDNPP	<i>bis</i> (2,4-dinitrophenyl)phosphate
BET	Brunauer-Emmett-Teller
CTAB	Cetyltrimethylammonium bromide
DLS	Dynamic light scattering
DNP	2,4 dinitrophenolate
DNPP	(2,4-dinitrophenyl)phosphate
DSC	Differential Scanning Calorimetry
EDX	Energy-dispersive X-ray spectroscopy
<i>et al.</i>	And others
<i>f</i>	Catalytic factor
g	grams
h	Hour
<i>k_{obs}</i>	Reaction rate constant observed
MCM-41	Mobil Composition of matter No. 41
min	Minutes
NMR	Nuclear Magnetic Resonance
PSiM	Porous Silica Material
PSiM-COOEu	Porous Silica Material functionalized with carboxyl groups adorned with Europium (III)
PSiM-COOH	Porous Silica Material functionalized with carboxyl groups
PSiM-COOHo	Porous Silica Material functionalized with carboxyl groups adorned with Holmium (III)
PSiM-COOLa	Porous Silica Material functionalized with carboxyl groups adorned with Lanthanum (III)
PSiM-NH₂La	Porous Silica Material functionalized with amino groups adorned with Lanthanum (III)
PSiM-NH₃⁺	Porous Silica Material functionalized with amino groups
SEM	Scanning electron microscopy
TEM	Transmission electron microscopy
TEOS	Tetraethyl orthosilicate
TGA	Thermo Gravimetric Analysis
TXRF	Total-reflection fluorescence
XRD	X-ray power diffraction
ZP	Zeta potential

List of Figures

Figure 1. 1. DNA and RNA structures depicting the phosphodiester bond in their backbones.	4
Figure 1. 2. Model for the dinuclear iron center of mammalian PAP's. Adapted from Wang et al. ³⁷	9
Figure 1. 3. Proposed catalytic mechanism of 5'-NT showing an in-line transfer of the phosphoryl group of the substrate to the nucleophile: (a) Michaelis complex,(b) transition state, and (c) primary product complex. ⁴⁰	10
Figure 1. 4. Modeling of the tetrahedral Zn ²⁺ complex showing the metal interaction with the oxygen of the (PO ₂ ⁻) moiety during the in-line attack by the ribose 2'-oxygen on the phosphorus atom. Modeling of the La ³⁺ complex that due to the length of the bonds and the lack of geometrical constraints is capable of complexing with both (PO ₂ ⁻) oxygens as well as to both ground state and the incipient phenoxide in the transition state. Adapted from Blaskó and Bruice. ²⁶	13
Figure 1. 5. Structures of tris-(hydroxymethyl)aminomethane (Tris) derivatives commonly used in the formation of stable complexes with lanthanide ions.	14
Figure 1. 6. Representation of the mechanism proposed by Beck et al. ¹⁰ Image adapted from Gibson. ⁷³	18
Figure 1. 7. TEM images of MCM-41 showing pore size of the materials made with (a) C-8 surfactant or (b) C-16 surfactant. Adapted from Beck et al. ¹⁰	18
Figure 1. 8. Possible applications of MCM-41: drug delivery system, ^{75,76} humidity sensors, ⁷⁷ and enzyme immobilization. ⁷⁸	19
Figure 1. 9. a) TEM image of the honeycomb structure of MCM-41 and a schematic representation of the hexagonal shaped one-dimensional pores. b) Typical XRD pattern of MCM-41 with Miller indices of the diffraction planes. Inset: enlargement of the XRD pattern. The corresponding d-spacings: (100) = 3.90 nm, (110) = 2.26 nm, (200) = 1.95 nm, and (210) = 1.48 nm. Adapted from Meynen et al. ⁷⁹	20
Figure 1. 10. The IUPAC classification of adsorption isotherms showing both the adsorption and desorption pathways. ⁸²	21
Figure 1. 11. Nitrogen sorption isotherm for MCM-41. Adapted from Zhao and Lu. ⁸³	21
Figure 1. 12. a) Scanning electron micrograph of MCM-41 spheres prepared with n-hexadecylpyridinium chloride. Adapted from Grün et al. ⁸⁵ b), c), d) Transmission electron microscopy images of the MCM-41 mesoporous silica. Adapted from Pasqua et al. ⁸⁶	23
Figure 1. 13. ²⁹ Si CP/MAS NMR spectra for template-extracted Si- MCM-41 (A), partially silylated Si-MCM-41 with a 43% coverage (B), and fully silylated MCM-41 (C). Adapted from Zhao and Lu ⁸³	24
Figure 1. 14. Thioalkylated MCM-41 for mercury removal from wastewater. A) Close-packed material at 75% surface coverage and B) containing mercury. Adapted from Feng et al. ⁹⁰	25
Figure 1. 15. Preparation of surface carboxyl functionalized MSNs. Adapted from Ray et al. ⁹⁹	26
Figure 1. 16. Representation of the degradability of large-pore silica-iron oxide NPs in water and in FBS (a). TEM images of the nanovectors before (b) and after three days of dispersion in water (c) or in FBS. Adapted from Omar et al. ¹⁰³	26
Figure 1. 17. Representation of the structural evolution of water molecules as the adsorbed layer thickness rises with relative humidity (RH). The icelike structure grows up to 3 molecular layers thick as RH increases from 0 to 30%. In the RH range from 30 to 60%, the icelike structure continues to grow while liquid structure begins to form. In this transitional RH region, approximately one molecular layer grows. Further increase in the RH above 60% causes water to adsorb in the liquid configuration (--- hydrogen bonds, -; covalent bonds). Adapted from Asay and Kim. ¹¹²	28
Figure 1. 18. Illustration of the base and degraded structures of silica NPs along with the mechanism and regulating factors of the degradation. Adapted from Croissant et al. ⁹⁶	29
Figure 1. 19. Generic mechanisms for the formation and dissolution of silica. a) Condensation mechanism of an alkoxy silane using acidic catalyst, b) Hydrolysis mechanism of an alkoxy silane using acidic catalyst, c) and d) Hydrolysis and condensation mechanisms of an alkoxy silane using basic catalyst. Adapted from Alothman. ⁸⁰	30

Figure 2. 1. Apparatus used for synthesis of PSiM	32
Figure 2. 2. Apparatus used for the functionalization of PSiM.....	33
Figure 2. 3. System 1 (reactor) used to monitor the hydrolysis of BDNPP in the presence of the silica materials (PSiM, PSiM-NH ₃ ⁺ and PSiM-NH ₂ La).	38
Figure 2. 4. System 2 (reactor) used to monitor the hydrolysis of BDNPP in presence of the silica materials (PSiM-COOH and PSiM-COOHln).	39

Figure 3. 1. The FT-IR spectra of PSiM (black), isocyanate(green) and amino(red) functionalized forms and its lanthanide complexes (blue). a) FT-IR spectra region of 4000-400 cm ⁻¹ , b) Close-up of FT-IR spectra at 4000-2600 cm ⁻¹ showing the peak at 2950 cm ⁻¹ (asymmetric and symmetric stretching vibrations of methylene groups), c) Close-up of FT-IR spectra at 1800-1300 cm ⁻¹ showing the peak at 1570 cm ⁻¹ (the N-H bending peak).	44
Figure 3. 2. Typical IR Absorption bands for the different silanol types present on the PSiM.....	44
Figure 3. 3. Thermograms of PSiM (black), PSiM-NH ₃ ⁺ (red), and PSiM-NH ₂ La (blue) in air. The different regions indicated correspond to (1) water desorption, (2) degradation of the organic moiety when present, and (3) condensation of silanol groups.....	45
Figure 3. 4. Differential scanning calorimetry curves for PSiM (black), PSiM-NH ₃ ⁺ (red), and PSiM-NH ₂ La. The different regions indicated correspond to (1) water desorption, (2) degradation of the organic moiety when present, and (3) condensation of silanol groups.	46
Figure 3. 5. Derivate of the TGA (dotted line) and DSC (solid line) curves of PSiM.....	47
Figure 3. 6. Derivate of the TGA (dotted line) and DSC curves (solid line) of PSiM-NH ₃ ⁺	48
Figure 3. 7. Derivate of the TGA (dotted line) and DSC curves (solid line) of PSiM-NH ₂ La.....	48
Figure 3. 8. a) Simplified arrangements used for conventional XRFA (up) and for TXRF (down). Adapted from Klockenkämper and Bohlen ¹³² . b) Total-reflection X-ray fluorescence of PSiM-NH ₂ La.....	50
Figure 3. 9. Nitrogen adsorption-desorption isotherms (a) and pore size distribution by the DFT method (b) for PSiM before and after modification and attachment of the La ³⁺ ion. In black the base material PSiM, in red the modified PSiM-NH ₃ ⁺ , and in blue the PSiM-NH ₂ La.....	52
Figure 3. 10. Secondary electrons SEM images (SE) of a) PSiM, b) PSiM-NH ₃ ⁺ , and c) PSiM-NH ₂ La.	54
Figure 3. 11. Energy-dispersive X-ray spectrum for: a) PSiM, b) PSiM-NH ₃ ⁺ , and c) PSiM-NH ₂ La.....	55
Figure 3. 12. Transmission electron microscopy (TEM images) a) and b) PSiM, c) and d) PSiM-NH ₂ La.....	56
Figure 3. 13. XRD diffractograms for PSiM and its functionalized forms PSiM-NH ₃ ⁺ and PSiM-NH ₂ La.	57
Figure 3. 14. Successive spectra as a function of the time for the kinetics of bis(2,4-dinitrophenyl) phosphate (BDNPP) cleavage in the presence of PSiM-NH ₂ La at pH 8.14 and 25 °C, using reactor 1 (Figure 2.3).....	60
Figure 3. 15. Absorbance at 360nm as a function of time for the hydrolysis reaction of BDNPP in the presence of PSiM (black), PSiM-NH ₃ ⁺ (red), and PSiM-NH ₂ La (blue) at pH 8.14 and 25 °C, using reactor 1 (Figure 2.3).	61
Figure 3. 16. Absorbance at 360nm as a function of time for hydrolysis of BDNPP in the presence of PSiM-NH ₂ La at pH 8.14 and 25 °C, using reactor 1(Figure 2.3).....	63
Figure 3. 17. Bar diagram representing the rate constants for the hydrolysis of BDNPP in the presence of PSiM-NH ₂ La at pH 8.14 and 25°C (table 3.6) obtained for each use and reuse (cycle).	64
Figure 3. 18. Absorbance at 360nm as a function of time for the hydrolysis of BDNPP in the presence of PSiM-NH ₂ La at different pHs, using reactor 1(Figure 2.3).	65
Figure 3. 19. pH-Rate profile for bis-(2,4-dinitrophenyl) phosphate (BDNPP) cleavage in absence (Δ) and presence (■) of PSiM-NH ₂ La at 25 °C. Kinetic data in absence of the catalyst were taken from Farber and Bunton. ¹²⁵	66

Figure 4. 1. Absorbance at 360nm as a function of time for the hydrolysis reaction of BDNPP in the presence of PSiM (black), and PSiM-NH ₂ La (blue) at pH 8.14 and 25 °C, using reactor 1(Figure 2.3). The two different stages on the reaction rate are divided by the red dashed line ≈ 1500 min.....	68
Figure 4. 2. Powder X-ray diffraction pattern of the recover at different hydration times and used as catalyst on the hydrolysis of BDNPP(8000 min).	69

Figure 4. 3. XRD for PSiM-NH ₂ La before and after its use in the hydrolysis of BDNPP.	70
Figure 4. 4. Transmission electron microscopy (TEM) at different reaction times a) PSiM 160 min, b) PSiM 1230 min, c) PSiM 2560 min, d) PSiM 8000 min, e) PSiM-NH ₂ La 0 min and f) PSiM-NH ₂ La 8000 min.	71
Figure 4. 5. Nitrogen adsorption-desorption isotherms for PSiM (black) and PSiM-NH ₂ La (blue) as-synthesized and recovered after the hydrolysis of BDNPP at pH 8.0 and 25°C.	72
Figure 4. 6. Solid-state MAS ²⁹ Si-NMR spectra for PSiM before (a) and after (b) use as catalyst on the hydrolysis of BDNPP at pH 8.0 and 25°C.	74
Figure 4. 7. Zeta potential as function of time for the PSiM (a) and the PSiM-NH ₂ La (b) at pH 8.0 and 25°C 75	75
Figure 4. 8. Absorbance at 360nm as a function of time for the hydrolysis of BDNPP in the presence of PSiM at pH 8.0 and 25 °C, first and second uses using reactor 1 (Figure 2.3).	77
Figure 4. 9. Kinetic profiles for the hydrolysis of BDNPP [12.5 mM] using a previous hydrated PSiM (30mg, on a 20 mL buffer solution by 1500 min) in the absence and presence of 2.0 mmolL ⁻¹ phosphate ion (Pi) at pH 8.0 and 25°C using reactor 2 (Figure 2.4).	77
Figure 4. 10. Kinetic profile for the hydrolysis of BDNPP using PSiM hydrated on flow reactor 2(Figure 2.4) at pH 8.0 and 25°C.	79
Figure 4. 11. Absorbance at 360nm as a function of time for the hydrolysis reaction of BDNPP in the presence of PSiM-NH ₂ La pH 8.14 and 25 °C, showing the fit obtained using the Avrami equation and the parameters shown in Table 4.5.	83

Figure 5. 1. The FT-IR spectra of PSiM in black, functionalized with cyano and carboxyl acid groups in green and red, respectively, and the lanthanide complex with carboxyl groups in blue.	86
Figure 5. 2. a) TGA and b) first derivate of TGA for PSiM (black), PSiM-CN (green), PSiM-COOH (blue), and PSiM-COOLa (red).	88
Figure 5. 3. Total-reflection X-ray fluorescence spectra of PSiM-COOLa (a), PSiM-COOEu (b), and PSiM-COOHo (c).	90
Figure 5. 4. Nitrogen adsorption-desorption isotherms for PSiM-COOLn as synthesized.	91
Figure 5. 5. Transmission electron microscopy (TEM) for A) PSiM-COOLa, B) PSiM-COOEu, and C) PSiM-COOHo.	92
Figure 5. 6. Zeta potential and particle size as a function of pH for PSiM and its functionalized forms at 25°C. Measured in different buffer solutions (0.1 mol L ⁻¹) as a dispersion of 1 mg mL ⁻¹ of material.	94
Figure 5. 7. Successive UV-Vis spectra over time for BDNPP hydrolysis catalyzed by PSiM-COOH and PSiM-COOLn.	95
Figure 5. 8. Absorbance at 360 nm versus time for first use of the materials (PSiM-COOLn) on the BDNPP hydrolysis, at pH 8.0 and 25 °C.	96
Figure 5. 9. Rate constants obtained for each use using PSiM-COOLn on the hydrolysis of BDNPP, at pH 8.0 and 25 °C.	97
Figure 5. 10. pH-Rate profile for bis(2,4-dinitrophenyl)phosphate (BDNPP) hydrolysis in the presence of PSiM-COOH and PSiM-COOHln at 25 °C.	99
Figure 5. 11. Proposed species for the BDNPP cleavage by PSiM-COOLn at different pH below and above pH 9.	99

List of Schemes

Scheme 1. 1. Phosphoric acid and corresponding ester structures (Mono, di and tri).....	3
Scheme 1. 2. Associative (A) and dissociative (B) mechanisms for the nucleophilic substitution in phosphoester.	5
Scheme 1. 3. Common types of catalytic mechanisms for the hydrolysis of phosphodiester by metals. ...	6
Scheme 1. 4. Binuclear metal complex activation for hydrolysis of phosphodiester.	6
Scheme 1. 5. Structures of bis(n-hydroxyquinoline) phosphate, where n=8 (a) and n=6 (b).....	7
Scheme 1. 6. Stabilization of the hydroxyquinolate leaving group due to the coordination of the metal.	7
Scheme 1. 7. Possible lanthanum ions complexes involved in activation of nucleophile and leaving group in the cleavage of (8-hydroxy-2-quinolyl)methyl(8-hydroxy-2-quinolyl)methylphosphonate.....	8
Scheme 1. 8. a) Mimetic model of RNA. b) Mechanism proposed for the metal ion catalytic intramolecular transesterification by Zn ²⁺ . c) Model for lanthanum ion interaction during catalysis. ³³	8
Scheme 1. 9. Formation of active catalytic complex between La ³⁺ and H ₂ O ₂	15
Scheme 1. 10. Mechanistic possibilities for the role of lanthanide peroxide complexes in the hydrolysis of phosphate esters.	15
Scheme 1. 11. Methanolysis(a) and hydrolysis (b) of both methyl paraoxon (R=CH ₃) and PNPDP (R=phenyl) in the presence of UIO-66 (Metal organic framework made up with Zr(IV)). Adapted from Katz et al. ⁷¹	16
Scheme 1. 12. Stages to generate the active Cu(II) complex supported on regular silica: i, [RhCl(PPh ₃) ₃], toluene, reflux, 3 days; ii, C ₂ H ₄ , [RhCl(PPh ₃) ₃], toluene, 25 °C, 15 h; iii, Cu(NO ₃) ₂ (aq). Adapted from Bodsgard et al. ⁶⁷	17
Scheme 2. 1. Synthesis of bis(2,4-dinitrophenyl)phosphate (BDNPP).	31
Scheme 2. 2. Synthesis of PSiM-NCO and PSiM-CN from non-functionalized PSiM.	33
Scheme 2. 3. Hydrolysis of isocyanate on PSiM-NCO.	34
Scheme 2. 4. Hydrolysis of cyano group on PSiM-CN.	34
Scheme 2. 5. Lanthanide (III) coordination to the modified PSiM-NH ₃ ⁺ and PSiM-COOH.	35
Scheme 2. 6. Hydrolysis reaction of bis(2,4-dinitrophenyl) phosphate (BDNPP).	37
Scheme 3. 1. Schematic representation of the dehydroxylation processes of SiOH groups in PSiM from two different types of silanol groups. Adapted from Zhao et al. ¹³¹	47
Scheme 3. 2. Hydrolysis reaction of BDNPP, showing the representation used in the analysis.	59
Scheme 3. 3. Proposed mechanism for bis-(2,4-dinitrophenyl) phosphate (BDNPP) cleavage by PSiM-NH ₂ La.	66
Scheme 4. 1. Hydroxylation processes during which new silanol groups are generated.....	73
Scheme 4. 2. Hydrolysis reaction of BDNPP, showing the representation used in the analysis.	82

Lists of tables

Table 1. 1. Typical lanthanide abundance in ores, ^a Adapted from Cotton. ⁴⁶	11
Table 2. 1. Buffer solution used in the kinetic studies.....	40
Table 2. 2. Typical intervals used to set up the spectra acquisition in the kinect experiment.....	40
Table 3. 1. Percentages from elemental analysis for PSiM and its functionalized forms.	49
Table 3. 2. Amounts of La determined in PSiM-NH ₂ La (triplicate) using TXRF	50
Table 3. 3. Surface area values obtain of the different samples of PSiM.	51
Table 3. 4. Zeta potential and results for the PSiM and its functionalized forms in water at 25°C.....	58
Table 3. 5. Kinetic parameters for cleavage of bis(2,4-dinitrophenyl) phosphate (BDNPP) in absence and presence of PSiM and its functionalized forms. The catalytic factor (f) is calculated in relation to the spontaneous hydrolysis. ¹²⁵	61
Table 3. 6. Kinetic parameters for cleavage of bis(2,4-dinitrophenyl) phosphate (BDNPP) in the presence of PSiM-NH ₂ La at pH 8.14 and 25 °C. The catalytic factor (f) is calculated in relation to the spontaneous hydrolysis (table 3.5).	63
Table 3. 7. Kinetic parameters for cleavage of bis-(2,4-dinitrophenyl) phosphate (BDNPP) in the presence of PSiM-NH ₂ La at different pH and 25 °C.	65
Table 4. 1. Structural parameters determined from XRD data (Figure 4.2 and Figure 4.3).	70
Table 4. 2. Surface area, Micropore area and D _p for PSiM and PSiM-NH ₂ La at different reaction times as measured from the adsorption-desorption of N ₂ at 77 K.	72
Table 4. 3. Kinetic parameters for cleavage of bis(2,4-dinitrophenyl) phosphate (BDNPP) in the presence of PSiM at pH 8.0 and 25 °C. The catalytic factor (f) is calculated in relation to the spontaneous hydrolysis (table 3.5).	76
Table 4. 4. Kinetic parameters for cleavage of bis(2,4-dinitrophenyl) phosphate (BDNPP) in the presence of hydrated PSiM in absence and presence of 2.0 mmol L ⁻¹ phosphate ion at pH 8.0 and 25 °C. The catalytic factor (f) is calculated in relation to the spontaneous hydrolysis (table 3.5).	78
Table 4. 5. Kinetic parameters found for the data fit using the modify consecutive kinetic model (equation 4.15).	83
Table 5. 1. Mass percentages from elemental analysis for PSiM and its functionalized forms	89
Table 5. 2. Amounts of Ln in PSiM-COOLn (triplicate) as determined using TXRF	90
Table 5. 3. Structural properties of PSiM-COOLn, as determined from the adsorption-desorption of N ₂ at 77 K).....	91
Table 5. 4. Kinetic parameters for reuse of PSiM-COOLn on the cleavage of bis-(2,4-dinitrophenyl) phosphate (BDNPP), pH 8.0 at 25 °C. The catalytic factor (f) was calculated in relation to the uncatalyzed reaction. ¹²⁵	97
Table 5. 5. Observed rate constants for BDNPP hydrolysis in the presence of PSiM-COOH and its lanthanide forms at different pH (buffer solution 0.1 mol L ⁻¹). The catalytic factor in parenthesis (f) was calculated in relation to the uncatalyzed reaction. ¹²⁵	98

1. INTRODUCTION

Phosphorus is a vital element in the composition of the living matter. Although, the human body contains only 1% in average of this element, this small amount is important for many cellular process.¹ For example, phosphodiester bonds form the backbone of DNA and play an important role for storage and transmission of the genetic information. The importance of these processes for maintenance of life are parallel with the formidable stability of phosphodiester bonds, which the estimated half-lives are over 30 million years.² Indeed, in order to life evolve and survive, nucleases are required to read or copy the genetic information precisely and within a lifespan. Another example is storage and transfer of energy in all organisms, which depends on the hydrolysis of adenosine triphosphate (ATP), catalyzed by ATPase's. This reaction is ubiquitous for all living forms to drive other chemical reactions that would not occur spontaneously. In addition, a variety of organic phosphates with P-N bonds (e.g. phosphocreatine, phosphoarginine and phosphohistidine) and several inorganic polyphosphates are found in biology.³

Phosphoesters also possess many technological and practical applications like plasticizers, reagents in the preparation of organophosphorous polymers, chelating agents for extraction of heavy metals (cations), insecticides, pesticides, and even toxic compounds used as warfare weapons.⁴ Sarin gas is a representative example of toxic phosphoesters developed by German scientists in the 1930's as an attempt for improvement of pesticides. However, due to its high nerve toxicity, Sarin and similar compounds, Tabun and Soman, were incorporated into artillery shells. Although, Germany did not use them against Allied targets in World War II. Many claims that the Nazis thought it was too extreme to be used.

Not surprisingly organophosphate pesticides are among important causes of severe toxicity and death from acute poisoning worldwide, representing more than 200,000 deaths/year in emergent countries.^{5,6} Therefore, accumulation of organophosphate pesticides in the environment is an important public health problem. Although, products from hydrolysis of these compounds are usually less harmful for humans and other mammals.

Due to the biological importance and health implications of phosphoesters, great efforts were made in the past decades to understand its reactivity (conditions, aspects, mechanism, etc.) and roles in chemistry and biology. Several studies were driven to develop efficient materials to hydrolyze phosphoester bonds either through homogeneous or heterogeneous conditions.^{7,8} Herein, the development of heterogeneous systems with high catalytic activity and easy recover was envisaged by us and others.^{4,9} The Mobil Composition of matter No. 41 (MCM-

41) is a porous silicate that enlists all properties above and was selected for this work.^{10,11} We anticipate that our results show that this material has good catalytic properties by itself, which were improved by functionalization of the surface silanols with organic ligands and coordination with lanthanide ions. Our interest in these metals is supported by the fact that lanthanide ions have shown excellent catalytic efficiency in nucleophilic substitutions and hydrolytic reactions of phosphoesters,^{12,13} either as free cations or associated with nucleophilic species resulting in synergic effects in the hydrolysis rate.^{12,14} Finally, it is important to mention that these new lanthanide based silica materials were developed to circumvent the formation of insoluble lanthanide hydroxides that show lower catalytic capacities in relation to free ions.

1.1 Motivation and Goals

Porous silica materials (PSiM) are versatile for applications in different fields. The inner characteristics of the surface can be modified by functionalization with organic groups, which may be adorned with lanthanides. This work evaluates the effect of two different functional groups (amine and carboxyl) on the physical and chemical properties of the material before and after incorporation of lanthanide ions. These ions were added to the surface in order to increase its Lewis acid capacity for catalytic purposes. Hydrolysis of phosphodiester was subject to catalysis by the porous silica materials, because these reactions show many biological and environmental implications. Understanding the chemical factors that affect the catalytic activity of the porous silica material is one of the major motivations of this work, which is particularly interesting due to the lack of understanding about the physical and chemical factors that modulate catalysis in materials. We also look to understand the effect of chemical modifications that may occur in the structure of the catalyst during its use, which may affect its catalytic properties in a positive or negative way.

Therefore, the main goal of this doctoral thesis was to understand the effect of porous silica materials as-synthesized or functionalized to catalysis of phosphodiester hydrolysis. We look to establish new relationships between the physical-chemical properties of the material and its effect on catalysis. These are the specific goals:

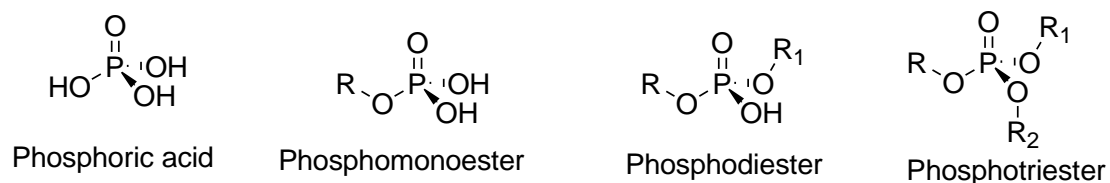
- I. Synthesis of porous silica material functionalized with amine and carboxyl groups to be adorned with lanthanide ions (La^{3+} , Eu^{3+} , and Ho^{3+});
- II. Characterize the physical and chemical properties of the synthesized materials by different analytical techniques;

- III. Evaluation of the catalytic effects of PSiM, PSiM-NH₂, PSiM-NH₂La, PSiM-COOH, PSiM-COOLa, PSiM-COOEu and PSiM-COOHo on the hydrolysis of *bis*(2,4-dinitrophenyl)phosphate (BDNPP) in aqueous solution at different pHs at 25°C;
- IV. Evaluation of structural parameters on catalysis;
- V. Analysis of different factors that modulate the catalytic properties of the material, such as: previous activation and inner stability of the material, functionalization, nature of the lanthanide ion;
- VI. Develop of a mathematical model to fit the kinetic profile for the hydrolysis reaction;
- VII. Contribute with new observations for the available literature devoted to the development of new catalysts and their ideal conditions of use.

1.2 Literature review

1.2.1 Chemistry of phosphoesters

Phosphoric acid can be derivatized to give three different types of phosphate esters (Scheme 1.1), mono-, di- and tri- substituted. Mono and di-phosphoesters possess hydroxyl groups that confer functionalities and properties of monoprotic and diprotic acids, which may afford species with different reactivities according to the pH.¹⁵



Scheme 1. 1. Phosphoric acid and corresponding ester structures (Mono, di and tri).

These compounds have many applications in chemistry as plasticizers, metal chelates, flame retardants, and pesticides, with also important implications in biology. Phosphomonoesters and phosphodiester are ubiquitous living systems. Phosphomonoesters play important roles in the control of the biological activity, while phosphodiesters form DNA and RNA backbones (Figure 1.1). The stability of this bond is remarkable. Hydrolysis of dialkylphosphate esters DNA models under physiological conditions exhibit an estimated half-life time of about 30 million years. Even for RNA type esters, which the 2'-hydroxyl group offers an intramolecular nucleophile and a faster phosphodiester bond cleavage, the half-life time is over 100 years. Many studies have been made to understand the mechanism of these reactions under spontaneous and catalyzed conditions.^{16,17} Several of such studies rely on enzymes responsible to hydrolyze the phosphoester bond. Mechanisms and strategies for P-O bond cleavage will be presented in the next sections.

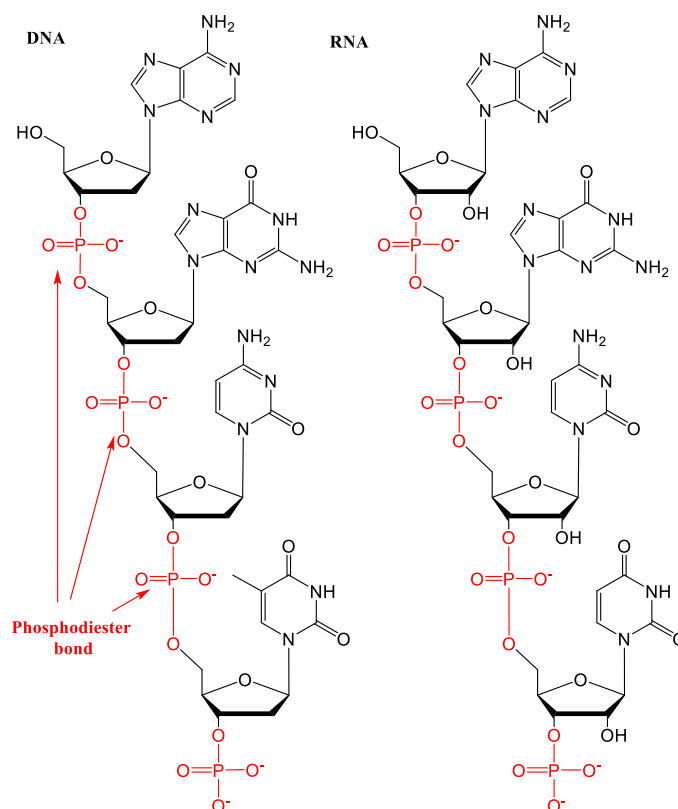
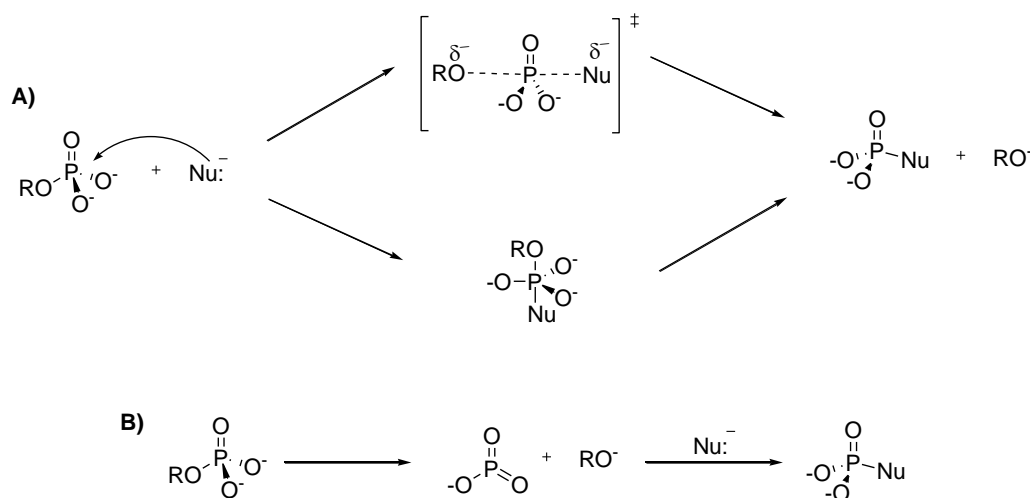


Figure 1. 1. DNA and RNA structures depicting the phosphodiester bond in their backbones.

1.2.1.1 Mechanism of phosphate ester hydrolysis

Enzyme catalyzed reactions of phosphoesters always occur with P-O cleavage, but in water, depending on the conditions, the hydrolysis may involve P-O or C-O cleavages. Several reviews are available on the mechanism for the nucleophilic substitution in phosphoester.^{18,19,20,21} Given its tetrahedral structure (Scheme 1.1 and 1.2), phosphoesters undergo nucleophilic attack in the phosphorus atom similarly to observed for S_N1 or S_N2 in substituted carbon atoms. Nevertheless, because phosphorus has the ability to form five bonds, reactions occur with variations regard the nucleophilic substitution known as: associative " S_N2 " or dissociative " S_N1 " (Scheme 1.2). The dissociative mechanism (Scheme 1.2B) appears in response to earlier observations for the hydrolysis of the monoanion-monoacid form of methyl phosphate. This reaction shows small entropies of activation, lack of dependence in relation to the concentration and strength of different nucleophiles, and a steep linear Brønsted relationship for free energies of activation for the hydrolysis reaction of substituted esters as a function of the conjugate acid's pK_a of the corresponding leaving group. These observations suggested a dissociative mechanism.^{18,22,23} The associative mechanism involves pentacoordinate intermediates or transition states (Scheme 1.2A) and a strong rate dependence on the strength of the

nucleophile. In summary, the dissociative mechanism proceeds via a hydrated metaphosphate ion, while an associative mechanism involves the formation of a pentacoordinated phosphorus atom.

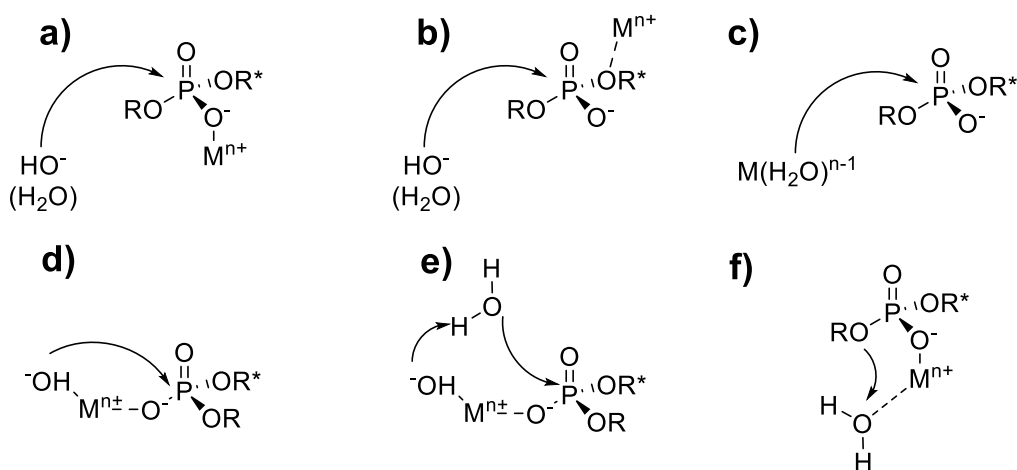


Scheme 1. 2. Associative (A) and dissociative (B) mechanisms for the nucleophilic substitution in phosphoester.

Besides the two mechanistic possibilities above, the comprehension of phosphoesters hydrolysis is complicated because may involve neutral or monoanionic or dianionic species, that can be attacked by H₂O or ⁻OH nucleophiles. In these cases, the role of charged species can be differentiated in studies over the pH, which the reaction rates are sensitive to the species distribution. Although, one should consider that kinetic studies cannot easily confront some simple hypotheses at first glance. For example, often the nucleophilic attack of a water molecule in a phosphoester is undistinguishable from a proton transfer from H₂O prior the nucleophilic attack of a hydroxide ion.

1.2.1.2 Role of the metal ions on the hydrolysis of the phosphoester bond

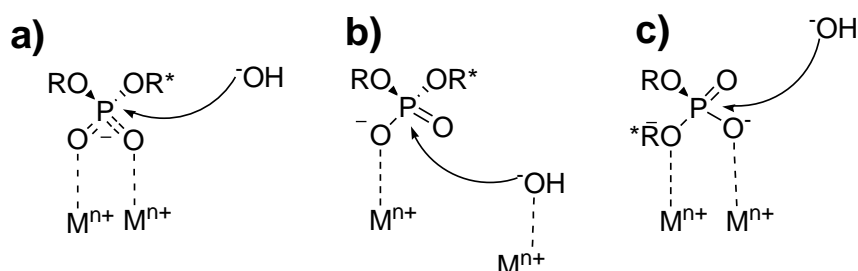
The field of metal-catalysis has experienced great development in the past decades, thanks majorly to the ability to emulate enzymatic systems.^{24,25} In the case of phosphoester cleavage it is often found that the enzymes involved in their cleavage contain metal ions. For instance, P1 nuclease contains a trimeric zinc center, other nucleases contain Mg(II), Fe(III) or Zn(II) as cofactors.²⁶ The general aspects of how the metal catalyzes the hydrolysis of phosphate ester are discussed in many reviews.^{7,16,17,27,28} The Scheme 1.3 shows the most common types of mechanism of catalysis.



Scheme 1. 3. Common types of catalytic mechanisms for the hydrolysis of phosphodiesters by metals.

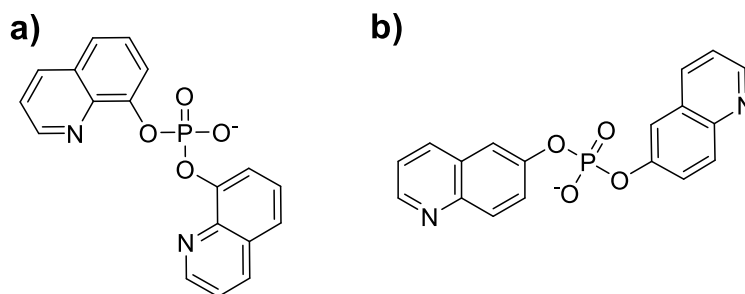
Mechanism **a** involves the coordination of the metal to the phosphoryl oxygen, leading to Lewis acid electrophilic activation of the substrate, which increases the positive charge of the phosphorus atom, and decreases the electrostatic repulsion with the nucleophile. Coordination of the leaving group, mechanism **b**, is equivalent to reduce the basicity of the leaving group ($\text{p}K_a$), speeding up the reaction. Mechanism **c** affects the activation of the nucleophile, lowering the $\text{p}K_a$ of its conjugate acid (by metal coordination), increasing the concentration of the nucleophile (more active species) in neutral solutions. A special case is when the nucleophile is water, what is referred as water activation. For example, some Co(III) complexes lowered the $\text{p}K_a$ of the coordinated water molecules by about 10 $\text{p}K_a$ units compared to free water molecules.²⁹ These three mechanisms can behave in a cooperative way, as showed in mechanism **d**. Mechanisms **a-d** are indistinguishable for kinetically labile metals as lanthanides. Mechanism **e** and **f** shows possible contributions of the general acid/base assistance,³⁰ which is usually minor for the hydrolysis of phosphodiesters.³¹

Binuclear complexes (Scheme 1.4) have received special attention because their capacity of double activation from combination of the mechanisms shown in Scheme 3. This synergism may create more active catalytic complexes.



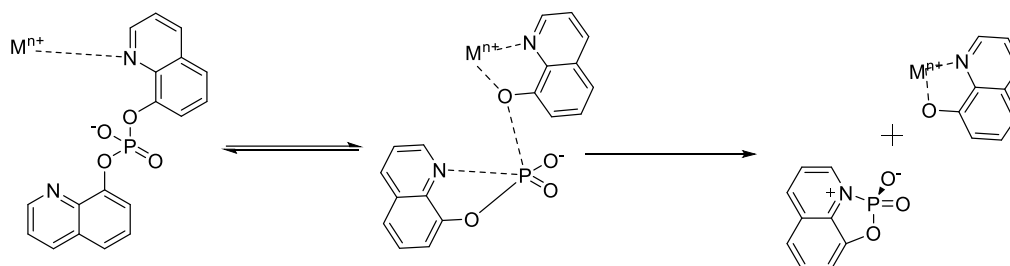
Scheme 1. 4. Binuclear metal complex activation for hydrolysis of phosphodiesters.

Substrate bearing coordinating groups have been used to gather important mechanistic information about kinetically labile metal cations. Browne and Bruice³² found that Ni^{2+} , Co^{2+} , and Zn^{2+} catalyze the hydrolysis of *bis*(8-hydroxyquinoline) phosphate (Scheme 1.5a), whereas the hydrolysis of *bis*(6-hydroxyquinoline) phosphate (Scheme 1.5b) is not affected by these metals, showing that the structure of the substrate is important.



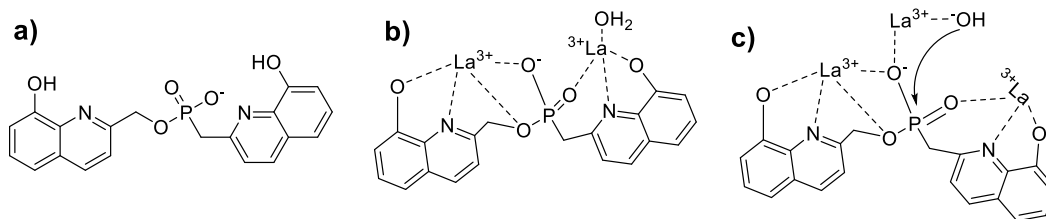
Scheme 1. 5. Structures of *bis*(*n*-hydroxyquinoline) phosphate, where *n*=8 (a) and *n*=6 (b).

The dependence on the structure can be explained because the metal assists the departure of the leaving group by coordination to the nitrogen atom (Scheme 1.6), which is placed in the opposite side of the reaction center in *bis*(6-hydroxyquinoline) phosphate.



Scheme 1. 6. Stabilization of the hydroxyquinolate leaving group due to the coordination of the metal.

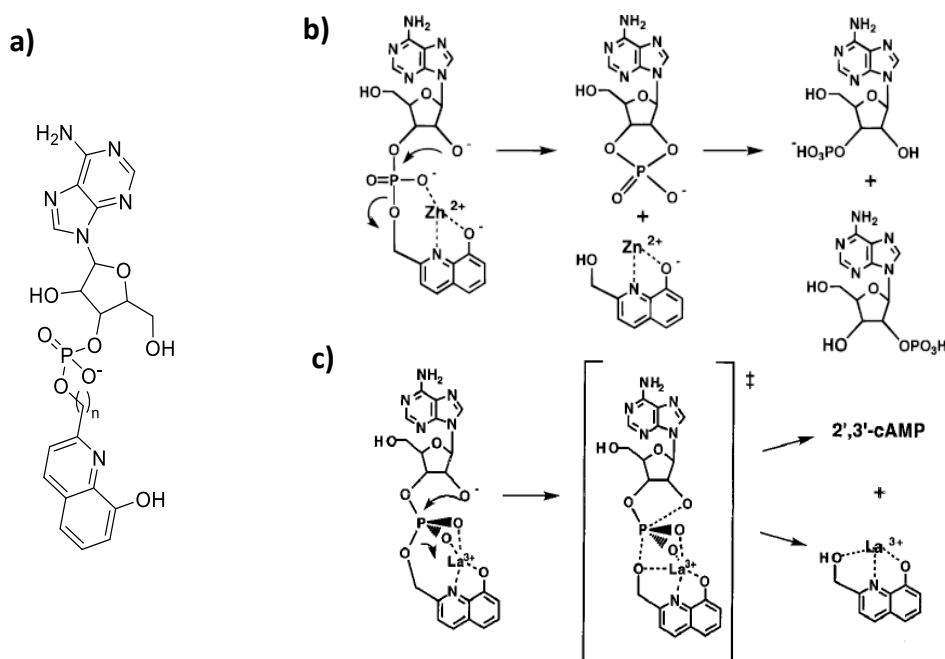
Another study showed that the same divalent cations (Ni^{2+} , Co^{2+} , and Zn^{2+}), as well as Cu^{2+} and Al^{3+} , form 1:1 complexes with (8-hydroxy-2-quinolyl)methyl(8-hydroxy-2-quinolyl)methylphosphonate (Scheme 1.7a) without any catalysis. Nevertheless, the use of La^{3+} showed a catalytic effect of $\approx 10^{13}$ -fold in the hydrolysis of this compound. Contrary to La^{3+} , the absence of catalysis by the other metals relates to their ability to chelate only the quinoline groups without cation binding to the phosphoryl oxygen atoms.¹³



Scheme 1. 7. Possible lanthanum ions complexes involved in activation of nucleophile and leaving group in the cleavage of (8-hydroxy-2-quinolyl)methyl(8-hydroxy-2-quinolyl)methylphosphonate.

The hydrolysis rate can be first, second and third order in respect to the metal.¹³ Structure 1.7b shows the model proposed to explain the second-order kinetic regime. One cation is bound to the leaving group and the other to the phosphoryl group, providing both Lewis acid and leaving group activation. The structure 1.7c suggest a role for a third metal, which provides even more Lewis acid and nucleophilic activation.

Systems that mimic biological targets have been widely studied. For example, the phosphodiester presented in Scheme 1.8a has been used as model in the metal ion catalytic cleavage of RNA.^{26,33} All the metal tested (Zn^{2+} , Mg^{2+} , Cu^{2+} , and La^{3+}) promoted the intramolecular transesterification of the substrate (scheme 1.8b).



Scheme 1. 8. a) Mimetic model of RNA. b) Mechanism proposed for the metal ion catalytic intramolecular transesterification by Zn^{2+} . c) Model for lanthanum ion interaction during catalysis.³³

The available literature for the different metal cations show that the highest activities in phosphodiester hydrolysis are observed with hard acids cations like $Zr(IV)$,³⁴ $Th(IV)$, and

Ce(IV),³⁵ which are active for the hydrolysis of quite unreactive substrates.³⁶ This information confirm that the electrophilic Lewis assistance is of major importance in the catalytic process. However, the main problem with the use of these metals is its strong tendency to form aggregates, even under physiological conditions, which precludes their application for homogeneous catalysis.

1.2.1.3 A look at Natural Enzymes

Often enzymes that catalyze the hydrolysis of phosphate esters contain metals ions in their active sites,¹⁶ and several require the presence of multiple metals. In the field of dinuclear metalloenzymes, special attention has been devoted to purple acid phosphatases (**PAP's**). These enzymes catalyze phosphate ester hydrolysis under acidic conditions (optimum pH of 4.9-6.0) and resist very well to inhibition. The dinuclear center of these enzymes requires one Fe³⁺ and the other metal is Fe²⁺ or another M²⁺ metal ion (Figure 1.2).

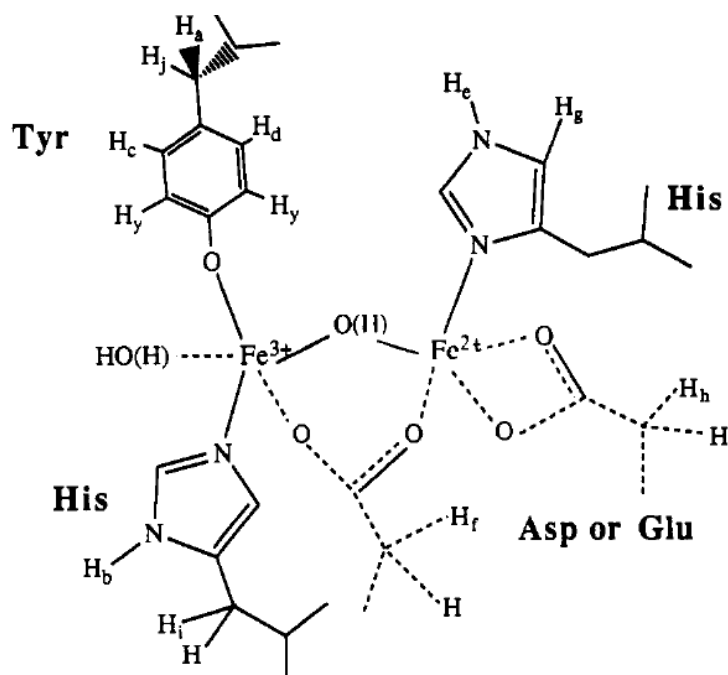


Figure 1. 2. Model for the dinuclear iron center of mammalian PAP's. Adapted from Wang et al.³⁷

There are also many enzymes activated only by one metal cation (e.g. staphylococcal nuclease), and the presence of a metal center is not always required for the hydrolysis of phosphodiester bearing β -hydroxyl groups (RNA). However, special attention has been devoted to the study of the bimetallic active center of enzymes.^{28,38} In general, the two metal ions on the active center are separated by a distance between 3-4 Å and provide Lewis acid activation to both the nucleophile and the leaving group. The metals generally found in the catalytic center of enzymes are Zn, Mg, Fe, Mn, Co, and Ni. The Lewis acid metal ability is an important aspect

for catalytic purposes, since metal ions with larger charges and smaller radii are stronger Lewis acids.³⁹

The mechanism of hydrolysis of a phosphomonoester by a bimetallic center (*E. coli* 5'-nucleotidase) is found in Figure 1.3.⁴⁰ The metals are separated by 3.5 Å with a bridging water molecule or a hydroxyl anion, and the carboxylate group of the aspartic acid. In the proposed mechanism, the Zn-1 (blue) attached to water or hydroxide is in the proper position for an attack in-line with the departure of the leaving group, while the phosphoryl group coordinated to the second metal ion Zn-2 (red) is made electrophilically active. The His117 and Arg410 also help this activation using electrostatic interactions.

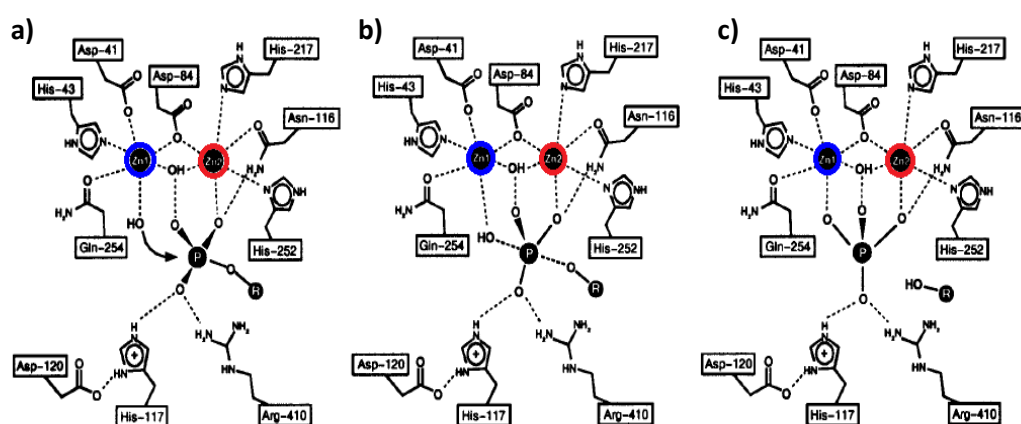


Figure 1. 3. Proposed catalytic mechanism of 5'-NT showing an in-line transfer of the phosphoryl group of the substrate to the nucleophile: (a) Michaelis complex, (b) transition state, and (c) primary product complex.⁴⁰

Although the mechanism of action of the enzymes may vary in many ways,^{41,42,43,44} all seem to work under the same principles, activation of both the leaving group and the nucleophile, and positioning the nucleophile for the attack on the phosphorus atom. These observations are supported by computer modeling studies.^{45,31} In this context, lanthanides exhibit wonderful features for development of artificial enzymes. In the following section the chemistry of these metal cations and their use in catalytic applications are addressed in depth.

1.2.2 Basic concepts about the chemistry of the lanthanide series

Lanthanide metals are obtained primarily from three minerals (Table 1.1):⁴⁶ Bastnäsite LnFCO_3 , and Monazite $(\text{Ln}, \text{Th})\text{PO}_4$, richer in lighter lanthanides, and Xenotime $(\text{Y}, \text{Ln})\text{PO}_4$, richer in heavier lanthanides. Monazite is a reddish-brown phosphate material of at least four different types depending on the relative elemental composition of the mineral. India, Madagascar, Brazil, and South Africa have large deposits of monazite sands. Bastnäsite contains either cerium,

lanthanum or yttrium as predominant rare earth elements. Bastnäsite and Monazite are the two largest sources of cerium, an important industrial metal.^{47,48}

China's southern provinces respond by more than 70% of the world reserves, mostly in the form of ionic ores. These minerals are present in granites eroded with lanthanide adsorbed on the surface of aluminum silicates, in Longnan province with lower cerium content and higher amounts of heavier lanthanides while deposits in Xunwu province are rich in lighter metals. These minerals are made of small particles, which provide an easy way to extract lanthanides. Indeed, China is the leading player in the chemistry of lanthanides due to its role in the global market and high reserves.⁴⁶

Table 1. 1. Typical lanthanide abundance in ores, ^a Adapted from Cotton.⁴⁶

%	La	Ce	Pr	Nd	Pm	Sm	Eu	Gd	Tb	Dy	Ho	Er	Tm	Yb	Lu	Y
Monazite	20	43	4.5	16	0	3	0.1	1.5	0.05	0.6	0.05	0.2	0.02	0.1	0.02	2.5
Bastnasite	33.2	49.1	4.3	12	0	0.8	0.12	0.17	160	310	50	35	8	6	1	0.1
Xenotime	0.5	5	0.7	2.2	0	1.9	0.2	4	1	8.6	2	5.4	0.9	6.2	0.4	60.0

^a Bold values are in ppm.

Lanthanides numerous features that differentiate them from *d*-block metals. Particularly, the reactivity of these elements is higher than observed for transition metals, likewise the Group II. Some lanthanide features are summarized below:⁴⁶

- I. A very wide range of coordination numbers (generally 6–12, although 2, 3 or 4 are also known).
- II. Coordination geometries are determined by ligand steric factors rather than crystal field effects.
- III. They form labile 'ionic' complexes that undergo facile ligand exchange.
- IV. The 4*f* orbitals in the Ln³⁺ ion do not participate directly in bonding because they are well shielded by 5*s*² and 5*p*⁶ orbitals. Their spectroscopic and magnetic properties are uninfluenced by the ligand.
- V. They present small crystal-field splitting and very sharp electronic spectra in comparison with the *d*-block metals.
- VI. They prefer anionic ligands with donor atoms of rather high electronegativity (e.g. O and F).
- VII. They readily form hydrated complexes, which may cause uncertainty in the assignment of coordination numbers.
- VIII. Insoluble hydroxides precipitate at neutral conditions unless coordinating agents are present.

IX. The oxidation number is +3, although the +2 state is known for Eu and +4 is the most common for Ce.

X. They do not form $\text{Ln}=\text{O}$ or $\text{Ln}\equiv\text{N}$ multiple bonds as known for many transition metals and certain actinides.

XI. Unlike the transition metals, they do not form stable carbonyls and have (virtually) no chemistry in the zero-oxidation state.

Some of these properties make them unique, particularly their strong hard acid character. This property gives them more affinity to hard bases, like fluorine and oxygen donor ligands such as H_2O and OH^- , which are good nucleophiles for hard electrophiles as phosphorus. In addition, lanthanide cations suffer poor influence of ligands and complex stability is mainly due to electrostatic interactions, high coordination numbers and capacity of ligand exchange with the medium. These features are important for catalytic applications as those presented earlier and detailed in the next section.

However, it is important to observe limitations for the lanthanide chemistry in aqueous solution, which even under physiological conditions can form insoluble hydroxide complexes. Thus, many studies have been carried out about the complexation and stabilization of the Ln^{3+} by different ligands in aqueous solutions.^{49,50}

1.2.2.1 Use of lanthanide complex in the hydrolysis of phosphate esters

As shown before in Scheme 1.8, different metals have the capacity to hydrolyze the phosphodiester bond in the mimetic model of RNA.³³ However, La^{3+} is the only metal that can interact simultaneously with both oxygen atoms of the $\text{O}=\text{P}-\text{O}^-$ moiety and with the oxygen of the leaving group due to the greater La-O bond length and the lack of directionality in La^{3+} binding (Scheme 1.8c). The authors claimed that an important aspect is the flexibility of the coordination sphere of the lanthanides that allows it to bind strongly well to the phosphate moiety at the ground and at the transition states.³³

The total charge of the cation and the ability to polarize the P-O bond are important factors in reactions promoted by metals. Lanthanide ions present the advantage of a high charge/radius relationship and coordination numbers.⁵¹ The phosphodiester cleavage of RNA models (Scheme 1.8, p. 9)³³ are accelerated by Zn^{2+} and La^{3+} . However, La^{3+} is 10^4 -fold more efficient than Zn^{2+} . Figure 1.4 shows the structure for the complexes formed between Zn^{2+} and La^{3+} with the substrate. Modeling studies for substrate-metal complex revealed that the interaction is more favored between the negative charges of the phosphoryl oxygen atoms and the La^{3+} bound to

the 8-hydroxyquinoline moiety.²⁶ The association constant was determined kinetically and is 10^2 -fold lower for the lanthanide complex, showing that the rate enhancement of the La^{3+} complex is due to its Lewis acid properties. This study also supports that the catalytic capacity of the lanthanide cation depends on its interaction with phosphate and leaving group oxygens in the transition state, which facilitates the bond breaking with the leaving group.²⁶

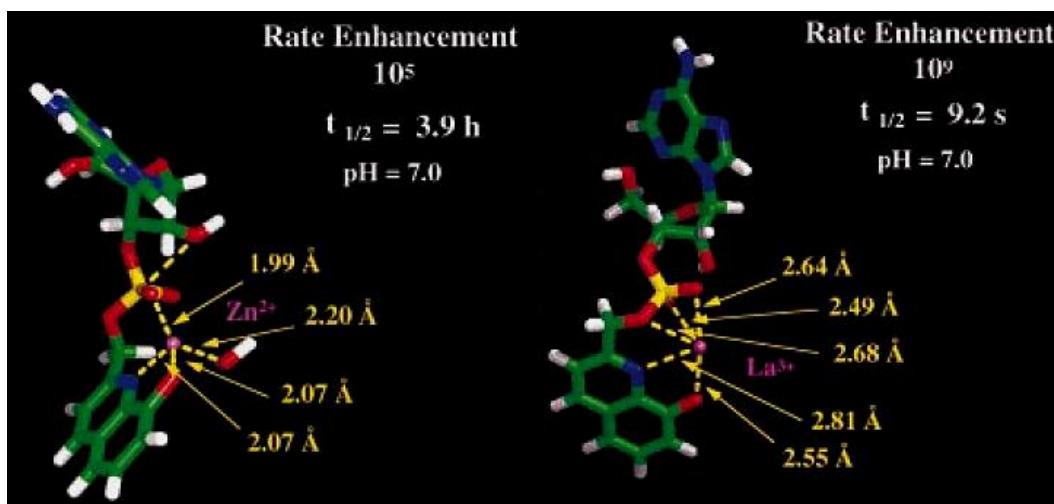


Figure 1. 4. Modeling of the tetrahedral Zn^{2+} complex showing the metal interaction with the oxygen of the (PO_2) moiety during the in-line attack by the ribose 2'-oxygen on the phosphorus atom. Modeling of the La^{3+} complex that due to the length of the bonds and the lack of geometrical constraints is capable of complexing with both (PO_2) oxygens as well as to both ground state and the incipient phenoxide in the transition state. Adapted from Blaskó and Bruice.²⁶

Lanthanide ions are remarkably effective catalysts for the hydrolytic cleavage of phosphate ester bonds, including the strong bonds in DNA.²⁵ But, their use require the formation of thermodynamically and even kinetically stable complex. Although free ions are catalytically effective, proper ligands must be used to coordinate lanthanides in the hydrolysis of phosphate esters. These ligands are important to stabilize the metal in solution to avoid loss of catalytic efficiency caused by its precipitation. The coordination properties of lanthanide cations are discussed in several reviews.^{52,53,54}

In water, the free aquo lanthanides(III) are relatively weak catalysts.¹² Numerous data show that cleavage of phosphodiester bonds occurs through the concerted action of a metal cation and a nucleophile, OH^- or RO^- . Therefore, low activities of lanthanide aquo cations most likely result from low concentration of OH^- or active metal hydroxo complexes in neutral solutions. Indeed, higher activities were reported for systems involving hydroxide or alkoxide lanthanide(III) complexes.^{55,56,57} Significant progress in the development of catalytic systems for the hydrolysis of phosphodiester bonds has been achieved. These studies show that not only the charge ratio of the metal is important for the activity, but also the basicity of the metal-

bound hydroxide ion. In the same direction, comparing the reactivities of individual mononuclear hydroxo complexes shows rather small variation for different lanthanides.¹²

Numerous sophisticated macrocyclic ligands, including calixarenes,⁵⁸ and the family of simple amino alcohol derivatives of tris(hydroxymethyl)aminomethane (Tris) (Figure 1.5), have been employed as lanthanide ligands in aqueous solutions. Tris was successfully used for stabilization of Zr(IV),⁵⁹ and bis-Tris formed hydrolytically active complexes with La(III).⁶⁰ High hydrolytic activity has been reported for complexes between lanthanide(III) and bis-tris propane (BTP) in weakly basic solutions.^{61,62} These reports show that lanthanide cations can be used under slightly basic conditions without apparent precipitation. However, the BTP system differs from other lanthanide-based systems in several aspects. First, the reaction kinetics for phosphate diester cleavage follows a first-order profile regard to the metal without any "saturation" as observed with other lanthanide-based systems. Second, pH-rate profile for these reactions are very steep, indicating deprotonation of at least two coordinated water molecules to afford catalytically active complexes.¹² For such reasons, BTP has been widely used for several kinetic studies.^{49,63}

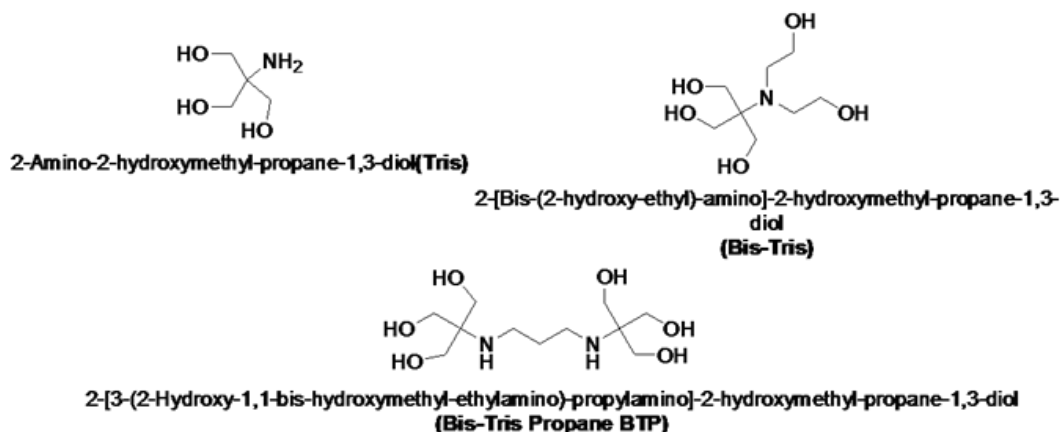
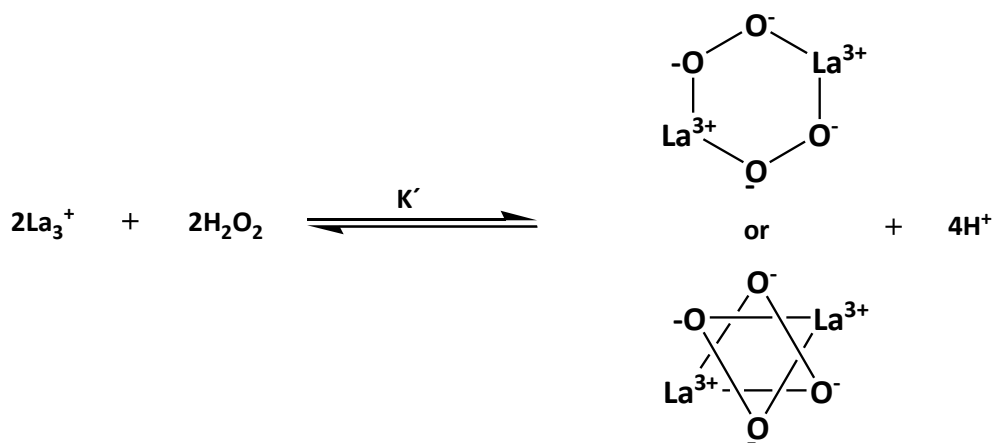


Figure 1. 5. Structures of tris-(hydroxymethyl)aminomethane (Tris) derivatives commonly used in the formation of stable complexes with lanthanide ions.

1.2.2.2 Effect of the Ln³⁺ complexes in the presence of nucleophilic species for cleavage of phosphate esters

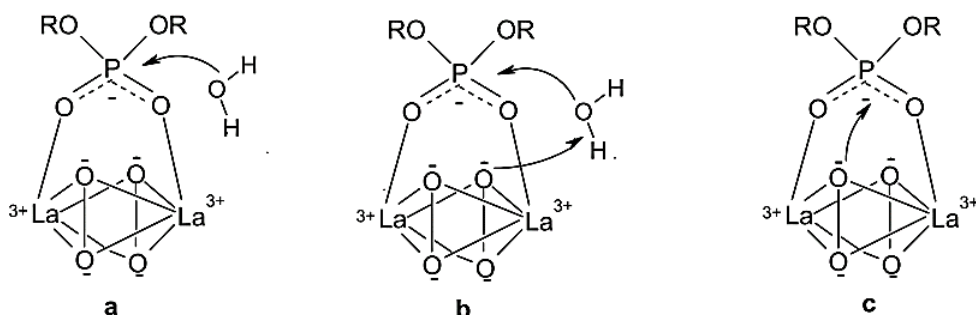
It is known since the early 1950's that lanthanide ions associated with hydroxide ions can catalyze nucleophilic substitutions in phosphate esters.⁶⁴ These metals not only act like "free" cations, they can create catalytically active oligomeric complexes.⁵⁵ Synergic effect has been also reported in the hydrolysis of phosphate esters when the La³⁺ is associated with nucleophilic species like hydrogen peroxide.^{65,66} It was found that, in the presence of hydrogen peroxide, the

catalytic activity is 10^4 -fold higher than with La^{3+} alone.⁶⁶ The reason implicated for this boost was cooperative interactions between the cation and H_2O_2 by forming active catalytic species as those shown in Scheme 1.9.



Scheme 1. 9. Formation of active catalytic complex between La^{3+} and H_2O_2 .

These binuclear complexes (Schemes 1.9 and 1.10) form bridged bonds with the phosphate ester (Scheme 1.10a). The bound peroxide anion can act as an intramolecular base (Scheme 1.10b) or as an intramolecular nucleophile affording peroxiphosphate (Scheme 1.10c). These observations have led to numerous studies who attempted to find the best synergistic system for the hydrolysis of phosphate esters.^{55,57,65}



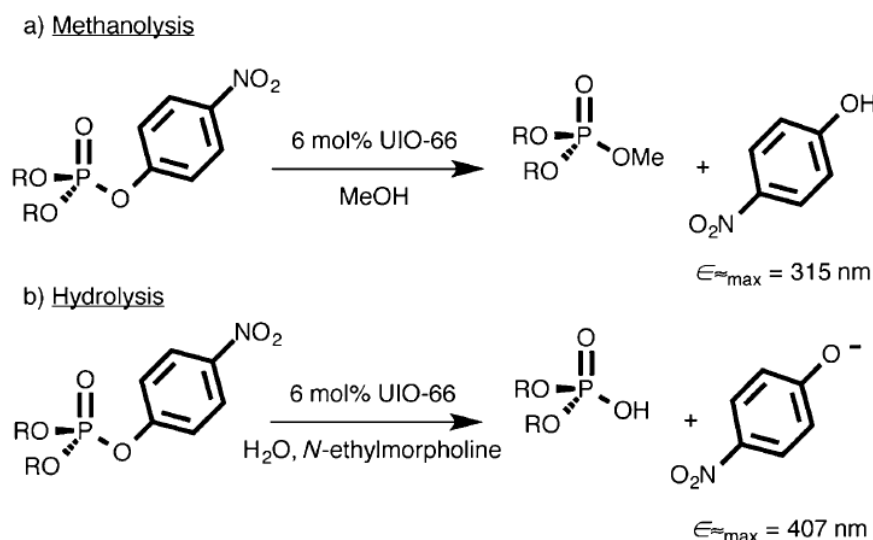
Scheme 1. 10. Mechanistic possibilities for the role of lanthanide peroxide complexes in the hydrolysis of phosphate esters.

No doubt that homogeneous catalysis is efficient and convenient, but recovery of the catalyst and incorporation into a recycling or continuous flow process is a difficult task. These difficulties can be overcome by immobilizing the catalytic centers on the surface of different matrices. Although, used for many types of applications, heterogeneous catalysis has not been widely applied to hydrolytic processes. Nevertheless, recent investigations demonstrated the efficacy in such cases.⁹

1.2.3 Heterogeneous catalysis in the hydrolysis of phosphate esters

The previous section provided a view of the strong capacity of lanthanide cations to catalyze the hydrolysis of phosphoesters in a homogeneous medium. Reports on efficient phosphate ester hydrolysis by metal centers built in silica based matrices and organic polymers show the potential applications of heterogeneous catalysts.^{67,68,69,70} The focus has been the *d*-metal block, mainly Cu²⁺, Zn²⁺, and Fe³⁺, which have been supported in solid matrices. A Cu²⁺polymer system presented good activities for phosphate ester hydrolysis, Hanafy *et al.*⁷⁰ reported an increase in the reaction rate of about 75,000-fold relative to the uncatalyzed hydrolysis of the *bis*(*p*-nitrophenyl)phosphate (BNPP) at pH 8.0 and 25 °C. Their complex was able to continuously catalyze the BNPP hydrolysis with considerable activities after eight reuses.

Other metals, Zr(IV), Ce(III), and Ce(IV), have also been coordinated to polymers, exhibiting good activity for phosphodiester bond cleavage.^{69,71,72} For instance, Zr(IV) complexes exhibited activity for the methanolysis and hydrolysis of Paraoxon (Scheme 1.11). This compound is a potent acetylcholinesterase inhibitor, about 70% as potent as the nerve agent Sarin. The catalyst was successfully recovered by filtration, and no activity was observed in the supernatant, demonstrating that the catalysis is heterogeneous and the active metal is not leached.⁷¹

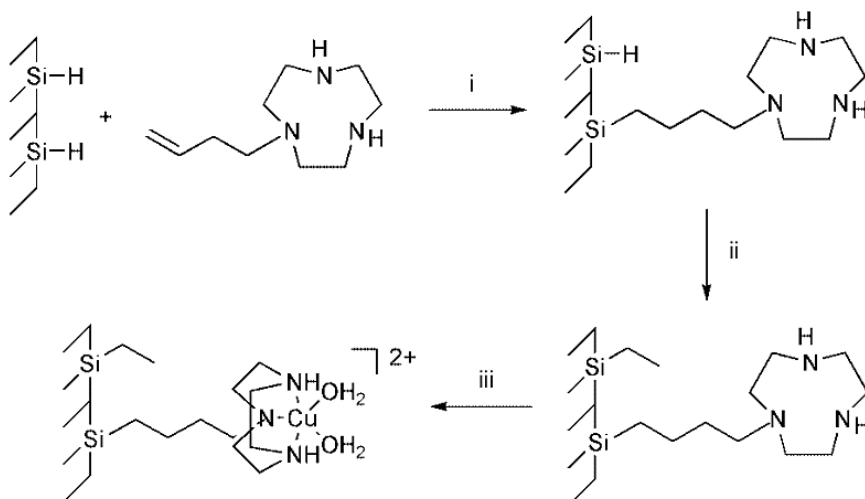


Scheme 1. 11. Methanolysis(a) and hydrolysis (b) of both methyl paraoxon (R=CH₃) and PNPDP (R=phenyl) in the presence of UIO-66 (Metal organic framework made up with Zr(IV)). Adapted from Katzet *al.*⁷¹

Zhang *et al.*⁸ reported the use of chitosan, a linear polysaccharide composed of randomly distributed β -(1,4)-linked D-glucosamine (deacetylated unit) and *N*-acetyl-D-glucosamine (acetylated unit) as support for a series of metals. The chitosan-metal complexes were used for the degradation of four organophosphorous pesticides. They observe that the catalytic activity depends on the ability of the target molecule to diffuse through the support and also on the

strength of the Lewis acid character of the metal. The best results were found when low molecular weight chitosan and Fe^{3+} were employed.

As one of many approaches to develop new useful catalysts, the immobilization of metal complexes onto the surface of insoluble solid matrices is an important tool to promote efficiency and selectivity. In this regard silica-based materials have presented interesting properties for the hydrolysis of phosphoester bonds.^{9,67} The surface hydroxyl groups can be functionalized with organic ligands to coordinate the metal or a metal complex, creating the catalytic center. Bodsgard *et al.*⁶⁷ found that a bound organocopper (II) complex presented good activity for the hydrolysis of *bis*(4-nitrophenyl)phosphate (BNPP) (Scheme 1.12). An interesting observation of this work was the presence of an induction period in which no substantial hydrolysis was observed. This induction period was only poorly explored, being related to solvation of the solid surface.



Scheme 1. 12. Stages to generate the active Cu(II) complex supported on regular silica: i, $[\text{RhCl}(\text{PPh}_3)_3]$, toluene, reflux, 3 days; ii, C_2H_4 , $[\text{RhCl}(\text{PPh}_3)_3]$, toluene, 25 °C, 15 h; iii, $\text{Cu}(\text{NO}_3)_2$ (aq). Adapted from Bodsgard *et al.*⁶⁷

In this work, we propose the use of MCM-41, which possess high surface area that may facilitate the encounter of the substrate and the catalyst. Below we focus on the characteristics and uses of this material.

1.2.4 Mesoporous molecular sieves MCM-41

Since its discovery in 1992,¹⁰ MCM-41 has become a popular member of the M41S family of mesoporous silicate and aluminosilicate materials. The most interesting characteristic of MCM-41 is its regular pore system with hexagonal array of one-dimensional shaped pores (Figure 1.6). The pore diameter varies from 2 to 10 nm, overall showing high surface up to 1500 $\text{m}^2 \text{g}^{-1}$ and specific pore volume up to 1.3 mL g^{-1} .

1.2.4.1 Synthesis of MCM-41

In general, mesosilica assembly involves the addition of a silicate source to an aqueous surfactant solution. Hydrolysis and condensation lead to a silica framework, which builds around the surfactant micelles. Two mechanisms were originally presented to describe mesosilica formation.¹⁰ The first mechanistic model described the addition of silicate agents to cetyltrimethylammonium bromide (CTAB) micelles, which polymerize around the previously formed micelles (Figure 1.6a). The second model proposed that addition of silicate to an aqueous CTAB solution induced ordering of silicate-encased surfactant micelles simultaneously, that is, micelle formation required the presence of silicate (Figure 1.6b). After polymerization, the mesosilica becomes porous by removing the surfactant template by solvent extraction, calcination or microwave digestion. Although, CTAB (a C-16 surfactant) is the most used surfactant, Beck¹⁰ and others have used surfactants with shorter hydrophobic tails (C-14, C-12, C-8) leading to the production of MCM-41 with shorter mesopores (Figure 1.7) which correlate directly with the size of the micelles; smaller micelles are made of surfactant cations(CTA⁺) with shorter hydrophobic tails.

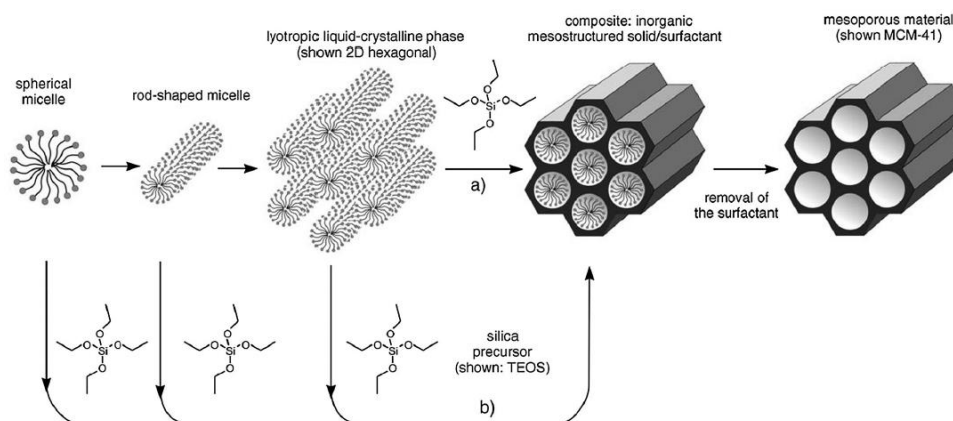


Figure 1. 6. Representation of the mechanism proposed by Beck et al.¹⁰ Image adapted from Gibson.⁷³

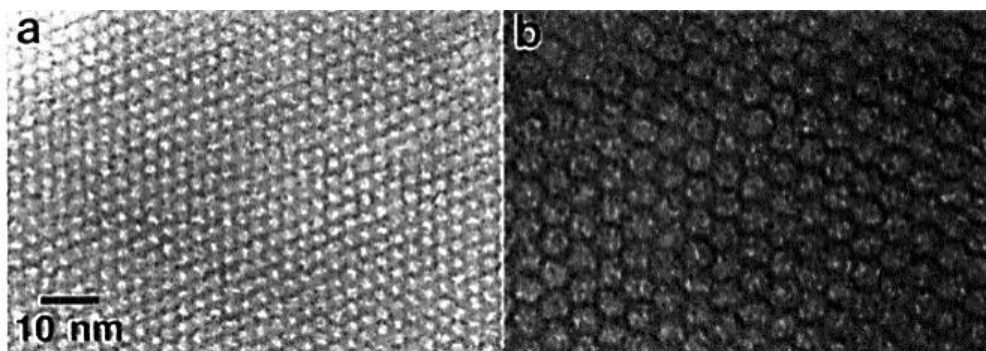


Figure 1. 7. TEM images of MCM-41 showing pore size of the materials made with (a) C-8 surfactant or (b) C-16 surfactant. Adapted from Beck et al.¹⁰

Later Monnier *et al.*⁷⁴ advocated that the original mechanistic models were insufficient to establish an understanding of MCM-41 formation. It was observed that mesosilica forms under conditions that would not normally support silica condensation (high pH, low silica and CTA⁺ concentration) and that precipitation is observed immediately on addition of the silicate to the surfactant (C-8 to C-20) solution. Basically, three factors were crucial to mesosilica formation: (i) multidentate binding of silicate oligomers; (ii) preferred polymerization of silicates at the surfactant-silicate interface; and, (iii) charge density matching across the interface.

Due to its regular structure and pore shape MCM-41 has attracted considerable interest as a material for a broad range of applications in catalysis, sorption, molecular recognition, electronics, and photochemistry. Some examples are seen in Figure 1.8.

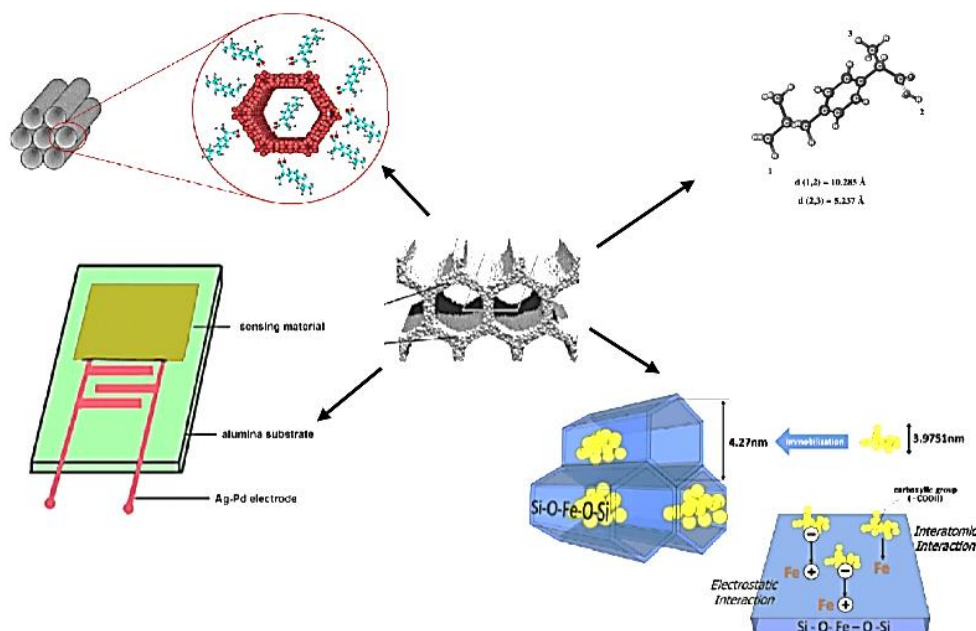


Figure 1. 8. Possible applications of MCM-41: drug delivery system,^{75,76} humidity sensors,⁷⁷ and enzyme immobilization.⁷⁸

1.2.4.2 Characterization of MCM-41

Many different techniques are usually applied to determine the composition, morphology and properties of heterogeneous materials.

X-ray crystallography is used for determining the atomic and molecular structure of a crystal (or a crystalline material), in which the crystal atoms planes cause a beam of incident X-rays to diffract into many specific directions. Each crystalline material has characteristic X-ray diffraction patterns and parameters, which affords the electron density of atoms in the unit cell and also provides information about the existence of co-crystals, purity and crystallinity. However, the concept of crystallinity cannot be used for MCM-41 type materials, which have walls made of

amorphous silica. This is observed by the absence of diffraction at high angles. However, the ordered hexagonal network, where one pore is surrounded by six others (Figure 1.9a), generates the characteristic reflections of the MCM-41 at small angles (Figure 1.9b).

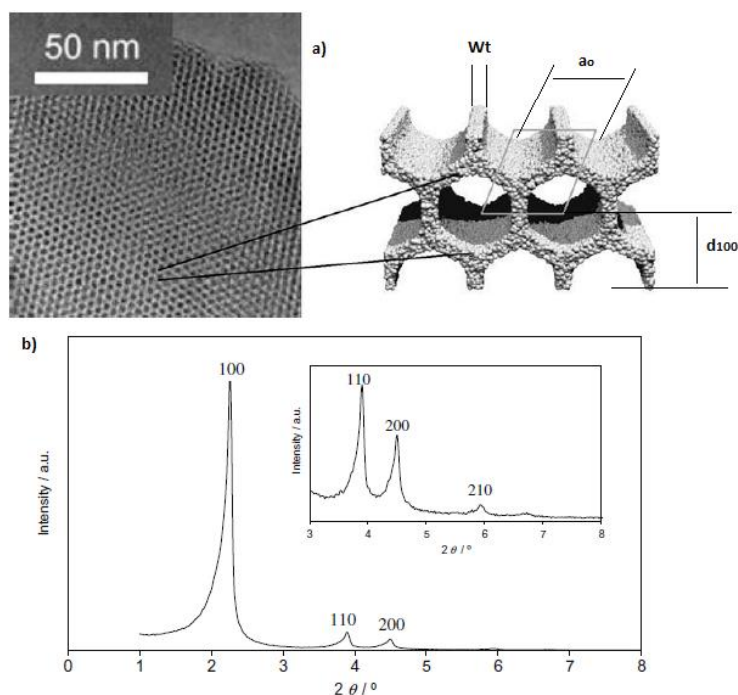


Figure 1. 9. a) TEM image of the honeycomb structure of MCM-41 and a schematic representation of the hexagonal shaped one-dimensional pores. b) Typical XRD pattern of MCM-41 with Miller indices of the diffraction planes. Inset: enlargement of the XRD pattern. The corresponding d-spacings: (100) = 3.90 nm, (110) = 2.26 nm, (200) = 1.95 nm, and (210) = 1.48 nm. Adapted from Meynen *et al.*⁷⁹

The X-ray diffraction provides quick information about the degree of organization of the material and physical characteristics. Application of the Bragg's law ($n\lambda=2d\sin\theta$) provides the distance between planes d_{100} (Figure 1.9a), which can be used to calculate the parameter network (a_0) = $2d_{100}/\sqrt{3}$ and the wall thickness (Wt); the late one by subtracting the pore diameter (D_p , calculated by the BJH method, mentioned later) from the network parameter (a_0).

The textural characterization of porous solids (volume, size and geometry) can be carried out by adsorbing molecules probes, like N_2 , Ar, CO_2 or He. Liquid N_2 is the most used for mesoporous materials. The N_2 adsorption isotherms measure the specific area related to micro, meso and macroporosity. Porous materials are often characterized in terms of pore sizes derived from gas sorption data. IUPAC conventions have been proposed for classifying pore sizes and gas sorption isotherms that reflect the relationship between porosity and sorption (Figure 1.10). There are six types of isotherm, which are typical of adsorbents showing microporous (type I), nonporous or macroporous (types II, III, and VI), or mesoporous (types IV and V) structures.^{80,81,82}

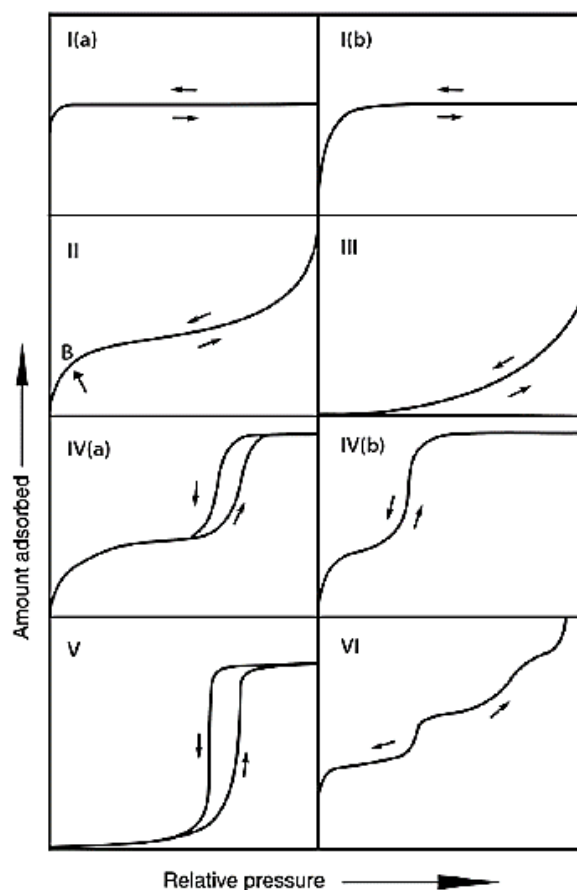


Figure 1. 10. The IUPAC classification of adsorption isotherms showing both the adsorption and desorption pathways.⁸²

Figure 1.11 shows a typical adsorption isotherm for MCM-41. The isotherm is type IV, characteristic of a mesoporous material with multilayer absorption cycles. The surface area for this material was $1180 \text{ m}^2 \text{ g}^{-1}$.⁸³

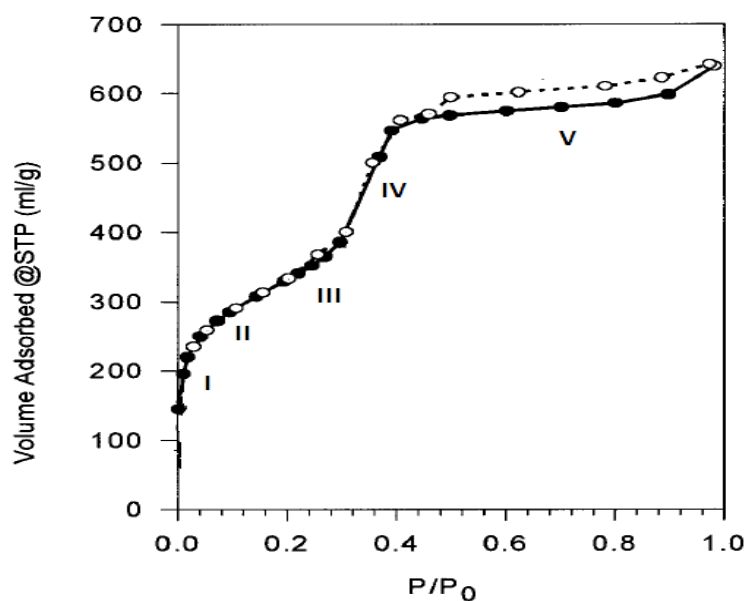


Figure 1. 11. Nitrogen sorption isotherm for MCM-41. Adapted from Zhao and Lu.⁸³

The isotherm in Figure 1.11 can be split into five regions. Region I, nitrogen molecules are adsorbed on the surface of MCM-41. Region II, formation of the monolayer, in this point the specific area can be calculated by the equation $BET = n_m A$, where n_m and A are the number of molecules absorbed in the monolayer and the cross-sectional area of the nitrogen gas molecule. Region III, where over the monolayer multiple layers are adsorbed. Region IV, where occurs a sudden increase of the quantity of nitrogen absorbed, called the capillary condensation zone, indicates when the pores are filled. Region V, the pore is saturated, and a small amount is adsorbed onto the walls. Using the volume adsorbed at the relative pressure $p/p_0 \approx 0.95-0.99$ the total pore volume $V_{total} = 1.54 \times 10^{-3} V_{ads}$ can be calculated.

The hysteresis, phenomena resulting from the difference between the mechanisms of condensation and evaporation, is also an important feature that gives information about the geometry of the pore. MCM-41 has a type H3 hysteresis loop at relative pressures of 0.42, which indicates capillary condensation of nitrogen within interparticles and/or some impurity phases, such as lamellar mesostructures often generated by liquid-templating synthesis. The mesopore size distribution or pore diameter can be calculated using the BJH method,⁸⁴ by assuming that all pores have cylindrical shape. This method is based on the Kelvin equation, which predicts the formation of liquid nitrogen in the capillary condensation stage.

Microscopy is another group of techniques largely used for material characterization. An electron microscope is an equipment that uses a beam of accelerated electrons as a source of illumination. Two techniques are routinely applied in the material chemistry, scanning electron microscopy (SEM) and transmission electron microscopy (TEM) (Figure 1.12). The scanning electron microscope (SEM) uses a focused beam of high-energy electrons to generate a variety of signals at the surface of solid specimens. The signals that derive from electron-sample interactions reveal information about the analyzed material including external morphology (texture), chemical composition, and crystalline structure and orientation. Figure 1.12a depicts SEM images used to determine size and morphology of a modified MCM-41.⁸⁵ The particle size of the sample ranges from 400 to 1100 nm with an average size of 580 nm. It is clearly visible that most particles are almost perfectly spherical with some agglomeration.

The transmission electron microscopy (TEM) uses a beam of electrons transmitted through an ultra-thin specimen, that interacts with it. TEM is a very powerful tool for material science, the interactions between the electrons and the atoms can be used to observe the crystal structure, besides dislocations and grain boundaries. TEM images can also be used to study the growth of layers, their composition and defects, pore size and wall thickness of the porous materials. Figures 1.12 **b** to **d** show TEM images where is seen a hexagonal symmetry of the pores in the MCM-41, like a beehive.

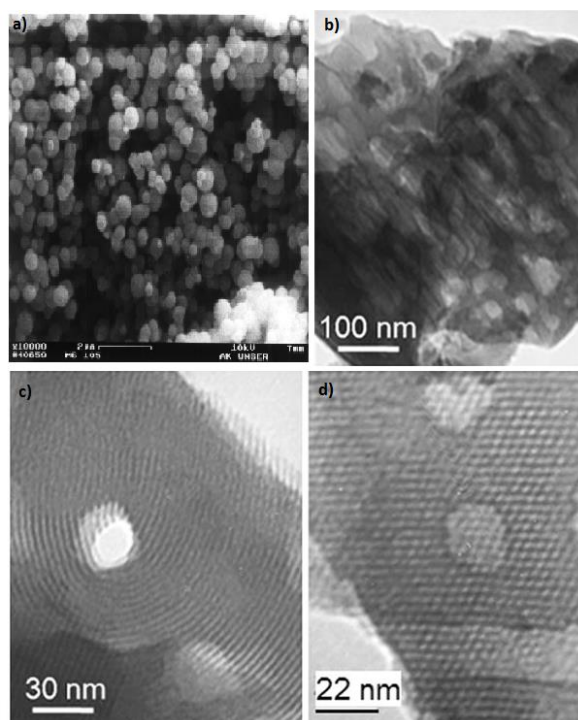


Figure 1. 12. a) Scanning electron micrograph of MCM-41 spheres prepared with n-hexadecylpyridinium chloride. Adapted from Grün *et al.*⁸⁵ b), c), d) Transmission electron microscopy images of the MCM-41 mesoporous silica. Adapted from Pasqua *et al.*⁸⁶

Thermal analysis fulfills the group of basic techniques used for material characterization. Thermo-gravimetric analysis (TGA) is a technique in which the mass change of the sample is measured as a function of temperature. Uncalcinated MCM-41 have three characteristic regions: 25-135 °C, where the water molecules are desorbed; 135-345 °C, when the surfactant decomposes; and at higher temperatures for the mass loss due to dehydration of adjacent silanol groups.⁸⁷ These events are commonly followed with two other analyses, Differential Thermal Analysis (DTA) and Differential Scanning Calorimetry (DSC), which provide similar information. DSC and DTA analyses measure the amount of energy absorbed or released by a sample when it is heated or cooled, providing quantitative and qualitative data on endothermic (heat absorption) and exothermic (heat evolution) processes. This allows the characterization of phase transitions and the study of order-disorder transitions and chemical reactions that can occur on the silica material when heated in the presence of different atmospheres (generally N₂ or synthetic air).

Depending on the MCM-41 application, many other characterization techniques can be used to describe its physical-chemical nature. The SiOH groups on the MCM-41 surface have been qualitatively and quantitatively determined by solid state ²⁹Si nuclear magnetic resonance with magic-angle spinning and cross polarization (²⁹Si CP/MAS NMR), thermogravimetric analysis, Fourier transformed infrared (FTIR) spectroscopy, and temperature-programmed desorption (TPD) of pyridine, among others.⁸³ For instance, the ²⁹Si solid state NMR is especially

useful to characterize silanol populations formed after a postgrafting functionalization. For example Zhao and Lu⁸³ reported that only a particular type of silanol groups are susceptible to modification with trimethylsilyl (TMS) groups (Figure 1.13).

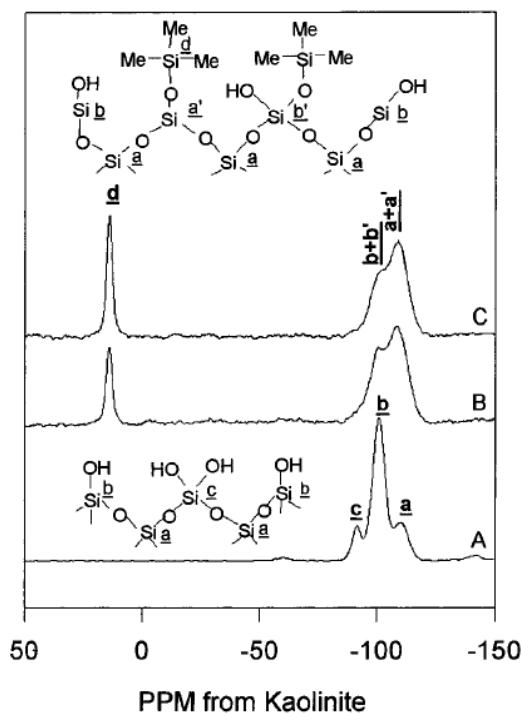


Figure 1. 13. ²⁹Si CP/MAS NMR spectra for template-extracted Si- MCM-41 (A), partially silylated Si-MCM-41 with a 43% coverage (B), and fully silylated MCM-41 (C). Adapted from Zhao and Lu⁸³

The ²⁹Si CP/MAS NMR spectra for MCM-41 samples show characteristic profiles.⁸³ Three resonances signals at -110, -101, and -92 ppm assign the silicon sites Q⁴, *Si(OSi)₄ (a), Q³, HO*Si(OSi)₃ (b), and Q², (HO)₂*Si(OSi)₂ (c), respectively. The Q³ sites are associated with isolated SiOH groups (i.e., free and hydrogen-bonded), while the Q² sites correspond to geminal silanols. The modified samples (Figure 1.13 B and C) show a sharp peak at 14 ppm, ascribed to the attached silicon sites in trimethylsilyl group (TMS) groups (d). The intensity of the Q⁴ silicons (a + a') is greater than prior functionalization, which reorganized the silicon sites at the expense of Q³ silicons. The Q² sites for both modified MCM-41 samples are not observed in the ²⁹Si CP/MAS NMR spectra, demonstrating that geminal silanols form active sites for silylation.

1.2.4.3 Functionalization of MCM-41

Optimization of silica functionalization is a field of intense research because its numerous applications and functionalization possibilities, which apart from their high porosity, can be tuned in a nearly unlimited fashion. Among applications, the SiOH groups in MCM-41 have been modified for use in catalysis,⁸⁸ adsorption,⁸³ and novel composites.⁸⁹ Mobil Oil Corporation has patented a sorption separation process using modified MCM-41 for purification of water. Feng

et al.⁹⁰ reported a thioalkylated functionalized mesoporous adsorbent for removal of mercury from wastewater (Figure 1.14).

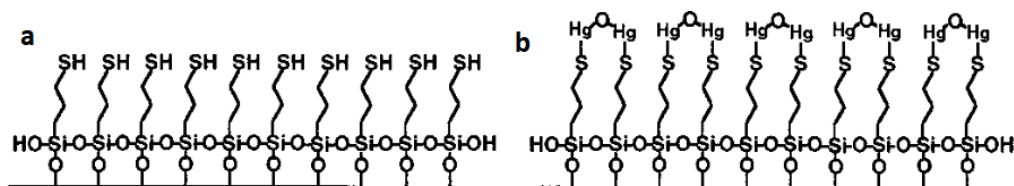


Figure 1. 14. Thioalkylated MCM-41 for mercury removal from wastewater. A) Close-packed material at 75% surface coverage and B) containing mercury. Adapted from Feng et al.⁹⁰

Modifications have made MCM-41 more biocompatible with biological media. Williams *et al.*⁸⁹ reported the synthesis of a modified MCM-41 for delivery of high amounts of drugs. The general biocompatibility of the modified MCM-41 has been proved in various studies. In the field of catalysis, functionalization has been routinely used. Studies have shown that modified MCM-41 can be used for enantioselective synthesis⁹¹ and C-C coupling of quite unreactive molecules.⁹² These are just two examples of many applications of functionalized MCM-41 in fine chemistry.

1.2.4.4 Stability of MCM-41

Thermal and hydrothermal stabilities of silicates have been extensively debated. Pure-silica and aluminosilicate MCM-41 have been shown to be stable at as high as 1100 K in the presence of water steam.⁹³ However, mesoporous MCM-41 disintegrate readily in distilled water around 370 K whereas stable in 100% steam at 800 K.⁹⁴ In general, MCM-41 family materials or any other porous silica material undergo structural changes in aqueous systems. This characteristic makes them attractive to some uses like the medical field, since the human body may discharge silicon particles from the body without major issues.⁹⁵ The rapid dissolution of mesoporous silica nanoparticles (MSNs) in biological media⁹⁶ is vital for their biomedical applications since most FDA-approved drugs require “the complete clearance of all injected contrast agents in a relatively short period of time.”⁹⁷

The stability of porous silicates can be improved with the incorporation of organic groups on the surface, combining the properties of organic and inorganic building blocks in the material.⁹⁸ The nature of the organic group can control many properties, such as adsorption, ion exchange, hydrophobicity, thermal stability, host-guest interactions, among others.⁸⁶ For example, Ray *et al.* post grafted carboxyl functionalized organosilanes (Figure 1.15) to get uniform spherical silica nanoparticles.⁹⁹ This material was used for the synthesis of pyrrolo[2,3,4-*k*]acridones, presenting good catalytic activities even after exposure to ambient atmosphere for 20 days. The aged catalyst was used for at least six times with good efficiency.

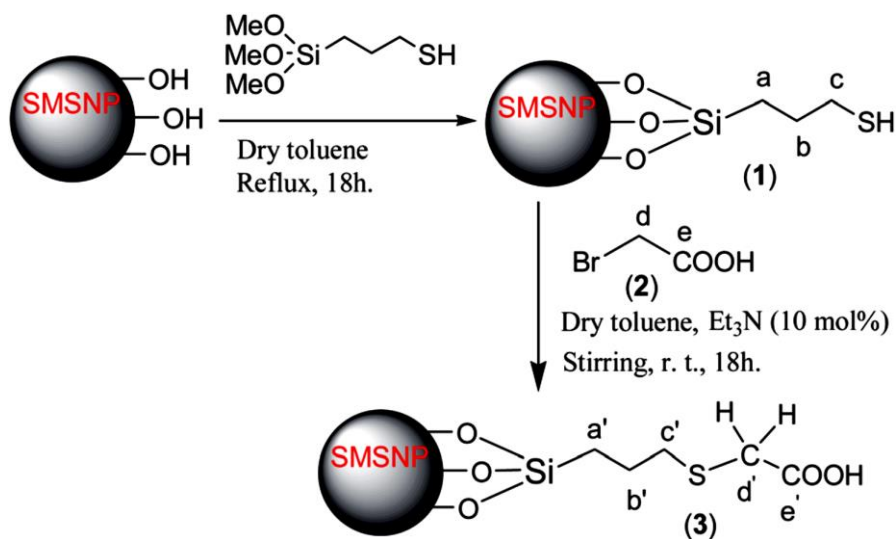


Figure 1. 15. Preparation of surface carboxyl functionalized MSNs. Adapted from Ray *et al.*⁹⁹

The incorporation of inorganic atoms or molecules into the mesoporous silica structure can also tune the dissolution rate.⁹⁶ For instance, zirconium doping was found to virtually stop the dissolution rate of silica,¹⁰⁰ while the use of calcium,¹⁰¹ manganese, or iron^{102,103} ion/oxide doping had the opposite effect. The degradation kinetics also depends on the pH and presence of proteins or glutathione (GSH).⁹⁵ One example of biodegradable iron-oxide@silica nanocomposites was reported by Omar *et al.*¹⁰⁴ The particle had a unique cavity-like mesostructure with large pores containing iron oxide crystalline nanophases that remained intact in water for 3 days. Nevertheless, exposition by the same period in fetal bovine serum (FBS) degraded the particles to sub-10 nm pieces as shown by TEM (Figure 1.16).

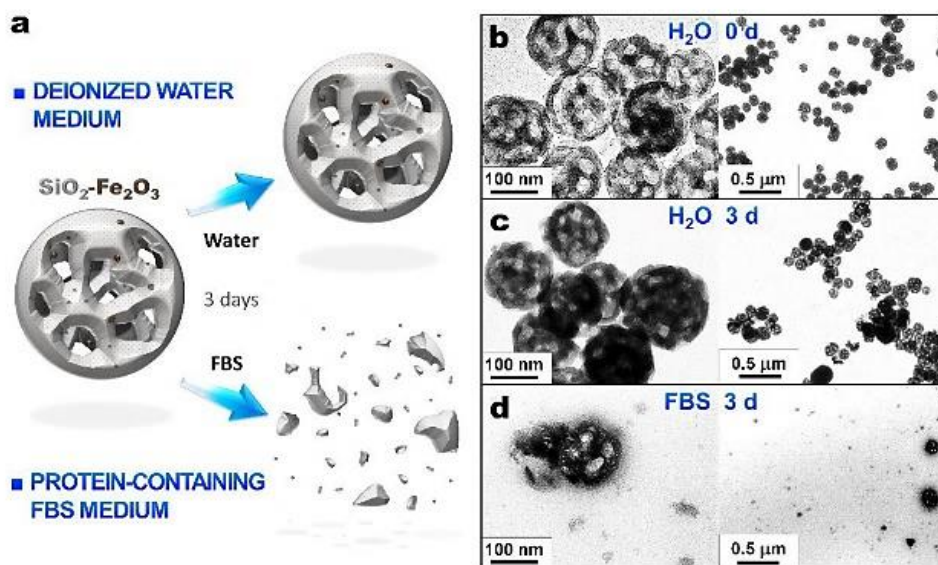


Figure 1. 16. Representation of the degradability of large-pore silica-iron oxide NPs in water and in FBS (a). TEM images of the nanovectors before (b) and after three days of dispersion in water (c) or in FBS. Adapted from Omar *et al.*¹⁰³

1.2.5 Physical Chemistry and Chemical Physics of Mesoporous Silica

According to the American Chemical Society, physical chemistry is devoted to the study of how matter behaves on a molecular and atomic level and how chemical reactions occur,¹⁰⁵ while chemical physics is concerned with the application of the concepts and theories of physics to the analysis of chemical systems and its physical behavior. Both aspects are relevant for heterogeneous systems, because interactions of the materials with the medium (or species in the reaction solution) can generate changes in their structure and to the parameters that control the diffusion and adsorption of liquids and substrates in the material. This is particularly important because the overall rate of a reaction may be limited by the rate of mass transfer of reactants between the bulk fluid and the catalytic surface,¹⁰⁶ which may even affect the catalytic activity.^{78,107,108} In such cases, the effectiveness of the catalyst does not depend on improvement of chemical activity but rather depends on providing a better diffusion for the substrate in the solid matrix.¹⁰⁸ This aspect is one of the main problems when scaling chemical reactions to industrial level.

It is important to observe though that diffusion or adsorption of species on mesoporous silica not only depends on its the physical characteristics (size, porosity, and texture) but also on the chemical interactions with the target molecule. Next pages address the factors that control the diffusion of molecules on the mesoporous silica structure.

1.2.5.1 Factors that affect the mobility of molecules in a mesoporous silica aqueous system

Diffusion is the spontaneous intermingling of atoms or molecules by random thermal motion. It gives rise to motion of species relative to motion of the mixture. In the absence of other gradients (such as temperature, electric potential, or gravitational potential), molecules of a given species in a single phase will always diffuse from regions of higher concentrations to regions of lower concentrations. This gradient results in a molar change of the species (e.g., A), W_A (moles/area x time), in the direction of the concentration gradient. The flux of A, W_A , is relative to a fixed coordinate and is a vector quantity with typical units of $\text{mol/m}^2 \times \text{s}$.¹⁰⁶

On industrial reactors this transport can be modulated (e. g. the use of pumps) to facilitate the transport. The use of lubricants can also be used to reduce friction between surfaces in mutual contact. It may also have the function of transmitting forces, transporting foreign particles, or heating or cooling the surfaces.

Several reports look to understand the behavior of water into different silicon channels.^{109,110,111,112} Asay and Kim¹¹² reported the formation of three layers of water on the surface of silicon oxide (Figure 1.17). The only one that facilitates the transport is the liquid water, which is extremely limited in nano, micro or mesoporous silica structures.^{109,110,111} In any case, deprotonation of surface silanols can change the diffusion and the structure of the confined fluid which is likely to modify substantially the transport properties of electrolytes solutions¹¹⁰

The importance of confinement provided by the porous channels has been addressed by Ohkubo *et al.*¹¹¹ They observe that “confined water within artificial silicate materials, such as ordered silicates and synthetic clay minerals, is attractive for chemical engineering applications. In such confined spaces, water properties including its structure, melting point, and mobility differ significantly from those of bulk water.” Because silica can react with water,^{96,113} the effects of water confinement gets more spurious because silicate released into solution may form a network,¹¹⁴ that affects the chemical and physical characteristics of the base material. These changes or/and the formation of a phase that expedite the diffusion can generate more active species on catalytic applications, this observation is commonly reported as induction time, after which catalytic activities increase.^{115,116}

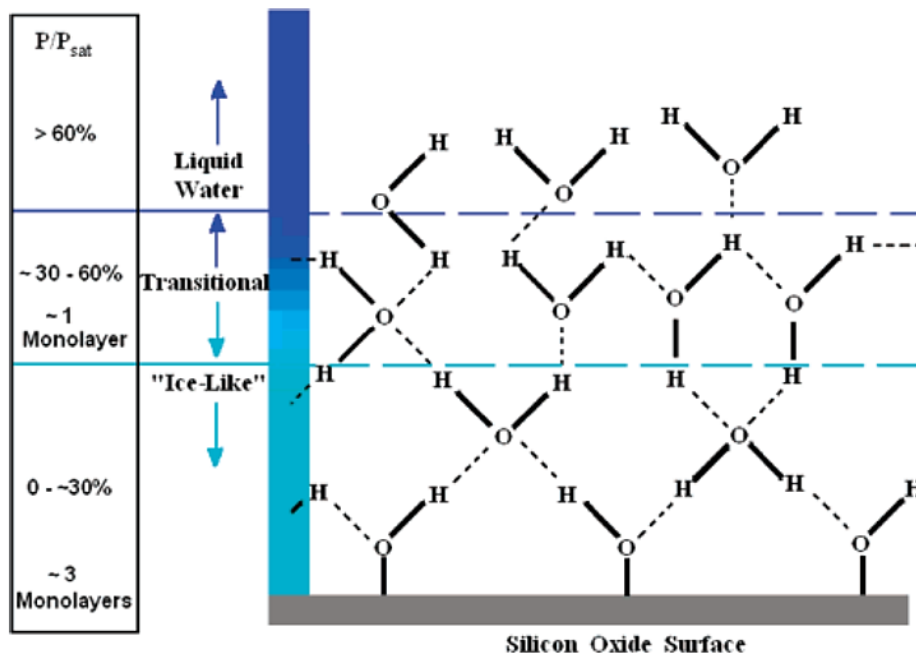


Figure 1. 17. Representation of the structural evolution of water molecules as the adsorbed layer thickness rises with relative humidity (RH). The icelike structure grows up to 3 molecular layers thick as RH increases from 0 to 30%. In the RH range from 30 to 60%, the icelike structure continues to grow while liquid structure begins to form. In this transitional RH region, approximately one molecular layer grows. Further increase in the RH above 60% causes water to adsorb in the liquid configuration (--- hydrogen bonds, —; covalent bonds). Adapted from Asay and Kim.¹¹²

1.2.5.2 Physical chemical aspects that modulated the structural changes on silica in aqueous medium

The stability of the framework depends on the chemical nature of the bonds that form the silica material. Figure 1.18 shows the general mechanism for the degradation of silica nanoparticles in aqueous medium. The general mechanism consists of three stages. The first one corresponds to the hydration of the material and the other two are related to hydrolysis processes (Figure 1.18). These two stages can be modulated by acid or basic conditions, just as the formation of the structure is also controlled by the pH.^{117,118}

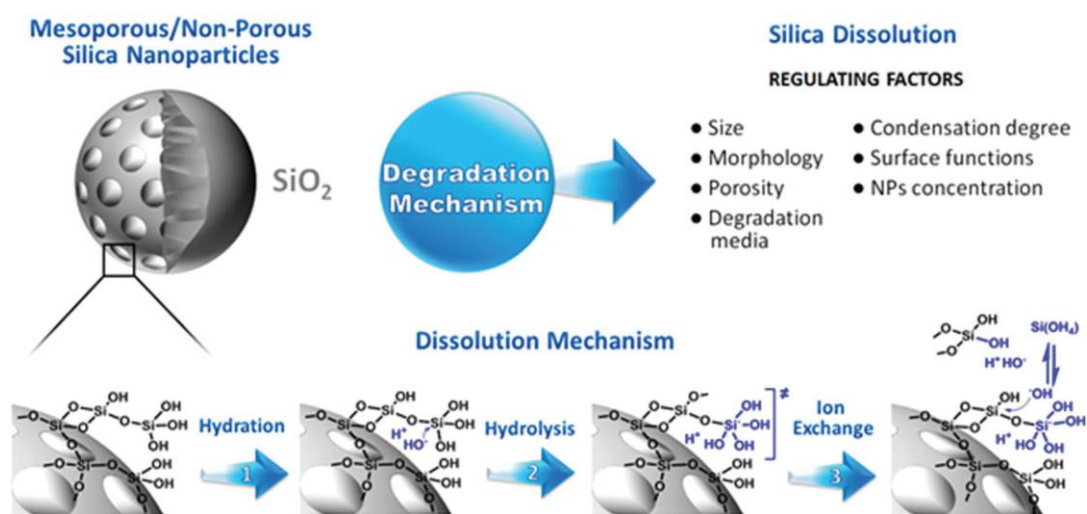


Figure 1. 18. Illustration of the base and degraded structures of silica NPs along with the mechanism and regulating factors of the degradation. Adapted from Croissant et al.⁹⁶

Figure 1.19 present the mechanism for growth and hydrolysis of the silica framework. The mechanism shows that on either case the protonation or deprotonation of silanol groups is necessary to start the reaction. In section 1.2.4.2, it was mentioned the types of silanol groups (Q⁴, Q³, Q²) present in the MCM-41 structure. The Q⁴ is more substituted and more difficult to protonated or deprotonated, Q³ and Q² sites presented Si-OH bonds that are labile to transfer a proton to start the reaction. That is why the presence of hydrophobic groups or groups that coordinate water molecules in a stable form may stabilize the overall structure.

These phase changes determinate the applicability of the silica material and have been extensively studied. Melvin Avrami in a set of three papers from 1939 to 1941 propose a mathematical model to explain the kinetic of phase change.^{119,120,121} This mathematical model has been used for kinetics of solid nucleation and dissolution.^{122,123,124}

In summary, the physical chemical characteristics of silica materials determinate its usability in aqueous systems. However, its structure can undergo changes that can be beneficial

or harmful for its application. The activity of the silica materials is also modulated by physical factors, which are in some cases determinant.

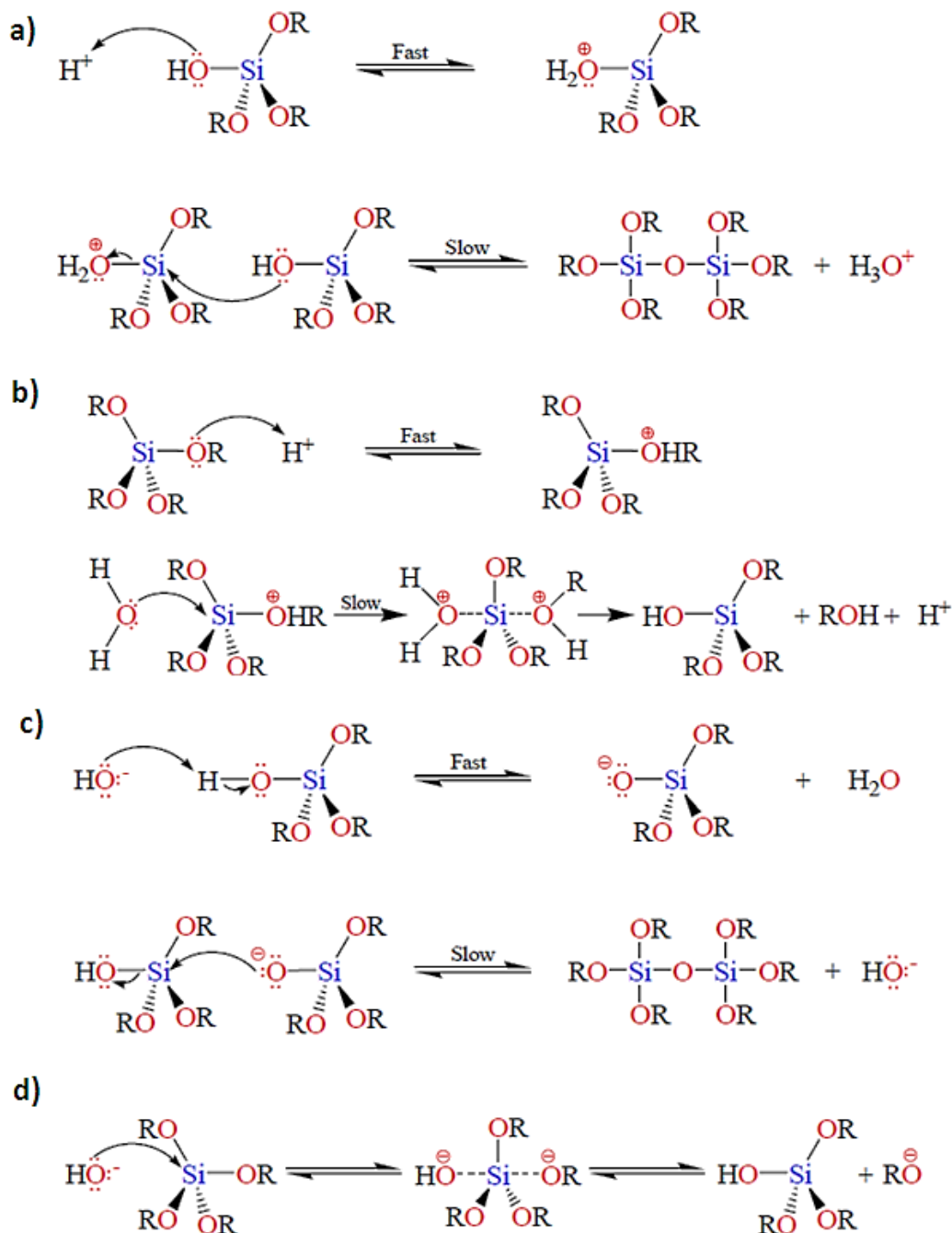


Figure 1. 19. Generic mechanisms for the formation and dissolution of silica. a) Condensation mechanism of an alkoxy silane using acidic catalyst, b) Hydrolysis mechanism of an alkoxy silane using acidic catalyst, c) and d) Hydrolysis and condensation mechanisms of an alkoxy silane using basic catalyst. Adapted from Alothman.⁸⁰

2. EXPERIMENTAL SECTION

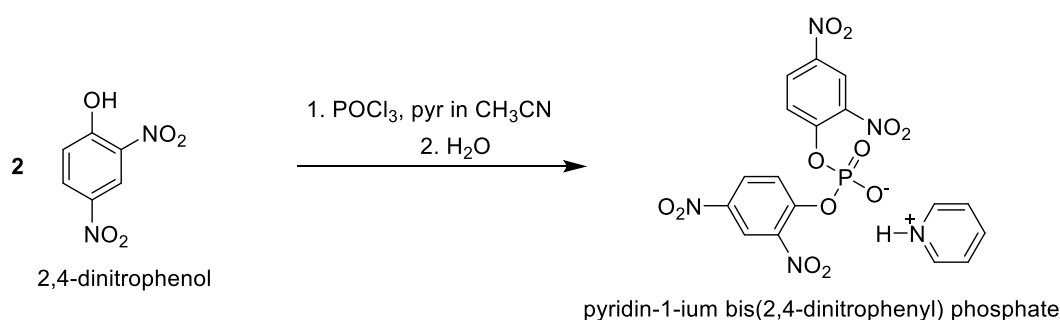
2.1 Materials

All reagents were obtained from common vendors and purified when needed. LnCl_3 solutions were prepared by the reaction between a known amount of Ln_2O_3 with an aqueous solution of HCl 2 molL^{-1} under heating and stirring. Care was taken to keep the pH at 5, no hydroxide was used. The desired volume was set with water and the final solution was stored in a refrigerator. When needed, the solvent was exchanged to ethanol by evaporation of water and addition of ethanol.

2.2 Synthetic procedures

2.2.1 Synthesis of *bis*(2,4-dinitrophenyl)phosphate (BDNPP)

Bis(2,4-dinitrophenyl) phosphate, **BDNPP**, was synthesized as reported by Bunton and Farber (Scheme 2.1).¹²⁵ Recrystallized (in CHCl_3) 2,4-dinitrophenol (2.77 g, 15 mmol) was mixed with distilled pyridine (2.5 mL, 31 mmol) in 30 mL of dry distilled acetonitrile under stirring, then 0.5 mL (5.36 mmol) of redistilled phosphoryl chloride was added in an ice-salt bath. The reaction mix was stirred for 15 min and then poured into ice-water (200 mL). The solid formed was filtrated off and washed several times with ice cold water to remove the excess of pyridine. The crude product was recrystallized in a mixture of acetone-ether (50% v/v) to afford 1.90 g (3.73 mmol, 70% yield) of the phosphate ester, mp 155-159°C (lit. 159-160°C).



Scheme 2. 1. Synthesis of *bis*(2,4-dinitrophenyl)phosphate (BDNPP).

2.2.2 Synthesis of the non-functionalized Porous Silica Material (PSiM) used for preparing the heterogeneous catalyst

The synthesis of PSiM (MCM-41-type) was carried out as follow: 6.0 g (16.5 mmol) of cetyltrimethylammonium bromide (CTAB) was mixed with 81 mL of NaOH 1 molL^{-1} and 162 mL

of H₂O and stirred for 3 h to give a homogeneous solution. Then, 30 mL (134 mmol) of tetraethyl orthosilicate (TEOS) was added dropwise under stirring (Figure 2.1) for 6 h and mixed for 24 h at room temperature. The white powder was filtered, washed with MilliQ water until the flow through had a conductivity lower than 10 μScm^{-1} and dried in the stove for 12 h at 60°C. Finally, the powder was calcinated at 550 °C for 6 h with a heating rate of 1 °C min⁻¹. After many synthetic rounds, is observed that this method gives on average 6 grams of PSiM.

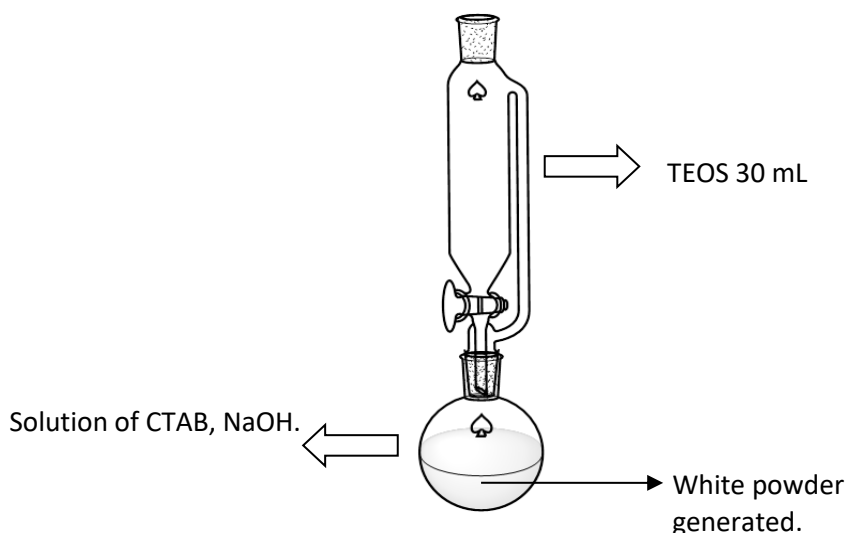


Figure 2. 1. Apparatus used for synthesis of PSiM

2.2.3 Functionalization of PSiM

The functionalization process is made in two stages: activation of the surface of the PSiM to generate the major quantity of silanols groups susceptible to functionalization, followed by the incorporation of the organic moiety.

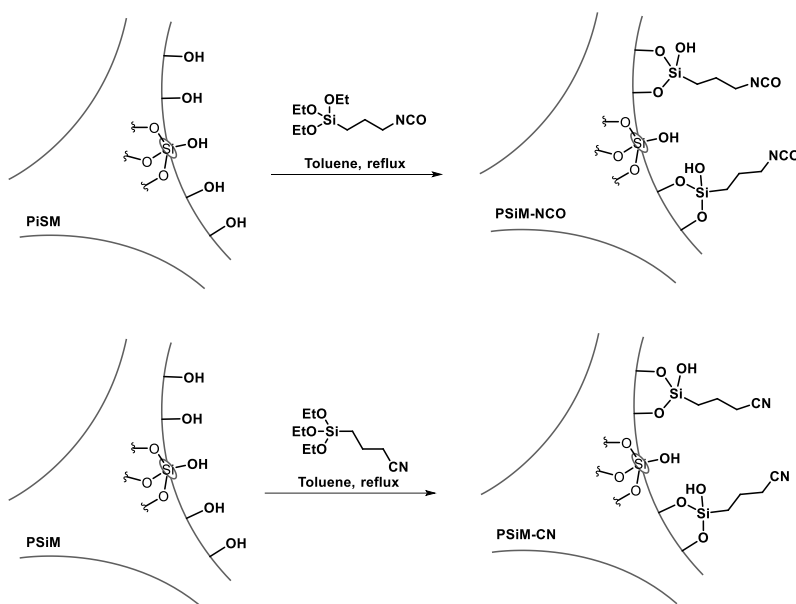
- Surface activation

In an ice-bath was added 6 mL of H₂O₂ 35% and 14 mL of H₂SO₄ 98% to PSiM (1.0 g). This mix was stirred for 10 min and the solid was filtered off. The silica was washed with abundant water (5x125 mL) and dried at 60°C for 12 h.

- Incorporation of the organic moiety onto the surface of PSiM

The PSiM modification was carried out according to a reported method (Scheme 2.2)¹²⁶: 300 mg of the active PSiM and 15 mL of dry toluene were placed in a two-neck round-bottom

flask connected to a Dean-Stark system (Figure 2.2). The system was saturated with argon atmosphere to provide anhydrous conditions. Then, 0.50 mL of 3-(triethoxysilyl)propylisocyanate (2.0 mmol) or 3-cyanopropyltriethoxysilane (2.2 mmol) was added to the reaction mix. The system was refluxed under stirring for three hours. The Dean-Stark was allowed to take out the ethanol generated in the reaction. After three hours, the product, PSiM-CNO or PSiM-CN, was filtered and washed with ethyl ether and toluene. Solvent vestiges were removed under vacuum and heating, and the product was stored in a desiccator.



Scheme 2. 2. Synthesis of PSiM-NCO and PSiM-CN from non-functionalized PSiM.

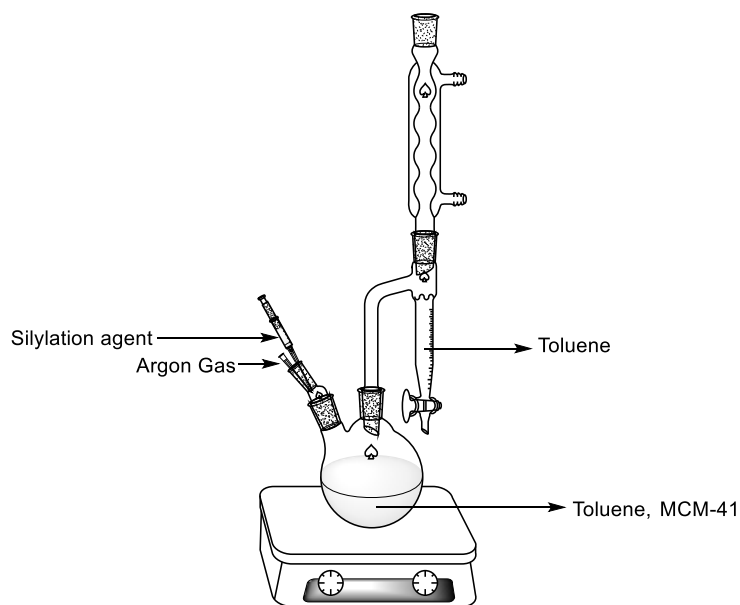
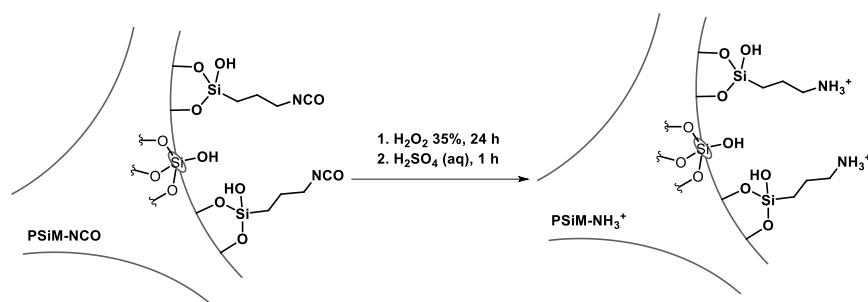


Figure 2. 2. Apparatus used for the functionalization of PSiM.

2.2.4 Hydrolysis of the isocyanate group on the surface of the PSiM-NCO

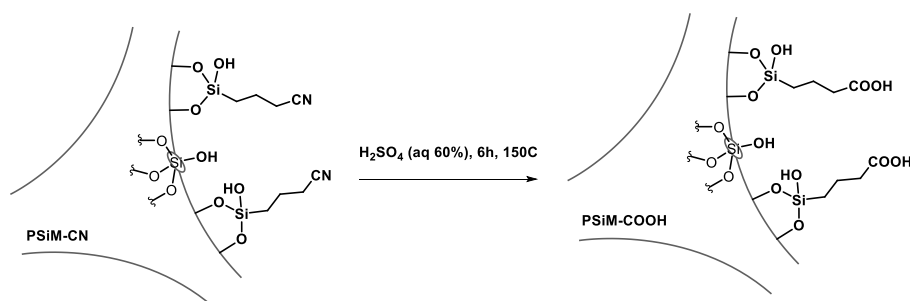
The modified PSiM-NCO (300 mg) was left to react in a 100 mL Erlenmeyer with 15 mL of H_2O_2 35% under vigorous stirring for 24 h at room temperature. Then, 2 mL of H_2SO_4 2 mol L^{-1} was added and stirred for 1h (Scheme 2.3). The silica was filtrated and washed with abundant water and dried under room temperature for 24 h.



Scheme 2. 3. Hydrolysis of isocyanate on PSiM-NCO.

2.2.5 Hydrolysis of the cyanate group on the surface of the PSiM-CN

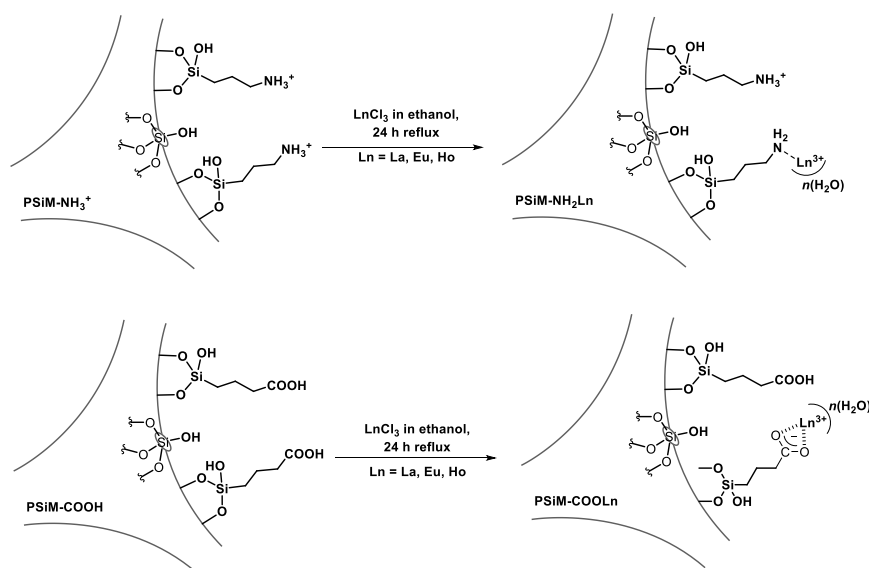
The modified PSiM-CN (300 mg) was let to react in a 100 mL one-neck round-bottom flask with 40 mL of H_2SO_4 60% v/v under vigorous stirring for 3 h at 150 °C (Scheme 2.4). Solids were filtered-off, washed with abundant water, and dried at room temperature for 24 h.



Scheme 2. 4. Hydrolysis of cyano group on PSiM-CN.

2.2.6 Lanthanide (III) coordination to PSiM-NH₂ and PSiM-COOH

The PSiM-NH₂ or the PSiM-COOH obtained as described above was mixed with 10 mL of an ethanolic solution of $\text{LnCl}_3 \approx 0.1$ mol L^{-1} (Scheme 2.5) in a one-neck round-bottom flask and refluxed under magnetic stirring for 24 h. The PSiM-NH₂-Ln and the PSiM-COOLn were filtered and washed with ethanol. Then, the product was dried at 70 °C for 6h under vacuum.



Scheme 2.5. Lanthanide (III) coordination to the modified PSiM-NH₃⁺ and PSiM-COOH.

2.3 Characterization

The synthesized materials were characterized by different techniques that all together intend to map out the physical-chemical properties of PSiM and its functionalized forms.

2.3.1 Infrared spectroscopy

FT-IR spectra were determined on a Varian Excalibur 3100 FT-IR equipped with a DTGS detector. Analyses were carried out in the Catalysis and Interfacial Phenomena Laboratory (LACFI) at UFSC. Each sample was dried for 12 h at 100°C prior preparation of KBr disks submitted to analysis. Each spectrum is the result of 64 interferograms with a resolution of 1.0 cm⁻¹.

2.3.2 Thermal Analysis

TG/DSC curves were obtained on a Mettler Toledo TGA/DSC1 - STAR^e system, using synthetic air atmosphere, with a flow of 50 mL min⁻¹, temperature range 25-750°C and heating rate of 10 °C min⁻¹. Approximately 5 mg of sample were used in each analysis, which were placed in alumina container. Analyses were carried out in the thermal analysis laboratory at the chemistry department of the UFMG.

2.3.3 Elemental Analysis Carbon, Hydrogen, Nitrogen (CHN)

Elemental analyses were carried out in duplicate on a PerkinElmer CHN analyzer using tin capsules and 2 to 3 mg of sample. Analyses were carried out in the elemental analysis laboratory at the chemistry department of the UFMG

2.3.4 Total-reflection X-ray fluorescence

Determination of Ln concentration in the suspension was performed using a portable full reflection X - ray fluorescence spectrometer, S2 PICOFOX™ TXRF (Bruker Nano GmbH, Germany). The spectrometer is equipped with a Mo K α 17.5 keV tube and operates under the conditions: 600 μ A, 50 kV, 50 W. The spectrometer has a multi-layer monochromator and a silicon drift detector - SDD with an active area of 10 mm². The radiation beam strikes the sample on a rectangular surface of about 7 x 0.1 mm². The resolution of the detector is better than 160 eV at 10 kPa (Mn K α). The data acquisition time was 500 s per sample. Processing of X-ray spectra and counting of fluorescence peaks were performed using SPECTRA software version 7.0 (Bruker Nano GmbH, Karlsruhe, Germany). The L1 α line was used for determination of the Ln concentration. Analyses were in triplicate.

Each sample (15 mg) was prepared by addition of 200 μ L of an internal standard (100.0 mg L⁻¹) of Ga to give a final concentration of 10.0 mg L⁻¹. The volume of the mixture was adjusted to 2 mL with Triton X-114 and homogenized by vortexing. Then, a 10.0 μ L aliquot was transferred to a sample holder and dried at 60°C for 10 min.

2.3.5 Powder X-ray diffraction (XRD)

Powder X-ray diffraction (XRD) were measured at 25 °C. Home source data were collected on a PANalytical - EMPYREAN diffractometer using Cu K α radiation, scanning the 2 θ from 2 to 10°, at 0.0131° steps and scan rate of 0.31 θ min⁻¹. Synchrotron data were recorded at the XRD1 beamline at the National Synchrotron Light Laboratory (LNLS, Brazil) at 6.5 keV.^{126, 127}

2.3.6 Nitrogen Adsorption-Desorption at 77 K (BET analysis)

The adsorption-desorption isotherms at 77 K were obtained in a volumetric adsorption equipment: Commercial Autosorb-1MP (Quantachrome Instruments Corp). Prior to analysis, the samples were degassed at 150 ° C for 16 h. The specific surface area was calculated by the BET method.

2.3.7 Electron Microscopy

Scanning electron microscopy (SEM) was carried out on a Quanta 200FEG FEI 14 2006 using an acceleration voltage of 15 kV. Samples were deposited on a carbon ribbon and metallized with 5 nm of platinum for the morphological analyses. Transmission electron microscopy (TEM) images were obtained on a G2-20 - SuperTwinTecnai FEI equipment. TEM samples were

dispersed in anhydrous ethanol and sonicated for 10 min before deposition and drying over Holey Carbon Films on 400 Mesh Copper Grids. SEM and TEM analysis were performed at the Microscopy Center at UFMG.

2.3.8 Particle size, zeta potential and conductivity

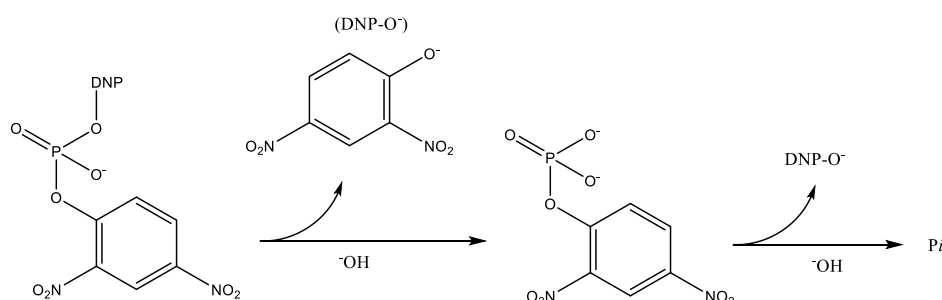
Dynamic light scattering (DLS), zeta potential and conductivity assays were measured on a ZetaSizer Nano ZS-90 (Malvern). Analyses were performed at 25 °C for non-sedimented particles after 5 min of dispersion (1.0 mg mL^{-1}) in water or buffer solution. Samples assayed by DLS were measured 10 times with 10 accumulations of 5 s each in 1 cm pathlength polystyrene cuvettes. Zeta potential and conductivity were assayed in folded capillary zeta cells (Malvern), each sample was measured 5 times with 5 accumulations. The ZP data was obtained immediately after the formation of the dispersion.

2.3.9 Solid-State Nuclear Magnetic Resonance (NMR)

Solid ^{29}Si Nuclear magnetic resonance were performed at the Nuclear Magnetic Resonance Laboratory of UFRJ using a 4 mm probe, relaxation delay (d1) of 4 seconds, 5 KHz rotation, number of scans (NS) of 4K

2.4 Kinetic studies

Kinetics were carried out using two similar reactor system (Figures 2.3 and 2.4). Non-functionalized and functionalized PSIM (10-50 mg) were mixed with 20.0 mL of buffer solution 0.1 mol L^{-1} , then the reactor was closed, and its contents pumped through a flow cuvette placed in an UV-Vis spectrometer. Once the system was filled up with the solution and the temperature stabilized at 25°C, 50 μL of a CH_3CN solution 5.0 mmol L^{-1} of **BDNPP** (Scheme 2.6). was added to start the kinetic experiment. Spectra (range 250-600 nm, resolution 1.00 nm) were taken over time



Scheme 2. 6. Hydrolysis reaction of *bis*(2,4-dinitrophenyl) phosphate (BDNPP).

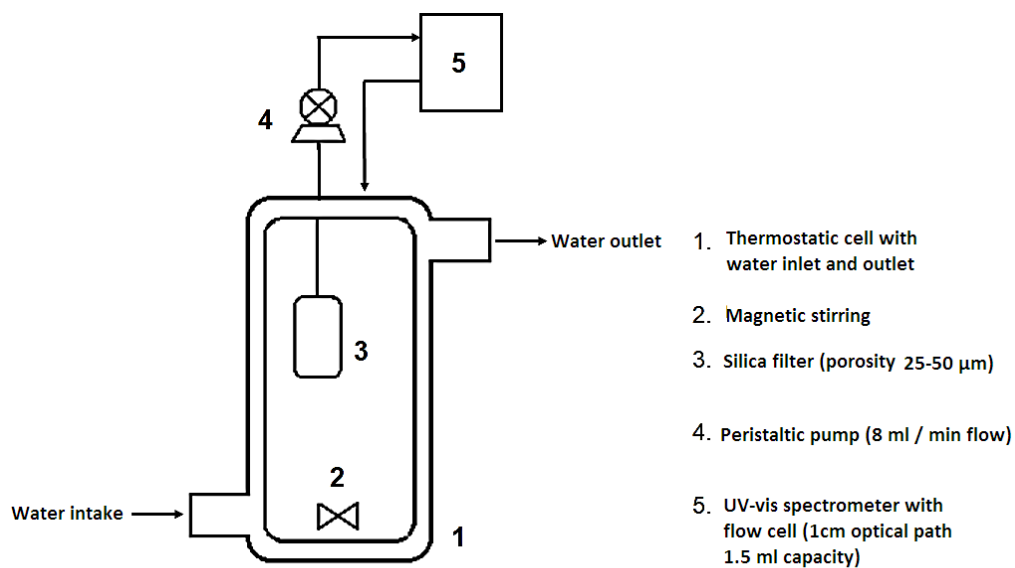


Figure 2. 3. System 1 (reactor) used to monitor the hydrolysis of BDNPP in the presence of the silica materials (PSiM, PSiM-NH₃⁺ and PSiM-NH₂La).

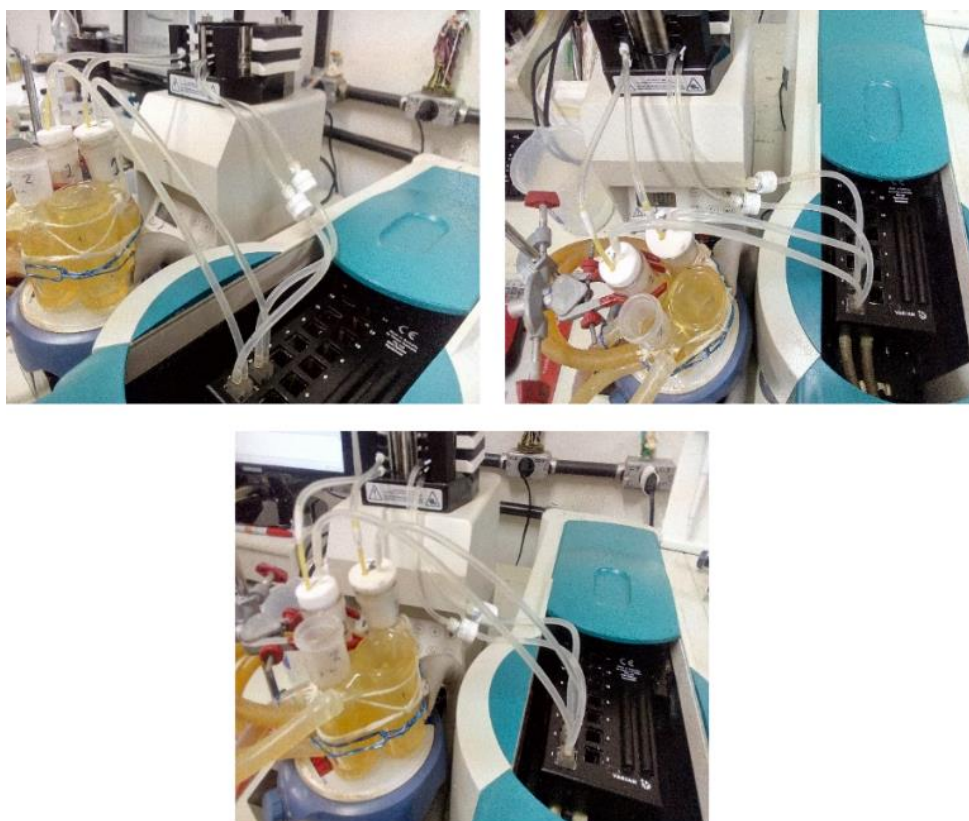
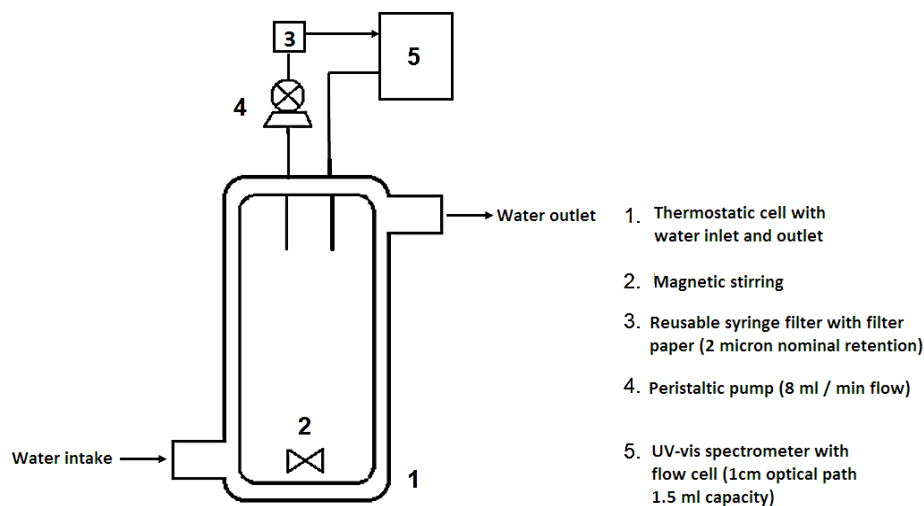


Figure 2. 4. System 2 (reactor) used to monitor the hydrolysis of BDNPP in presence of the silica materials (PSiM-COOH and PSiM-COOHLn).

System 1 (Figure 2.3) was used for the kinetic studies in chapters 3 and 4, which the PSiM amount was 50 mg. System 2 (Figure 2.4) was used for the kinetic studies in chapters 4 and 5 for amount up to 50 mg of PSiM, due to the inner limitation of the system to handle higher charges of the catalyst (system clogging, flow stop).

Reactions were carried out as described above at different pH and buffer solutions (Table 2.1). The concentration was the same for all buffer solutions (0.1 molL⁻¹). The reaction was followed for 8000 min with four-time stages (Table 2.2). The pH of the buffer solution was measured before and after its use and the change was below 0.05 pH units, indicating that the concentration of H₃O⁺ was constant during the experiments.

Table 2. 1. Buffer solution used in the kinetic studies.

Buffer	pH range
ACETATE	3.5-5.7
PIPES	6.0-7.2
HEPES	7.4-8.4
CHES	8.6-9.8
CAPS	10.0-11.0

Table 2. 2. Typical intervals used to set up the spectra acquisition in the kinect experiment.

Stage	Cycle (min)	Stop (min)
1	3.0	60
2	10.0	1000
3	15.0	3000
4	30.0	8000

2.4.1 Catalyst Reuse

Two methods were used to evaluate the capacity of reuse of the catalyst after the first use at pH 8.1. In the first method (hydrated PSiM), the remaining solution was eliminated, and the system was washed with buffer solution until the spectrum of the solution did not present any residual absorption. Then, a new buffer solution was added (pH 8.1) and 50 µL of a solution 5.0 mmol L⁻¹ of substrate **BDNPP** was injected to start the kinetics. In the second method (dry PSiM), the remaining solution was eliminated, and the system was washed with buffer solution until

the spectrum of the solution did not present any residual absorption. Then, the silica material was dried in an oven at 80 °C for 24 h, and the material was placed back in the flow system with a new buffer solution (pH 8.1) before starting the kinetics with 50 µL of a solution 5.0 mmol L⁻¹ of **BDNPP**.

2.4.2 Activation (hydration) of PSiM

To validate the influence of the method of hydration, two methods were used for hydration of PSiM. In the first method, the PSiM (30 mg) was hydrated with 20 mL of buffer solution (HEPES 0.1 mol L⁻¹ pH 8.0, on a 50 mL conical tube) for 1500 min. Then, 50 µL of a solution 5.0 mmol L⁻¹ of **BDNPP** was added to start the kinetics. In the second method, PSiM (10 mg) was placed on the system with 20 mL of buffer solution (HEPES 0.1 mol L⁻¹ pH 8.0) and was let to hydrate for 1500 min. Then, 50 µL of a solution 5.0 mmol L⁻¹ of **BDNPP** was added to start the kinetics.

RESULTS AND DISCUSSION

Following sections discuss the characterization and catalytic properties of the different synthesized materials. The discussion was separated by functional group on the surface of the PSiM and their catalytic properties.

Non-functionalized PSiM was prepared according to the method of Ribeiro-Santos et al.¹²⁸ The surface hydroxyl groups were functionalized using 3-(triethoxysilyl)propyl isocyanate or 3-cyanopropyltriethoxysilane to afford PSiM-NCO and PSiM-CN, respectively.⁸⁸ The isocyanate groups in PSiM-NCO were converted to the amino form (PSiM-NH₂) in the presence of 35% H₂O₂ followed by treatment with 2 mol L⁻¹ H₂SO₄. The cyano groups in PSiM-CN were converted to carboxyl (PSiM-COOH) by treatment with H₂SO₄ (60% v/v). Then, coordination of the functionalized silica materials with Ln³⁺ yielded PSiM-NH₂Ln and PSiM-COOLn.

Materials were characterized in relation to composition, morphology and properties using the following techniques: Infrared spectroscopy, Thermogravimetric Analysis (TGA), Differential Scanning Calorimetry (DSC), Elemental Analysis, Total-Reflection X-Ray Fluorescence (TXRF), adsorption of nitrogen gas to determine the surface area (BET method), Scanning and Transmission Electron Microscopy, and Dynamic Light Scattering. The catalytic properties of the materials were determined for kinetic studies on the hydrolysis of bis(2,4-dinitrophenyl)phosphate (BDNPP).

3 PSiM FUNCTIONALIZED WITH AMINO GROUPS AND ADORNED WITH LA (III)

This chapter first describes the characterization of PSiM-NH₃⁺ and PSiM-NH₂La materials. Then, the catalytic properties of these materials on the hydrolysis of BDNPP is presented.

3.1 Characterization of the PSiM and its amino and lanthanum forms.

Materials were characterized in relation to their composition, morphology and properties.

3.1.1 Infrared spectroscopy

Figure 3.1 shows the FT-IR spectra of PSiM and PSiM based hybrid materials. The strongest band is observed at 1080 cm⁻¹ for the asymmetric (ν_{as} , Si-O-Si) stretching vibration of the mesoporous framework, another characteristic band is the symmetric stretching vibration at 795 cm⁻¹ (ν_s , Si-O-Si). These observations show the success of the hydrolysis and copolymerization steps in the synthesis of PSiM. Figure 3.2 depicts the different silanol types present on the PSiM and their typical IR absorption bands.

The bands near 2950cm⁻¹ for the modified PSiM (Figure 3.1b red and blue) are assigned to the asymmetric and symmetric stretching vibrations of methylene groups, suggesting that the incorporation of the aliphatic chain to the PSiM framework has been successfully achieved. In line with these observations, comparing the spectra of PSiM with its amino functionalized forms, new bands are seen around 1570 cm⁻¹, which were assigned to the N-H bending peak of the organic moiety (Figure 3.1c). Figure 3.1b shows that the intensity on the region of the different silanol types on the PSiM (Figure 3.2) are affected by functionalization. The greatest intensity change regard the non-functionalized PSiM is observed for PSiMNH₂La (Figure 3.1b, blue) in agreement with the capacity of the La(III) ion to recruit water molecules. On the other hand, both organic functionalized forms PSiM-NCO (Figure 3.1b, green) and PSiM-NH₃⁺ (Figure 3.1b, red) present a decrease on the intensity comparing with the base PSiM (Figure 3.1b, black) as expected due to some silanols groups on the surface of PSiM are interchanged by organic moieties.

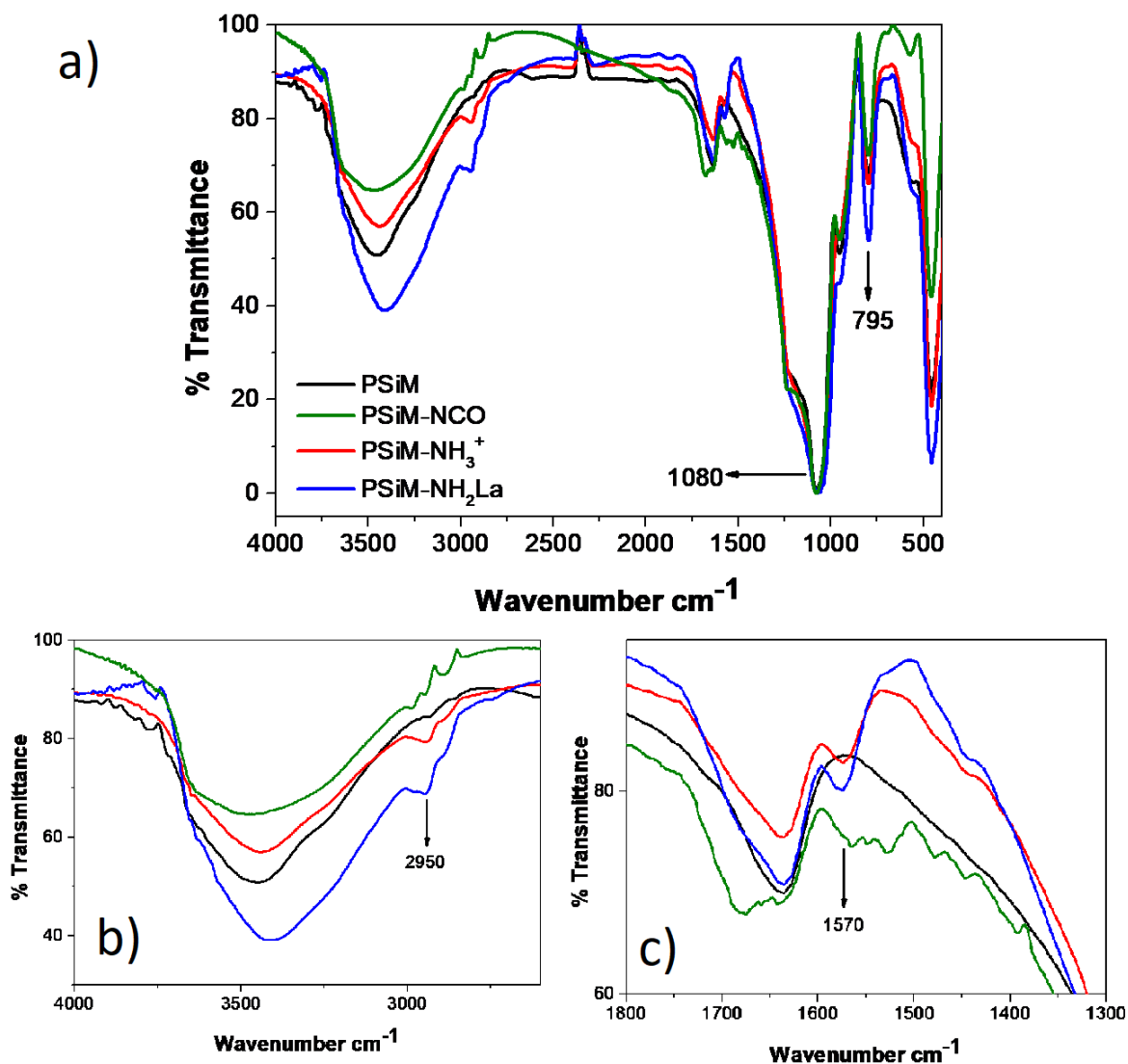


Figure 3. 1. The FT-IR spectra of PSiM (black), isocyanate(green) and amino(red) functionalized forms and its lanthanide complexes (blue). a) FT-IR spectra region of 4000-400 cm^{-1} , b) Close-up of FT-IR spectra at 4000-2600 cm^{-1} showing the peak at 2950 cm^{-1} (asymmetric and symmetric stretching vibrations of methylene groups), c) Close-up of FT-IR spectra at 1800-1300 cm^{-1} showing the peak at 1570 cm^{-1} (the N-H bending peak).

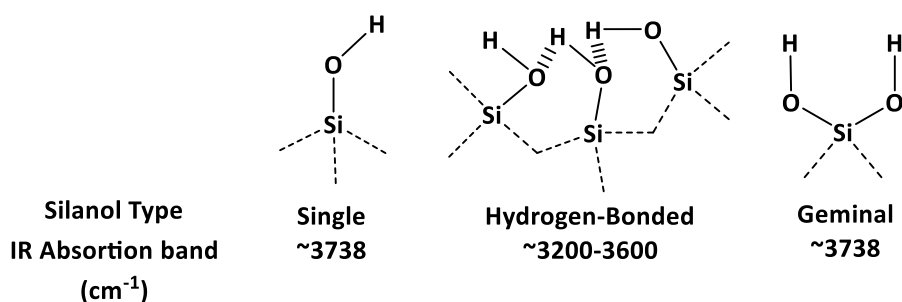


Figure 3. 2. Typical IR Absorption bands for the different silanol types present on the PSiM.

3.1.2 Thermo gravimetric analysis (TGA)

Figure 3.3 illustrates TGAs for PSiM and its functionalized forms in air. Comparisons between TGA for PSiM and its functionalized forms show variations in relation to the quantity of adsorbed water and organic composition. Both are consistent with hydroxyl functionalization as described for other silica materials.^{129, 130} Functionalization affords a less hydrated material and the weight loss (~8%) between 250 and 500 °C refers to the combustion of the organic groups. The amount of organic material was calculated by subtracting the degree of PSiM dehydroxylation (~4%) in the non-functionalized material from the total mass loss between 160 and 700 °C (12%) for the functionalized PSiM. The chemical composition and degree of functionalization observed by thermal analyses agreed well with infrared and elemental analyses (discussed in section 3.1.4).

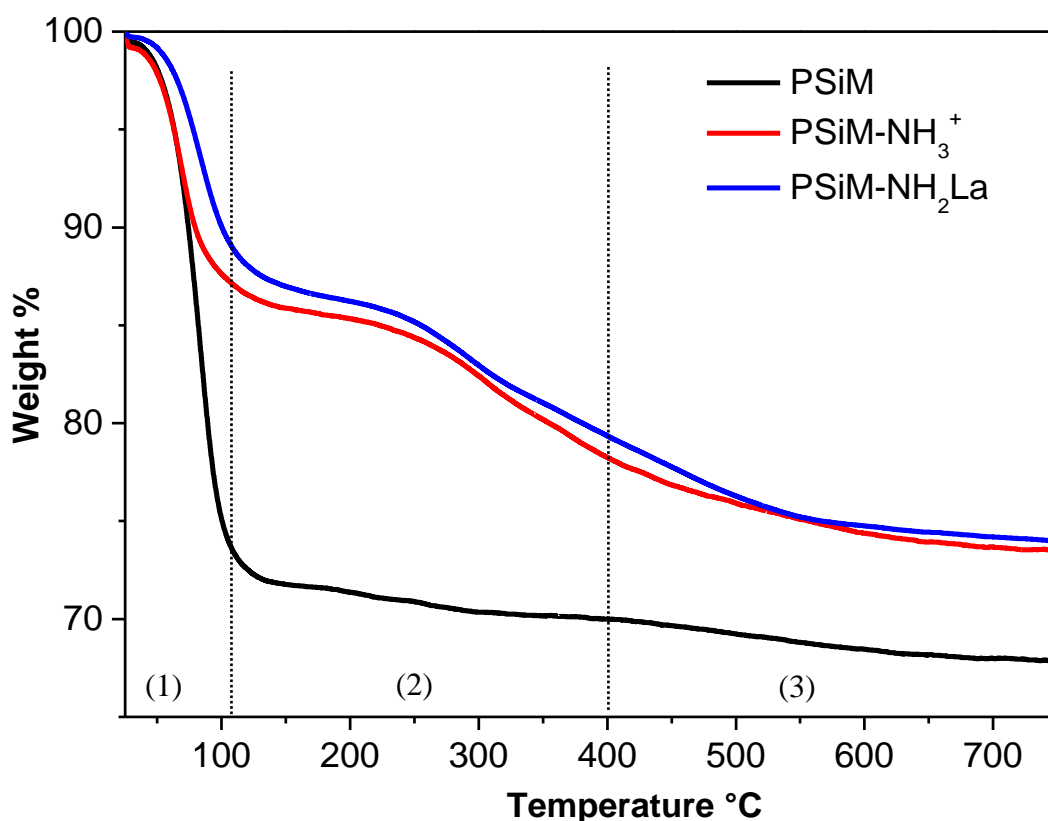


Figure 3. 3. Thermograms of PSiM (black), PSiM-NH₃⁺(red), and PSiM-NH₂La (blue) in air. The different regions indicated correspond to (1) water desorption, (2) degradation of the organic moiety when present, and (3) condensation of silanol groups.

3.1.3 Differential Scanning Calorimetry (DSC)

The differential scanning calorimetry (DSC) gave information about the behavior of the thermal processes (Figure 3.4). PSiM presents an endothermic event from 25-150°C, which is related with the mass loss attributed to desorption of water (Figure 3.3 region 1).

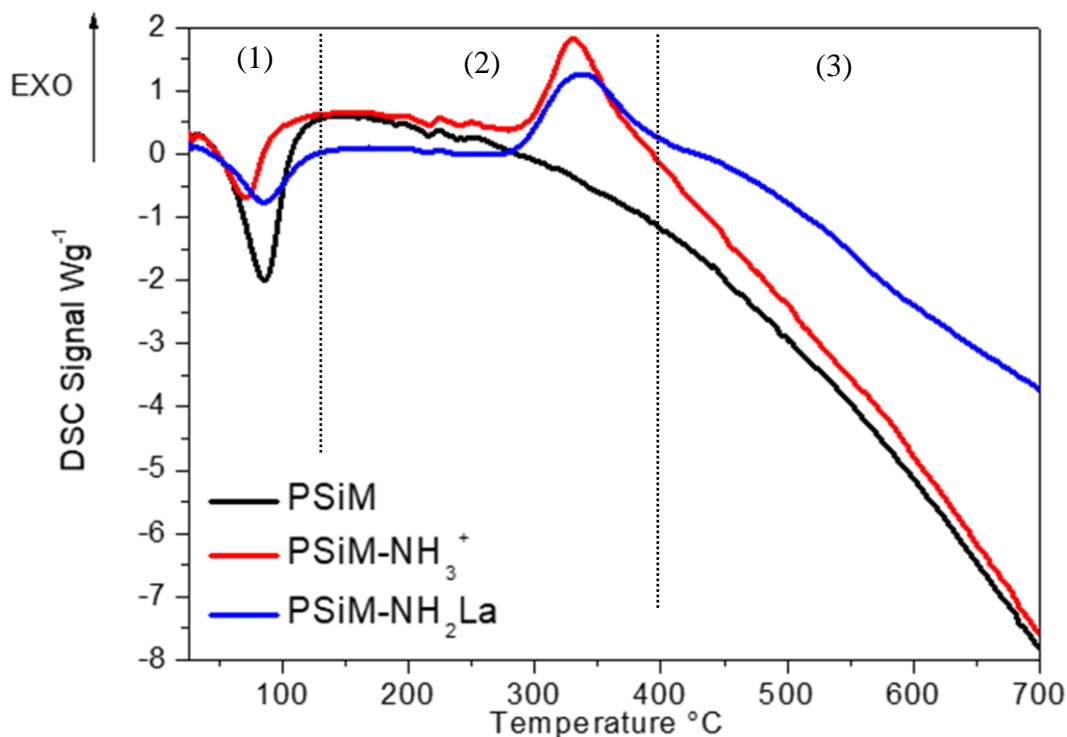


Figure 3. 4. Differential scanning calorimetry curves for PSiM (black), PSiM-NH₃⁺(red), and PSiM-NH₂La. The different regions indicated correspond to (1) water desorption, (2) degradation of the organic moiety when present, and (3) condensation of silanol groups.

The endothermic nature of the desorption is a reverse process of the exothermic adsorption, which can be explained by two reasons: (i) adsorption leads to a decrease in the residual forces on the surface of the adsorbent, which causes a decrease in the surface energy of the adsorbent. Therefore, adsorption is always exothermic; and, (ii) ΔS of adsorption is negative, because a molecule adsorbed on a solid surface has its movement restricted. Now for a process to be spontaneous, ΔG should be negative. Since ΔS is negative, ΔH has to be negative to compensate and provide a negative ΔG . Hence, adsorption is always exothermic.

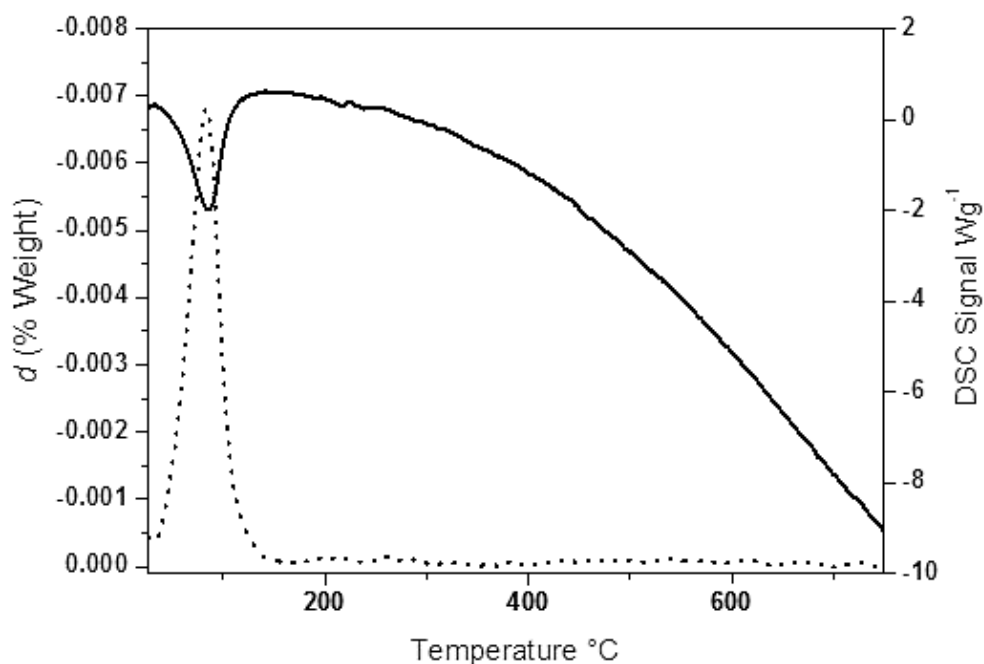
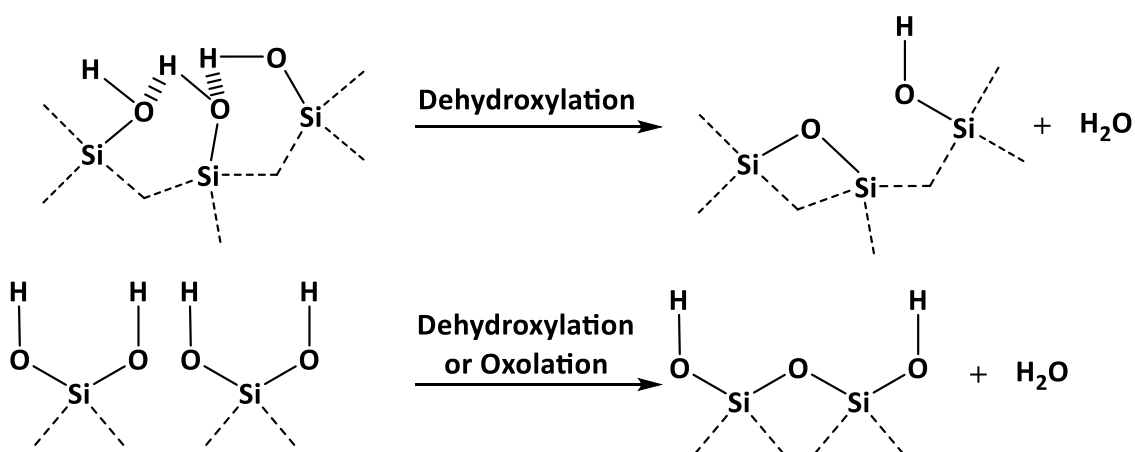


Figure 3. 5. Derivate of the TGA (dotted line) and DSC (solid line) curves of PSiM.

The DSC curve for PSiM also present a constant endothermic process above 250°C, the rate of this process does not change up to 700°C (derivate of the weight percentage in Figure 3.5). To explain this phenomenon is important to consider the type of surface silanol groups present on PSiM (Figure 3.2). These silanol groups undergo dehydroxylation (oxalation condensation reaction in which an oxo bridged is formed between two metal centres) reactions (Scheme 3.1) that cause a constant mass decrease by loss of water molecule every time the reaction takes place.



Scheme 3. 1. Schematic representation of the dehydroxylation processes of SiOH groups in PSiM from two different types of silanol groups. Adapted from Zhao et al.¹³¹

The DSC curves of the modified PSiM-NH₃⁺ (Figure 3.6) and PSiM-NH₂La (Figure 3.7) presented the same events observed for PSiM, desorption of water molecules and dehydroxylation under endothermic processes. Compared to PSiM, an additional exothermic transition is found at 200-393°C for the PSiM-NH₃⁺ and 200-428°C for the PSiM-NH₂La; the final temperature is determined by the sign change in the DSC curve. The 35°C higher temperature to complete the reaction for PSiM-NH₂La is consistent with the coordination of the metal to the organic moiety that required more energy to decompose.

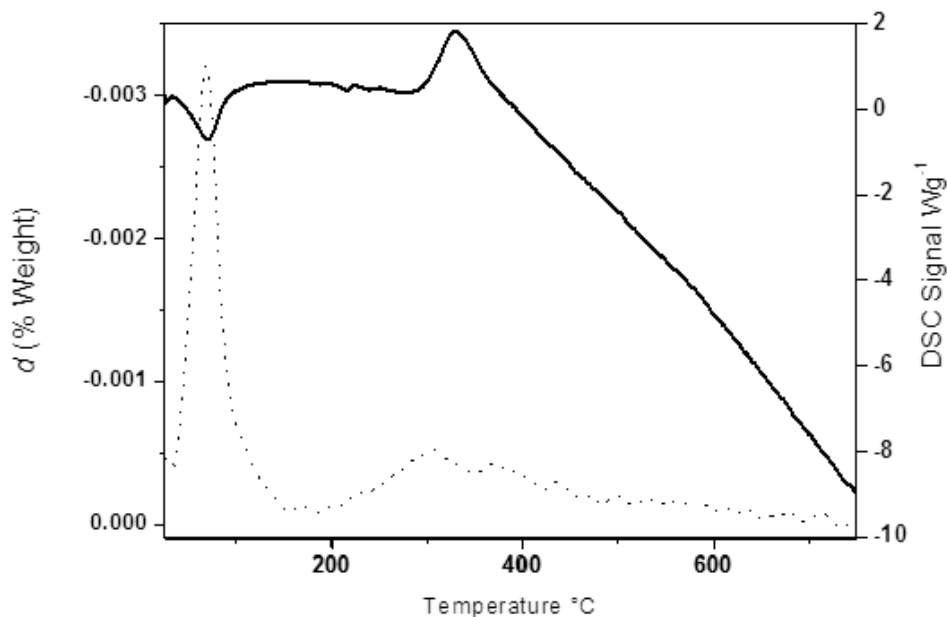


Figure 3. 6. Derivate of the TGA (dotted line) and DSC curves (solid line) of PSiM-NH₃⁺.

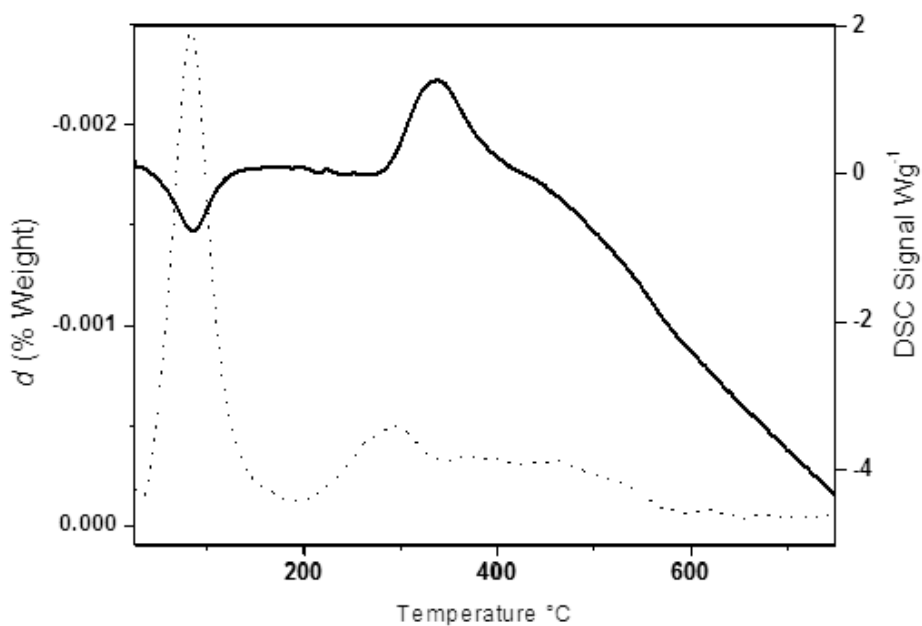


Figure 3. 7. Derivate of the TGA (dotted line) and DSC curves (solid line) of PSiM-NH₂La.

3.1.4 Elemental analysis

Table 3.1 presents the results for elemental analysis for PSiM and its functionalized forms. An increase in the percentage of carbon and nitrogen in each of the modified samples was observed as expected. For PSiM-NH₃⁺ was found 9.1% of carbon and nitrogen in a molar relationship of $4.2 \frac{\text{mol C}}{\text{mol N}}$ (calculations presented below), which is slightly higher than expected ($3.0 \frac{\text{mol C}}{\text{mol N}}$). This difference can be explained by contamination with organic matter. Since contamination relies on nitrogen-free organic solvents used in the synthetic procedures (e.g. toluene and ethyl ether), the nitrogen content was considered to determine the degree of functionalization as 8.2%. This value was determined from the amount of nitrogen (1.4 mmol N g⁻¹) and the molecular formulae for the organic moiety (C₃H₈N, M.W. 58.12). A similar method was used by Vunain et al.¹²⁹ to calculate the degree of functionalization on amino-functionalized MCM-41. Therefore, the amount of extraneous organic matter was lower than 2% according to the carbon content determined by elemental analysis.

Table 3. 1. Percentages from elemental analysis for PSiM and its functionalized forms.

Sample	Weight (mg)	%C	%H	%N
PSiM	1.884	0.30	3.16	0.15
PSiM-NH ₃ ⁺	3.149	7.13	2.30	1.97
PSiM-NH ₂ La	1.480	6.60	2.19	2.02

$$\frac{7.13 \text{ g C}}{12.011 \text{ g mol}^{-1}} = 0.59 \text{ mol C}$$

$$\frac{1.97 \text{ g N}}{14.007 \text{ g mol}^{-1}} = 0.14 \text{ mol N}$$

$$\frac{0.59 \text{ mol C}}{0.14 \text{ mol N}} = 4.2 \text{ mol C/mol N}$$

3.1.5 Total-reflection X-ray fluorescence (TXRF)

Total-reflection X-ray fluorescence (TXRF) is a sensitive method with several improvements regard to Energy Dispersion X-Ray Fluorescence (EDXRF).¹³² Basically, the internal arrangement of the TXRF provides higher sensitivity in relation to EDXRF. While the angle of incidence and fluorescence emission are approximately 45°/45° in the EDXRF, the TXRF is <0.1°/90°, as seen in Figure 3.8a.¹³² This causes the total reflection of the photons from the sample, and thus the

beam has minimal interaction with the sample holder on which are deposited only μL or μg of sample. This set up is attractive for detection of ultrace to traces elements.¹³³

Figure 3.8b depicts the TXRF spectrum for PSiM-NH₂La. The La³⁺ cation show signals for L _{α 1} and L _{β 1} emissions at 4.647 and 5.038 keV, respectively. Table 3.2 reports the results for three samples showing an amount of 15.5 g kg⁻¹ (or 1.5%) of La. The presence of other elements was found in trace quantities. However, the presence of chlorine is substantial, with a concentration of 4.4 g kg⁻¹ (or 0.44%), which implies that chloride ions from the LaCl₃ used in the synthetic procedure remains as La³⁺ counter ions.

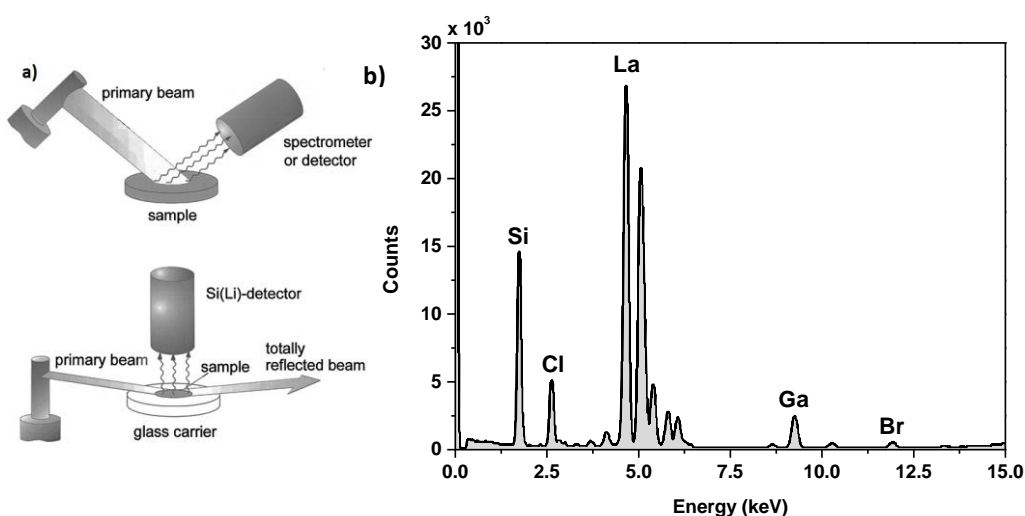


Figure 3. 8. a) Simplified arrangements used for conventional XRF (up) and for TXRF (down). Adapted from Klockenkämper and Bohlen¹³². b) Total-reflection X-ray fluorescence of PSiM-NH₂La.

Table 3. 2. Amounts of La determined in PSiM-NH₂La (triplicate) using TXRF

Sample	Amount of La (mg/kg)	Amount of Cl (mg/kg)
PSiM-NH ₂ La (a)	15270	4461
PSiM-NH ₂ La (b)	15700	4634
PSiM-NH ₂ La (c)	15530	4052
Average	15500	4382
Standard deviation	153	220

The amount in moles of lanthanum and chlorine were calculated analogously as the determination of organic matter by elemental analysis. Assuming 1 g of material and the atomic weight of the lanthanum as 138.9 g mol⁻¹, the quantity in moles of La³⁺ in this sample was:

$$\frac{0.015 \text{ g}}{138.9 \text{ g mol}^{-1}} = 0.108 \text{ mmol of La}^{3+}$$

The quantity in moles of Cl⁻ present in this sample is:

$$\frac{0.0044 \text{ g}}{35.45 \text{ g mol}^{-1}} = 0.124 \text{ mmol of Cl}^{-}$$

Near a unity ratio Cl⁻/La³⁺ is found, which implies a close relationship between these two ions. These mean that the chlorine ion works as counterion of the La³⁺ on the structure.

3.1.6 Determination of the surface area by adsorption of N₂ using the BET method

Nitrogen adsorption isotherms for PSiM, PSiM-NH₃⁺ and PSiM-NH₂La are shown in Figure 3.9a. These isotherms exhibit the typical shape for a mesoporous material (MCM-41 type) (Figure 1.11), type II-B isotherms with H4-type hysteresis loops at low relative pressure according to the IUPAC classification.⁸⁰ A H4-type hysteresis loop at low relative pressure is observed for all samples at relative pressures above 0.42, which are typical for nitrogen capillary condensation in narrow pores.⁸⁰ The specific area and pore size have been calculated by the Brunauer–Emmett–Teller (BET)¹³⁴ and are presented in the Table 3.3. Average pore diameters (Table 3.3) and pore size distributions, calculated using the BJH method (Figure 3.9b) reflect PSiM functionalization. Pore width narrowed from 13 to 26 Å in the nonfunctionalized PSiM to 6-18 Å in PSiM-NH₃⁺ and PSiM-NH₂La. Pores smaller than 13 Å width in the non-functionalized PSiM disappeared upon functionalization.

Table 3. 3. Surface area values obtain of the different samples of PSiM.

SAMPLE	BET surface area (m ² g ⁻¹)	D _p (nm)
PSiM	812	2.8
PSiM-NH ₃ ⁺	523	2.6
PSiM-NH ₂ La	432	2.6

As seen in Table 3.3, all mesoporous hybrid materials exhibit smaller specific area in comparison with the pure PSiM. This behavior is expected since the functionalization of the surface of PSiM partially occludes its hexagonal cavity as observed by others.

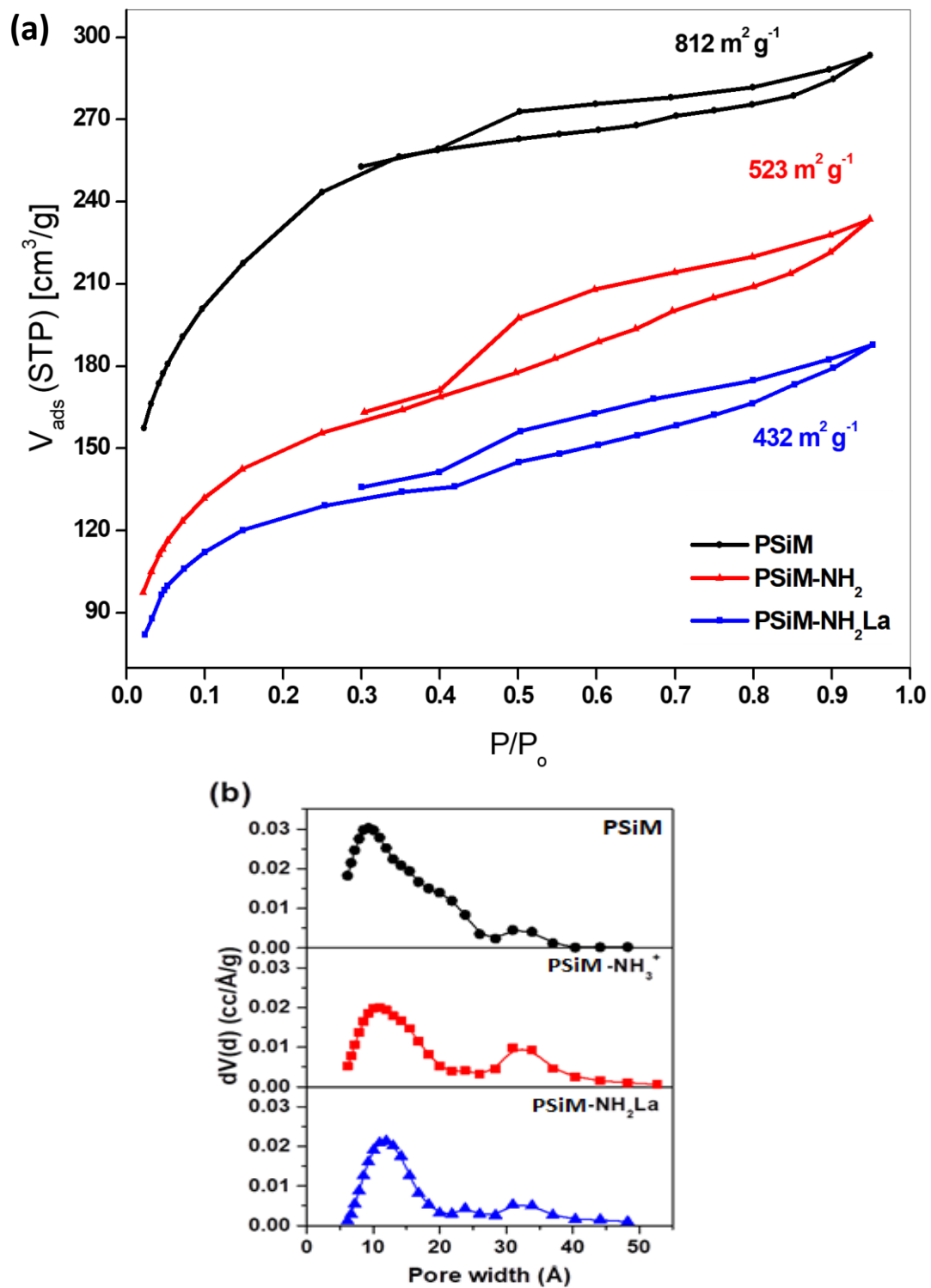


Figure 3. 9. Nitrogen adsorption-desorption isotherms (a) and pore size distribution by the DFT method (b) for PSiM before and after modification and attachment of the La³⁺ ion. In black the base material PSiM, in red the modified PSiM-NH₃⁺, and in blue the PSiM-NH₂La.

The quantity of organic chains by square meter can be obtained from the surface area of $523 \text{ m}^2\text{g}^{-1}$ determined by the BET method (Table 3.3) and the amount of organic chain per gram determined by elemental analysis:

$$\frac{1.4 \text{ mmol g}^{-1}}{523 \text{ m}^2\text{g}^{-1}} = 2.7 \text{ } \mu\text{mol m}^{-2}$$

In addition, the value of 0.1079 mmol of La^{3+} per gram of material determined by TXRF can be convert in area of material as following:

$$\frac{0.108 \text{ mmol g}^{-1}}{432 \text{ m}^2\text{g}^{-1}} = 0.25 \text{ } \mu\text{mol m}^{-2}$$

3.1.7 Scanning electron microscopy

Scanning Electron Microscopes (SEM) analyze a sample with a focused electron beam and deliver images with information about topography and composition. Figure 3.10 presents the secondary electrons SEM images (SE) for PSiM and its functionalized forms. Imaging with secondary electrons provides information about morphology and surface topography. The contrast is dominated by the so-called edge effect more secondary electron can leave the sample at edges than in flat areas leading to increased brightness there.^{135,136} Also it can be observed that the size of the PSiM base particles decrease from around $60 \text{ } \mu\text{m}$ (Figure 3.10a) to $20 \text{ } \mu\text{m}$ when the surface modification is carried out (Figure 3.10 b and c). However, as seen in the images at maximum magnification, the morphology and the topography of the modified materials remains the same after functionalization.

Figure 3.11 shows the Energy-dispersive X-ray spectroscopy (EDS, EDX, or XEDS) for the PSiM and its functionalized forms. This analytical technique offers elemental analysis and chemical characterization of samples. As expected, the only significant difference between the spectra for the PSiM- NH_3^+ and PSiM is a stronger signal at 0.28 keV for the k_α emission of the carbon atom in the former sample. In the spectrum for the PSiM- NH_2La signals are found for the chlorine (2.6 keV) and lanthanum atoms, although La emission was close to the detection limit. The TXRF, discussed earlier, offers data that are more reliable in this regard.

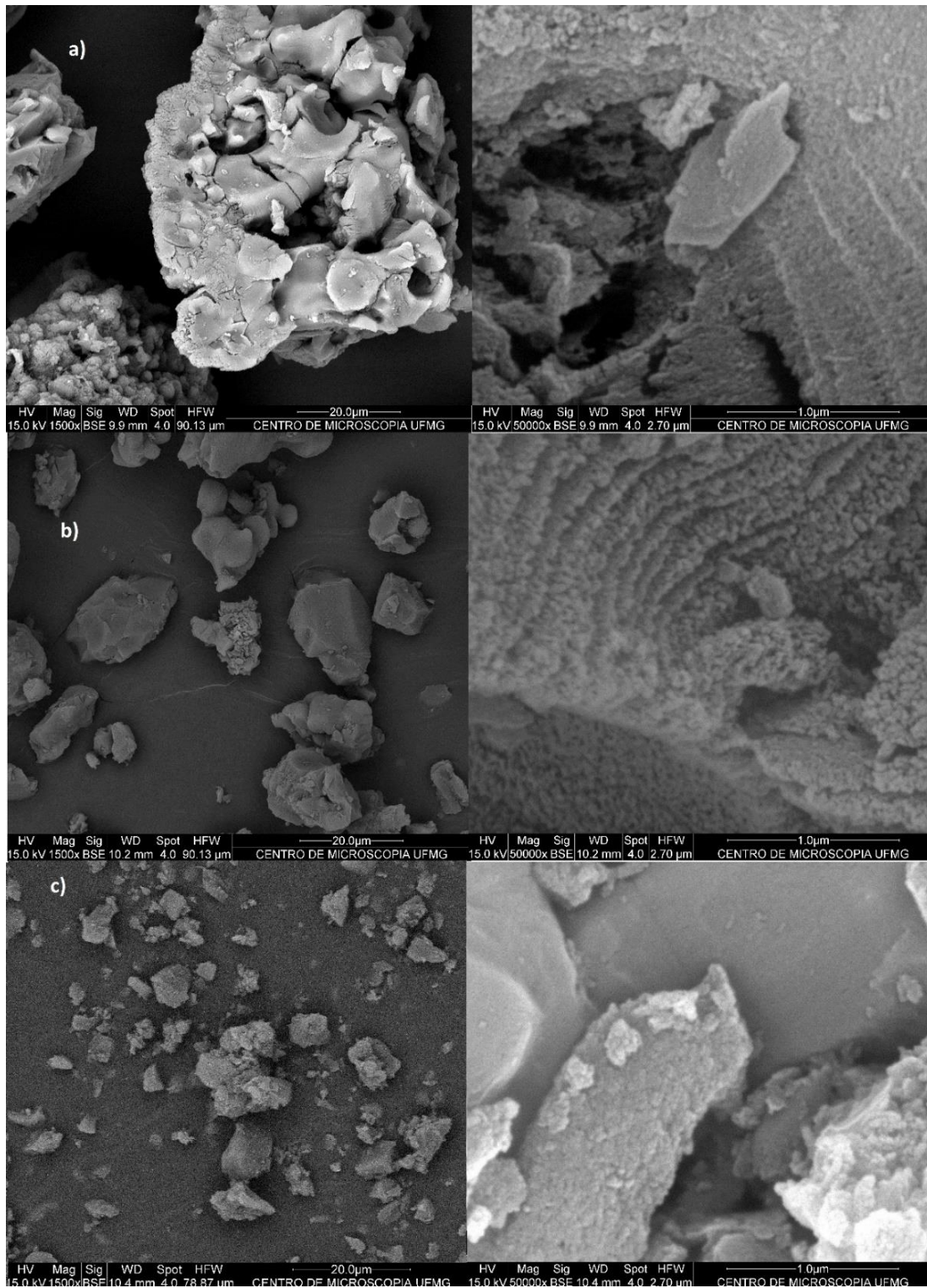


Figure 3. 10. Secondary electrons SEM images (SE) of a) PSiM, b) PSiM-NH₃⁺, and c) PSiM-NH₂La.

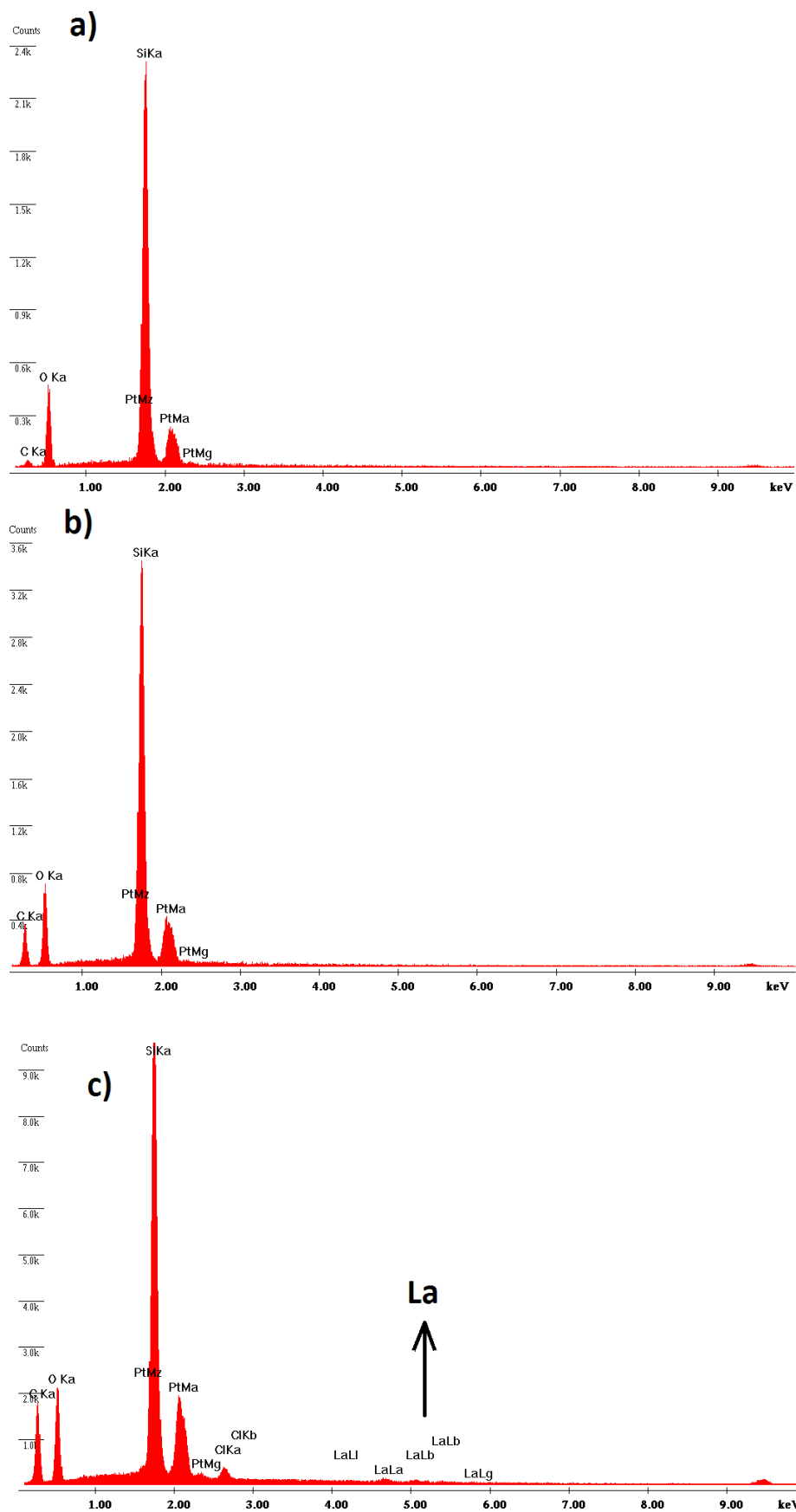


Figure 3. 11. Energy-dispersive X-ray spectrum for: a) PSiM, b) PSiM-NH₃⁺, and c) PSiM-NH₂La.

3.1.8 Transmission electron microscopy

Figure 3.12 shows TEM images for PSiM (Figures 3.12 a and b) and PSiM-NH₂La (Figures 3.12c and d). In the Figure 3.12a (into the square, zoom in the corner) is observed the hexagonal structure of the PSiM (MCM-41 type pores), which have an average diameter of 2.8 nm or 28Å. The same hexagonal structure from a different perspective is found in many places of the TEM image for PSiM-NH₂La (Figures 3.12 c and d), the square highlights one of these regions from where was determined an average pore diameter of 22 Å. Nevertheless, as seen on the images, most regions are disordered. This observation is agreement with the N₂ adsorption-desorption isotherm, that present a hysteresis that suggests N₂ condensation within interparticles and/or some impurity phases, such as lamellar mesostructures or agglomerate of particles.

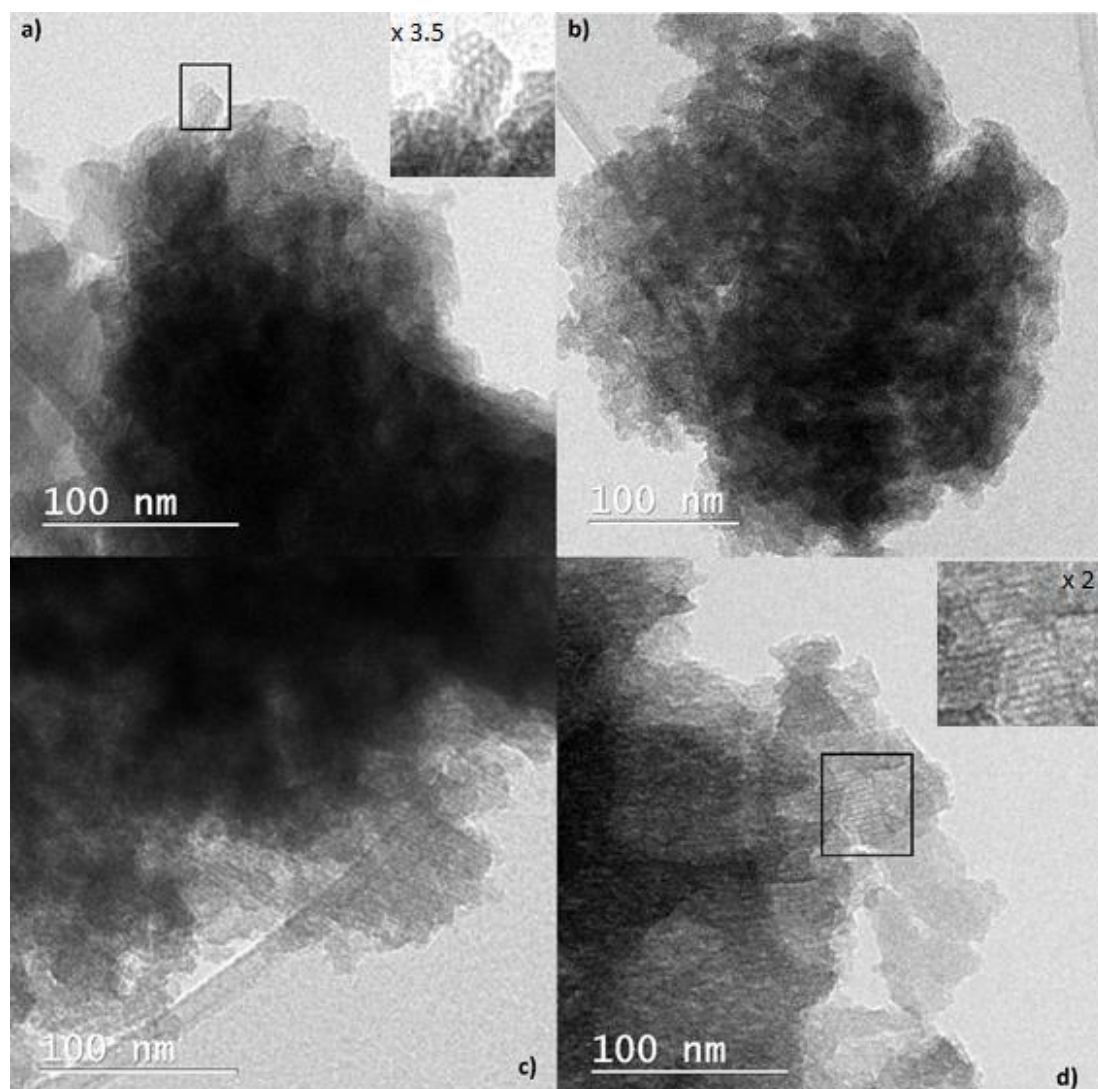


Figure 3. 12. Transmission electron microscopy (TEM images) a) and b) PSiM, c) and d) PSiM-NH₂La.

3.1.9 X-ray Power Diffraction (XRD)

As shown in Fig. 3.13, XRD diffractograms for PSiM and its functionalized forms display reflections for the plane (100) at 2θ values near 2.5° in our home source ($\lambda=0.1542$ nm), d_{100} about 3.5 nm (see calculations below), which is typical for materials with ordered hexagonal arrangements.^{85,137} As reported for other amino-functionalized porous silica materials,^{129,138} functionalization affects the scattering contrast between the pore channels and the silica walls, and the 2θ peaks are less resolved than in the corresponding non-functionalized material. Indeed, the 2θ peaks for (110) and (200) planes between 4° and 6° for the non-functionalized PSiM cannot be resolved in the XRD diffractograms for the functionalized materials.

$$n\lambda = 2d\sin\theta \quad (3.1)$$

$$1 \times 0.1542\text{nm} = 2d\sin(2.5) \quad (3.2)$$

$$\frac{1 \times 0.1542 \text{ nm}}{2 \times \sin\left(\frac{2.5}{2}\right)} = d \quad (3.3)$$

$$3.5 \text{ nm} = d \quad (3.4)$$

From this value, the hexagonal network parameter a_0 , which corresponds to the distance between the center of the pores, can be calculated.

$$a_0 = \frac{2d_{100}}{\sqrt{3}} \quad (3.5)$$

$$a_0 = \frac{2 \times 3.5 \text{ nm}}{\sqrt{3}} \quad (3.6)$$

$$a_0 = 4.04 \text{ nm} \quad (3.7)$$

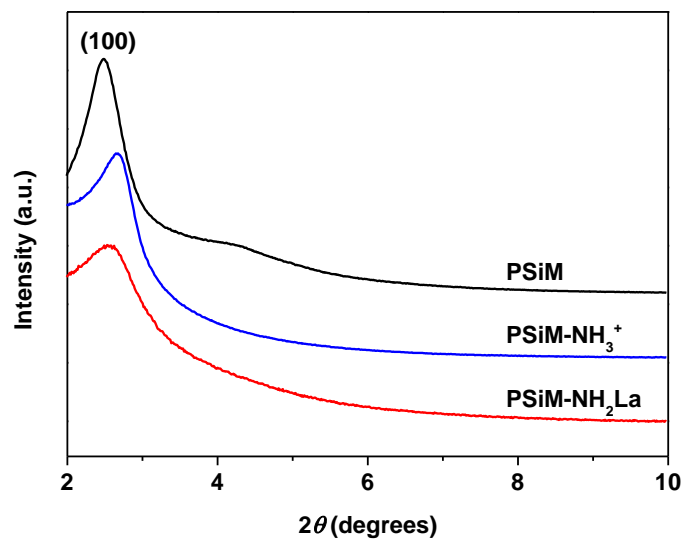


Figure 3. 13. XRD diffractograms for PSiM and its functionalized forms PSiM-NH₃⁺ and PSiM-NH₂La.

3.1.10 Zeta potential and conductivity

Next, we summarize important aspects for measurement of zeta potentials. Between particles in any suspension exists an attractive van der Waals interaction. That is why to prepare stable colloidal suspensions is necessary to introduce interactions that oppose these Van der Waals attractions. In an electrolyte solution, ions surround the particles and shield their surface charge offering the required stabilization. The distribution of counter ions near a charged surface can be described using Stern-Gouy-Chapman theory in which the potential at the surface drops across two layers, a compact inner and a diffuse outer layer. The distribution of ions in the diffuse layer depends of many factors (the concentration of electrolyte, the formal charge of the ions, the solvent, etc.), an important factor of this distribution is the potential at the boundary between the compact inner layer of ions and the diffuse outer layer of ions. The potential at this interface is often equated to the zeta (ζ) potential, which is the potential at the shear plane between the particle and the solvent under flow.

Table 3.4 presents zeta potential, mobility, and conductivity data in water. Non-functionalized PSiM has a negative zeta potential (-29.12 mV) consistent with the acidic nature of the surface hydroxyl groups, which upon partial functionalization with isocyanate groups provides PSiM-NCO with a less negative zeta potential (-16.54 mV). Hydrolysis of the isocyanate groups and La^{3+} coordination affords PSiM-NH₃⁺ and PSiM-NH₂La, respectively, which have positive zeta potentials (33.4 and 38.4 mV respectively). In agreement with their chemical nature, these materials undergo partial ionization in water and their conductivities are higher than observed for the non-functionalized PSiM. Ávila-Ortega et al.¹³⁹ made similar observations for amino-functionalized mesoporous silica nanoparticles (MSNs).

Table 3. 4. Zeta potential and results for the PSiM and its functionalized forms in water at 25°C.

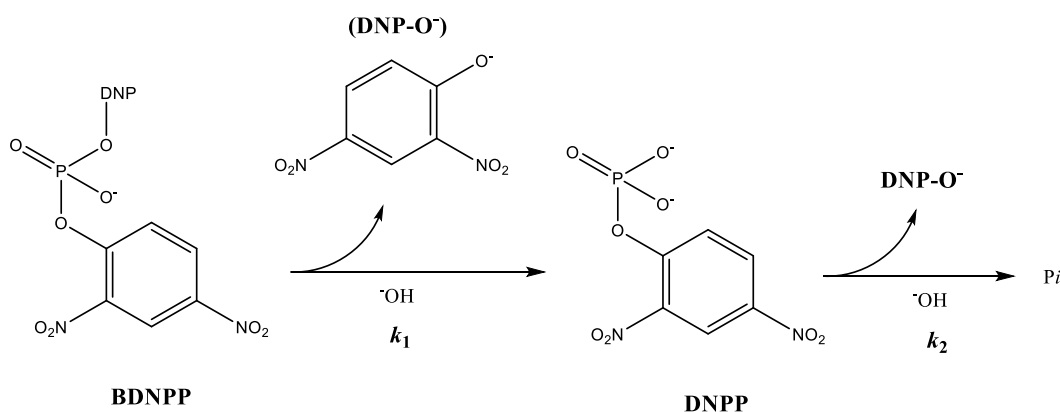
Sample	ZP	Mobility	Conductivity
	mV	$\mu\text{mcm/Vs}$	$\mu\text{S/cm}$
PSiM	-29.1 ± 1.8	-2.28 ± 0.14	9.72 ± 8.4
PSiM-NCO	-16.5 ± 2.4	-1.30 ± 0.19	5.61 ± 1.3
PSiM-NH ₃ ⁺	33.4 ± 2.5	2.62 ± 0.19	27.4 ± 1.5
PSiM-NH ₂ La	38.4 ± 5.0	3.11 ± 0.39	61.0 ± 1.6

3.2 Kinetic studies

The catalytic properties of the materials were evaluated for the BDNPP hydrolysis, which was followed by UV-Vis spectroscopy using a flow system. The reaction extent was monitored by 2,4-dinitrophenolate (DNP) formation, which absorbs at 360 nm and has a characteristic yellow color (Fig. 3.14). The reactions were started in a thermostated water-jacketed cell containing the catalyst that had its contents pumped through a silica filter and a quartz flow cuvette. In this technique, the Beer-Lambert law gives the absorption of monochromatic light for a single species of concentration c :

$$\log_{10}\left(\frac{I_0}{I_t}\right) = \epsilon cl = A \quad (3.1)$$

where, I_0 and I_t refer to the intensity of the respective incident and transmitted lights, l is the path length of the beam through the solution and ϵ is the molar absorptivity at that wavelength. Liquid contents were pumped through a silica filter and a quartz flow cuvette (refer to Figures 2.3 and 2.4). The BDNPP hydrolysis yielded one equivalent of DNP ($Abs_{360}=0.184 A U$)¹⁴⁰ and the phosphomonoester DNPP, which reacted to give an additional equivalent of DNP and inorganic phosphate (Pi) (Scheme 3.2). Figure 3.14 presents the data for the first 1500 min of BDNPP hydrolysis in the presence of PSiM-NH₂La.



Scheme 3. 2. Hydrolysis reaction of BDNPP, showing the representation used in the analysis.

Next, we present the results for the catalytic activity of PSiM and its functionalized form PSiM-NH₃⁺ and PSiM-NH₂La on the hydrolysis of BDNPP.

3.2.1 Evaluation of the catalytic activity of the PSiM hybrid material on the hydrolysis of BDNPP

Figure 3.14 presents successive spectra over time for the BDNPP hydrolysis in the presence of PSiM-NH₂La, showing the formation of DNP with maximum adsorption at 360 nm.

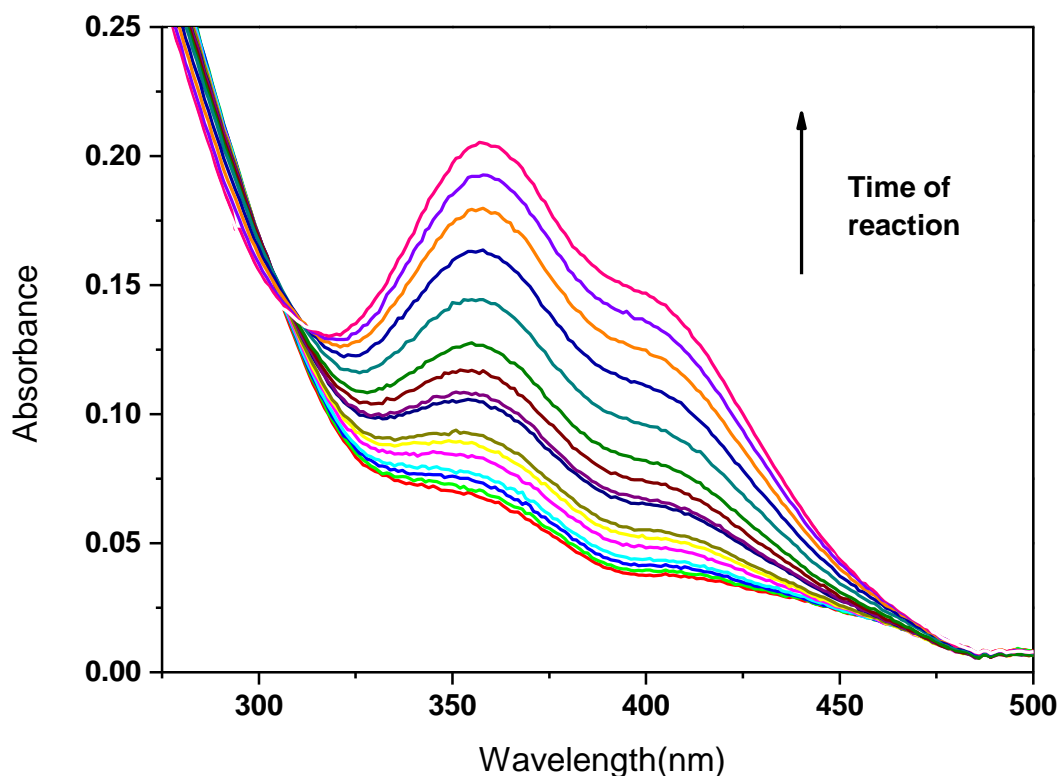


Figure 3. 14. Successive spectra as a function of the time for the kinetics of *bis*(2,4-dinitrophenyl) phosphate (BDNPP) cleavage in the presence of PSiM-NH₂La at pH 8.14 and 25 °C, using reactor 1 (Figure 2.3)

Figure 3.15 shows the kinetic profiles for the BDNPP hydrolysis (absorbance at 360 nm vs. time) obtained in the presence of PSiM and its functionalized forms. Clearly, PSiM and PSiM-NH₃⁺ have less activity for the hydrolysis of BDNPP at pH 8.14 compared to PSiM-NH₂La. The rate constants for cleavage of BDNPP in the presence of each material were treated by initial velocities according to the following equation:

$$k_{obs} = \frac{(\Delta Abs / \Delta t)}{2\epsilon b [BDNPP]} \quad (3.2)$$

where, ϵ is the molar absorptivity for DNP ($\epsilon = 14700 \text{ M}^{-1} \text{ cm}^{-1}$), b is the cuvette pathlength (1 cm), and $[BDNPP] = 12.5 \text{ } \mu\text{M}$. This method was preferred since considers only the BDNPP cleavage without other time-dependent effects due to species distribution on the catalyst

surface or structural changes in the catalyst. The observed rate constants for each of the materials studied are presented in the Table 3.5.

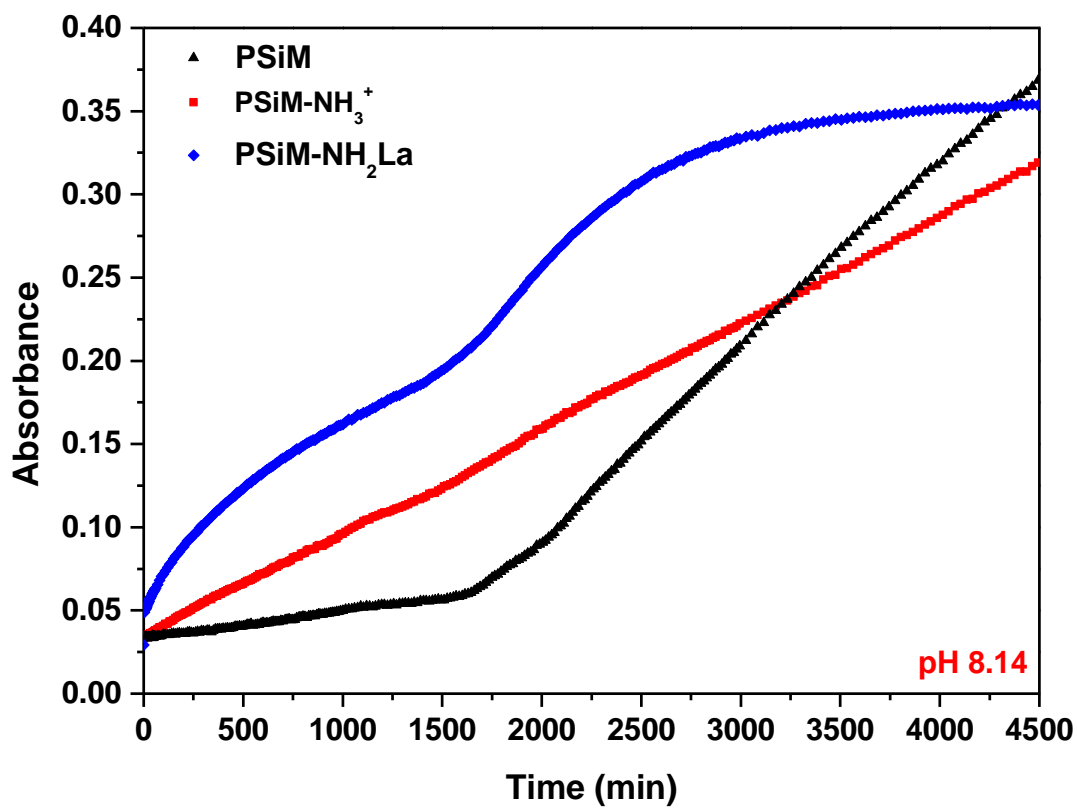


Figure 3. 15. Absorbance at 360nm as a function of time for the hydrolysis reaction of BDNPP in the presence of PSiM (black), PSiM-NH₃⁺ (red), and PSiM-NH₂La (blue) at pH 8.14 and 25 °C, using reactor 1 (Figure 2.3).

Table 3. 5. Kinetic parameters for cleavage of *bis*(2,4-dinitrophenyl) phosphate (BDNPP) in absence and presence of PSiM and its functionalized forms. The catalytic factor (*f*) is calculated in relation to the spontaneous hydrolysis.¹²⁵

Conditions (pH 8.14)	$10^4 k_{obs}$ (min ⁻¹)	<i>f</i>
Spontaneous hydrolysis	0.14	1.0
Non-functionalized PSiM	0.31	2.3
PSiM-NH ₃ ⁺	1.27	9.2
PSiM-NH ₂ La	5.30	38

Equation (3.2) is valid whenever the BDNPP concentration is the single change over time in a system where all the other variables are constant (e.g. nucleophile concentration and pH). The catalytic effect (*f*) denoted the ratio between the rate constants for the catalyzed and

uncatalyzed reactions. The half-life for the uncatalyzed hydrolysis is 35 days ($k_{\text{obs}}=1.38\times 10^{-5}$ min⁻¹) and falls to about 22 h ($k_{\text{obs}}=5.30\times 10^{-4}$ min⁻¹) in the presence of PSiM-NH₂La in pH 8.14 at 25 °C. This represents a rate enhancement of 38-fold, which is 4 and 17-fold higher than observed for PSiM-NH₃⁺ ($f = 9.2$) and PSiM ($f = 2.3$), respectively.

Supramolecular systems offer a multicooperative environments for catalysis^{141,142} and lanthanide coordination.¹⁴³ We attribute the small 2.3-fold catalytic effect for PSiM to entropic advantage (Circe effect).¹⁴⁴ The penalty for bringing reactants into close proximity in the uncatalyzed reaction is paid by their binding in the pores of PSiM, which restraint translational and rotational motions in the ground state. This effect is also observed for PSiM-NH₃⁺, where positively charged ammonium groups assist the recruitment of anionic reactants from the solution to the catalyst surface. This electrostatic effect reduces the repulsion between anionic groups and helps to stabilize the developing negatively charged transition-state. In PSiM-NH₂La, besides the entropic advantage due to substrate binding and electrostatic effects from positively charged amino groups, the La³⁺ coordinates nucleophilic hydroxide ions and the anionic BDNPP in close proximity for reacting (as mentioned before Chapter 1.2).

3.2.2 Evaluation of the reusability of PSiM-NH₂La on the hydrolysis of BDNPP

To assess the reuse capacity and stability of PSiM-NH₂La, reuses studies were made as described on chapter 2.3.1 (hydrated method) using the reactor 1 (Figure 2.3). Figure 3.16 shows the kinetic profiles for each reuse of the catalyst. The activity boosts after the first use is due to aspects that will be discussed in detail in the next chapter. This increase in activity remains even after the sixth cycle of use (Figure 3.17), although after each use the catalytic activity undergoes a slight decrease. According to TXRF analyses, the material preserved the same metal concentration after the first use, and no detectable amount of La³⁺ was found in the reaction solution after filtering off the catalyst. Decrease in the catalytic activity after reuse is probably a consequence of catalyst poisoning by phosphate. Such behavior is common for metal-containing catalysts used in the hydrolysis or cleavage of phosphoesters,^{145,146,147} which involves metal poisoning caused by coordination of the inorganic phosphate released as a reaction product. After the first use of PSiM-NH₂La, the following 5 reuses occurs at faster rates with formation of two DNP equivalents.

Table 3. 6. Kinetic parameters for cleavage of *bis*(2,4-dinitrophenyl) phosphate (BDNPP) in the presence of PSiM-NH₂La at pH 8.14 and 25 °C. The catalytic factor (*f*) is calculated in relation to the spontaneous hydrolysis (table 3.5).

Conditions	$10^4 k_{\text{obs}}$ (min ⁻¹)	<i>f</i>
(PSiM-NH ₂ La 50mg, reactor 1, and pH 8.14)		
1 st use	5.30	38
1 st reuse	84.5	612
2 nd reuse	54.5	395
3 rd reuse	54.0	391
4 th reuse	38.1	276
5 th reuse	29.6	215

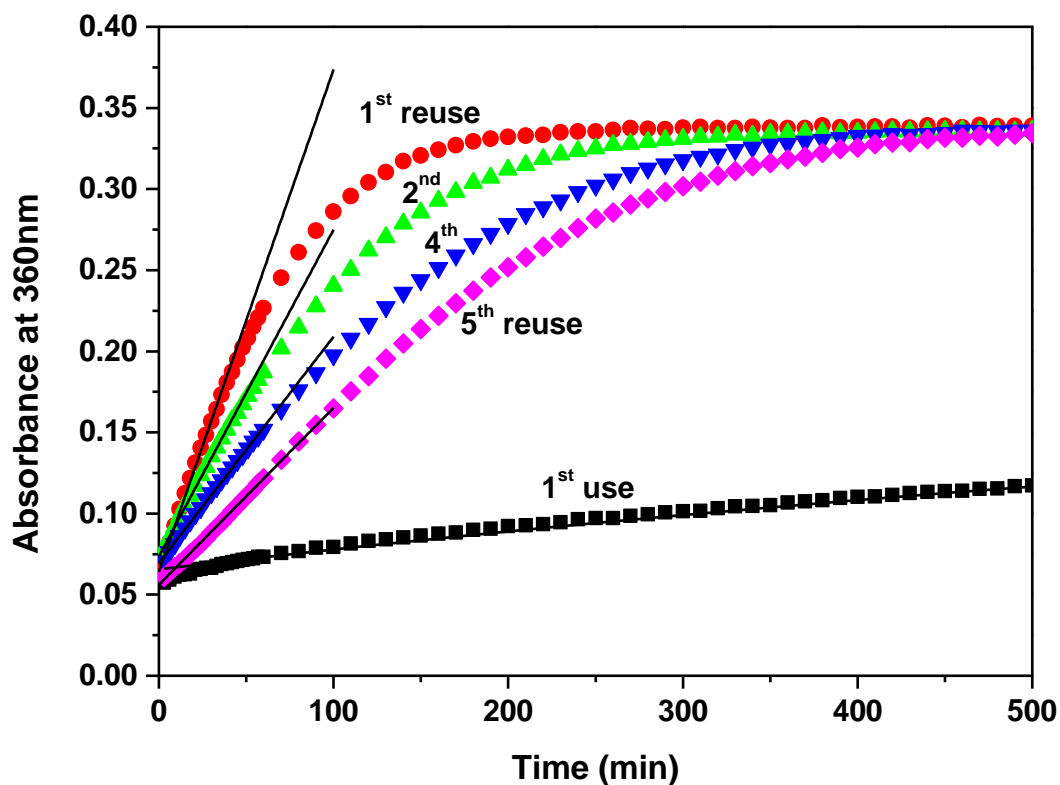


Figure 3. 16. Absorbance at 360nm as a function of time for hydrolysis of BDNPP in the presence of PSiM-NH₂La at pH 8.14 and 25 °C, using reactor 1(Figure 2.3).

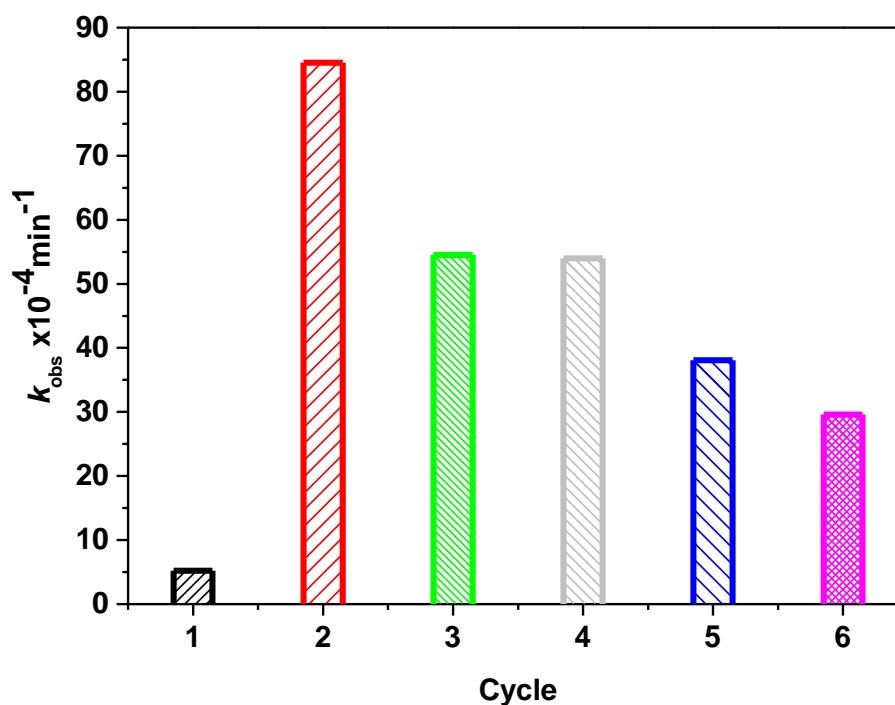


Figure 3. 17. Bar diagram representing the rate constants for the hydrolysis of BDNPP in the presence of PSiM-NH₂La at pH 8.14 and 25°C (table 3.6) obtained for each use and reuse (cycle).

The catalytic activity (f) after the first use and second reuse are 38 and 612-fold above the spontaneous BDNPP hydrolysis under the same conditions. After 6 reuses the catalyst exhibits an activity only 3-fold lower than the second reuse, though 5.6-fold above the first use.

3.2.3 pH-rate profile for the catalytic activity of PSiM-NH₂La on the hydrolysis of BDNPP

To evaluate the influence of pH on the catalytic properties of PSiM-NH₂La to hydrolyze BDNPP, the catalytic activity was evaluated at different pHs (Table 3.7). The Figure 3.18 shows the increase in absorbance at 360 nm as function of time for each pH.

Fresh PSiM-NH₂La samples were used for the kinetic studies from pH 7 to 11 (Figure 3.19). A negative slope of about 0.3 is found in the pH-dependent region and a plateau is achieved below pH 8. This indicates that gradual environment-dependent amino group protonation occurs at lower pH, providing faster reactions. The protonated catalyst activates the initial state by substrate and nucleophile recruitment to the catalyst surface, where transition state stabilization provides a fast substrate cleavage. A possible mechanism underlining these observations is depicted in Scheme 3.3.

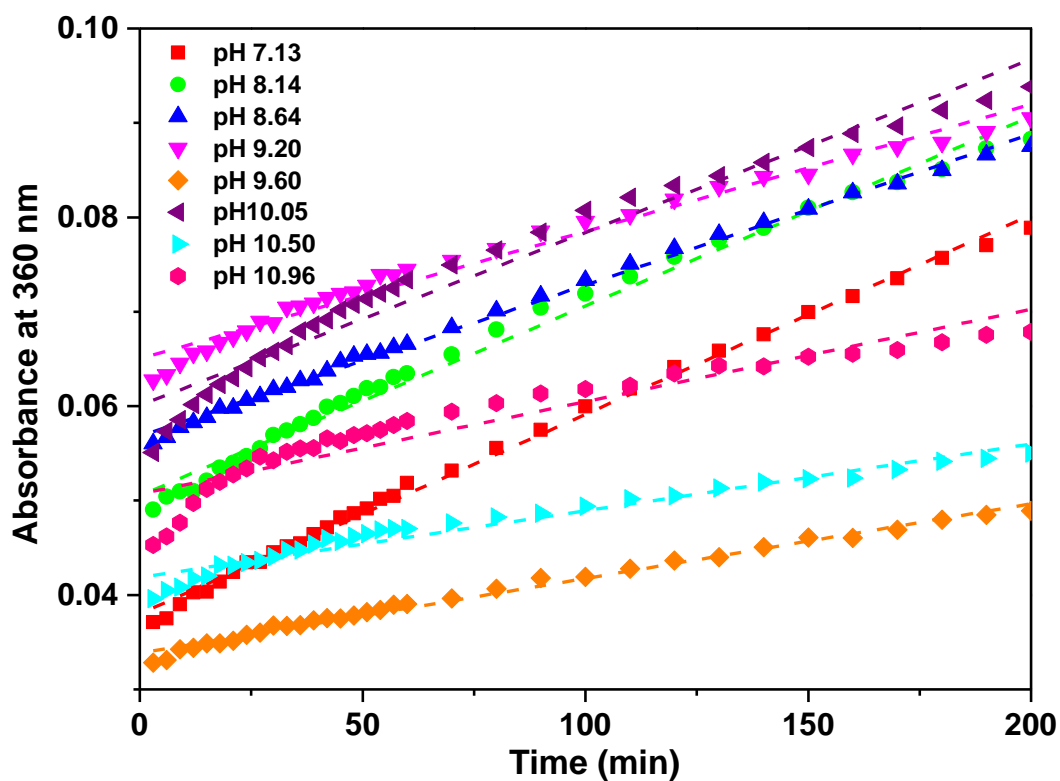


Figure 3. 18. Absorbance at 360nm as a function of time for the hydrolysis of BDNPP in the presence of PSiM-NH₂La at different pHs, using reactor 1(Figure 2.3).

Table 3. 7. Kinetic parameters for cleavage of *bis*-(2,4-dinitrophenyl) phosphate (BDNPP) in the presence of PSiM-NH₂La at different pH and 25 °C.

Conditions (PSiM-NH ₂ La 50 mg, reactor 1)	$10^4 k_{\text{obs}}$ (min ⁻¹)
pH 7.13	5.35
pH 8.14	5.30
pH 8.64	3.93
pH 9.20	3.46
pH 9.60	1.69
pH 10.05	1.87
pH 10.50	1.04
pH 10.96	1.10

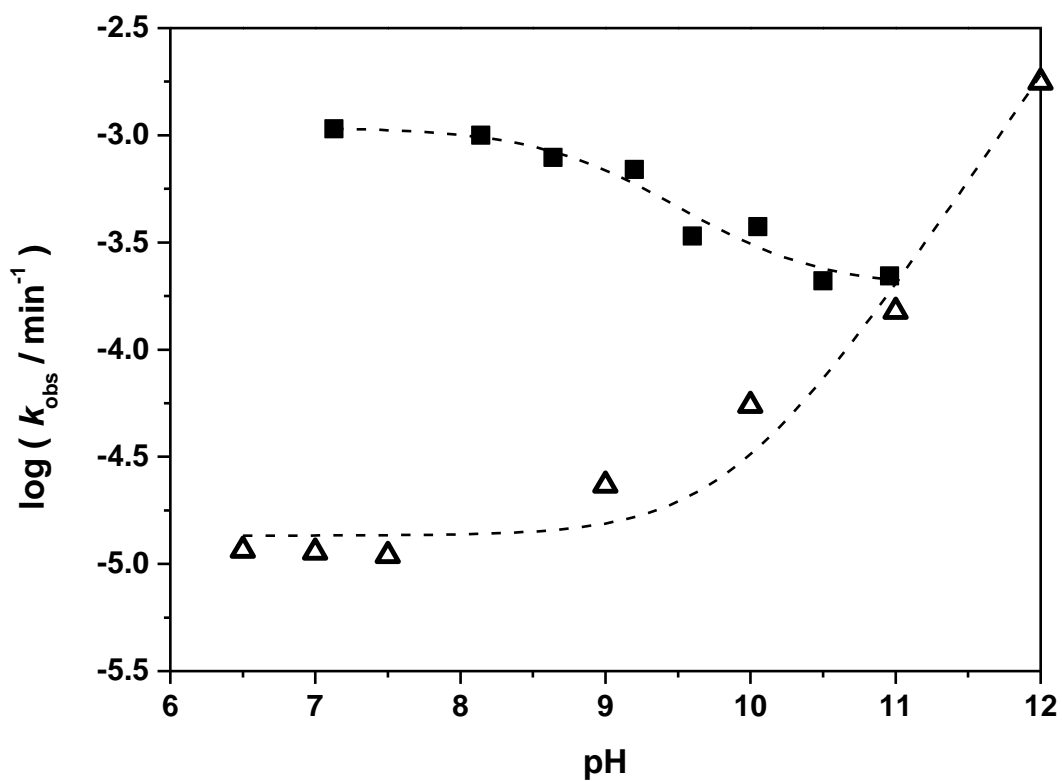
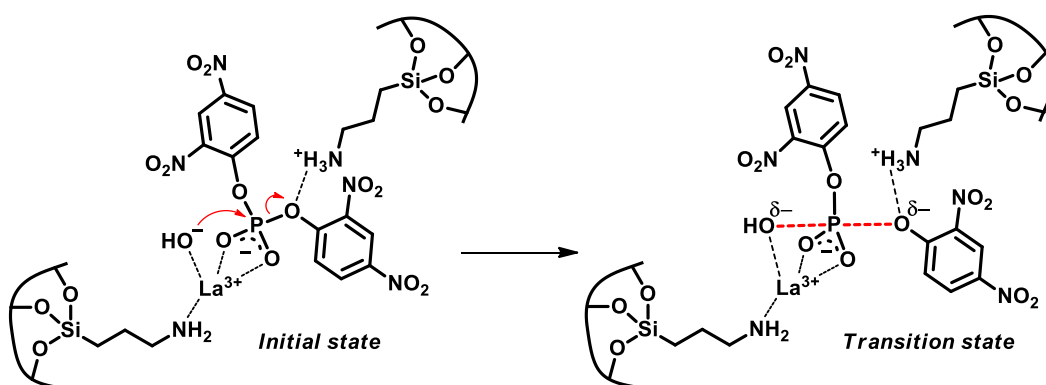


Figure 3. 19. pH-Rate profile for *bis*-(2,4-dinitrophenyl) phosphate (BDNPP) cleavage in absence (Δ) and presence (\blacksquare) of PSiM-NH₂La at 25 °C. Kinetic data in absence of the catalyst were taken from Farber and Bunton.¹²⁵



Scheme 3. 3. Proposed mechanism for *bis*-(2,4-dinitrophenyl) phosphate (BDNPP) cleavage by PSiM-NH₂La.

3.3. Conclusion

In summary a porous silica material with high surface area ($S_{\text{BET}}=432\text{m}^2\text{ g}^{-1}$) functionalized with $\text{NH}_2/\text{NH}_3^+$ groups and coordinated to lanthanum ions in the respective proportion of 13 to 1 was synthesized and used as catalyst for the hydrolysis of BDNPP. As such, the catalyst surface was positively charged and attracted the anionic bis(2,4-dinitrophenyl)phosphate. The hydrolysis in the first use of the catalyst at pH 8.14 was about 38-fold faster than in its absence. In contrast to its first use, catalysis was about 15 times faster in the first reuse and about 6 times faster after the 5th reuse. Lanthanum ion activated metal bound hydroxide ions, which were properly oriented for nucleophilic attack on the electrophilic substrate, and the amino groups partook in transition state stabilization by electrostatic interactions.

4 STRUCTURAL CHANGES IN THE PSiM STRUCTURE AND ITS ROLE TO CATALYSTS.

Catalytic activity, selectivity and stability depends on size, shape and structure of the catalyst particles.^{148,149} While ex-situ characterization offers significant understanding into the catalyst structure and composition, these observations may not provide information about changes in the catalyst structure and properties in its operating state. Such observations are fundamental to describe the catalyst structure-property relationships and, therefore, is essential to obtain structural information about catalysts under reaction conditions. In our case, as discussed in the previous chapter, hydrolysis of BDNPP in the presence of PSiM and PSiM-NH₂La (scheme 3.2) was used to probe changes in the activity, functionality, and stability of the catalysts. A key observation for this part of the work is the increase of the catalytic activity after an induction period (Figure 4.1). This chapter discusses what type of changes occur in the PSiM structure and how these changes affect the catalytic properties of the material. To probe the structural changes over time, samples of the catalyst were taken and analyzed by different techniques to find a relationship between physical and chemical changes on the surface and structure of PSiM and PSiM-NH₂La with the catalytic activity on the hydrolysis of BDNPP.

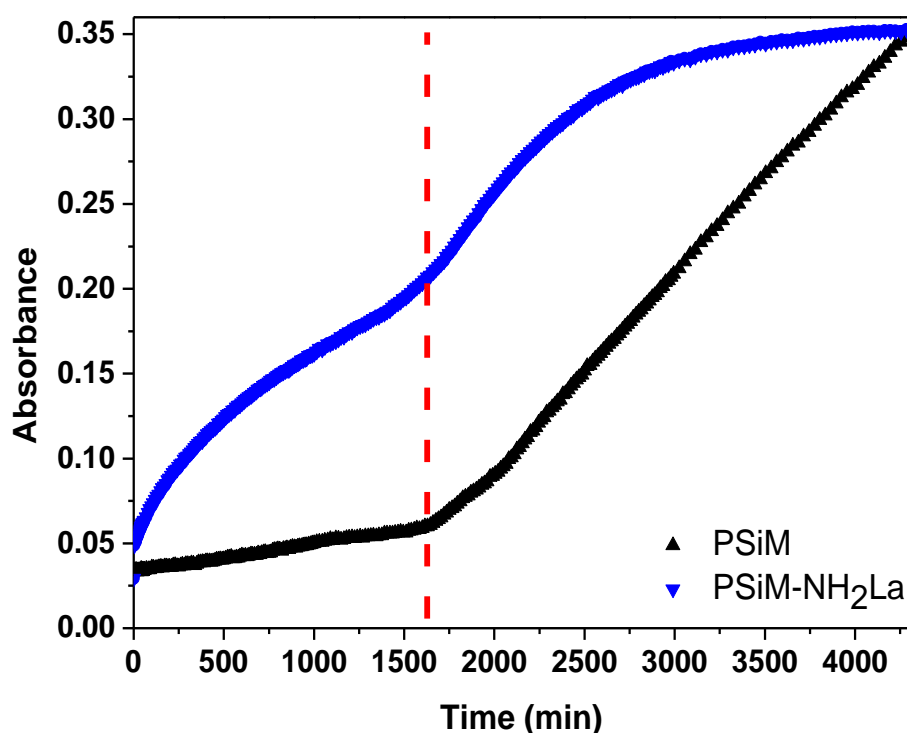


Figure 4. 1. Absorbance at 360nm as a function of time for the hydrolysis reaction of BDNPP in the presence of PSiM (black), and PSiM-NH₂La (blue) at pH 8.14 and 25 °C, using reactor 1(Figure 2.3). The two different stages on the reaction rate are divided by the red dashed line \approx 1500 min.

4.1 Structural characterization

Insights about the structural changes associated with the increase on the catalytic activity were provided by different analytical techniques.

4.1.1 X-ray Power Diffraction (XRD) in function of time

Figure 4.2 presents the XRD analysis for the PSiM samples recovered at different hydration times and when used as catalyst on the hydrolysis of BDNPP (8000min) at pH 8.0. To determine if the initial structure is maintained or lost during the reaction, all samples up to 8000 min presented a distinguishable Bragg peak at 3.1° related to (1 0 0) Miller reflection for the hexagonal P6 space array of PSiM particles.¹⁰ However, a slight loss in the intensity of the (1 0 0) peak is observed, together with the disappearance of the (1 1 0) and (2 0 0) peaks observed in the base material. Assuming that the samples were prepared in the same manner, these observations can be related to the effect of the physically adsorbed water on the XRD intensities¹⁵⁰ and/or the pore structure changes during rehydration¹¹⁸ as discussed by others. Marler *et al.*¹⁵⁰ found that the presence of organic sorbates or water have a major influence on the XRD intensities of MCM-41 materials which, however, can be fully recovered upon desorption of the species by heat treatment.

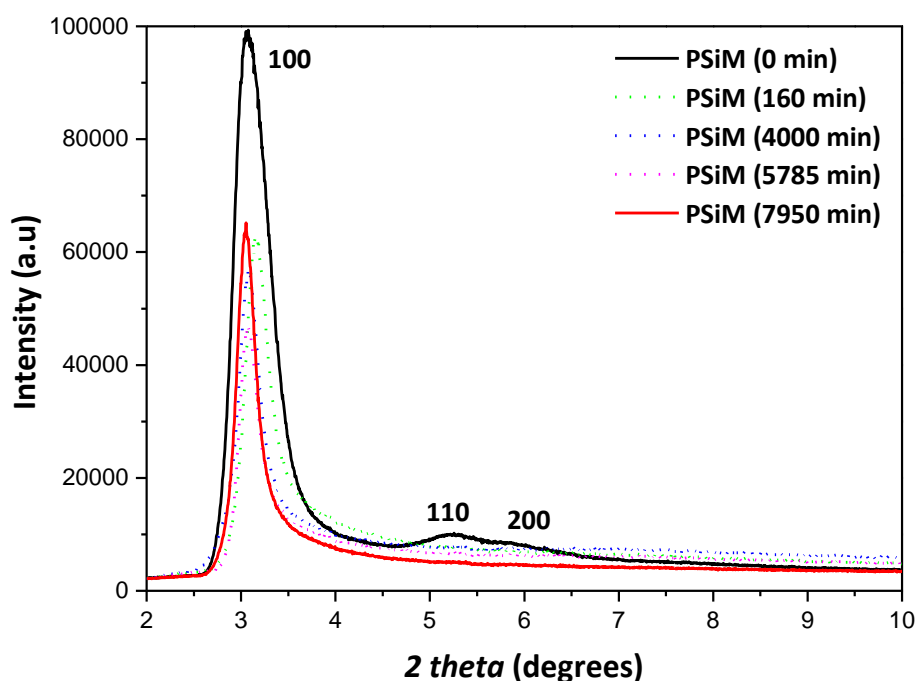


Figure 4. 2. Powder X-ray diffraction pattern of the recover at different hydration times and used as catalyst on the hydrolysis of BDNPP(8000 min).

This behavior is not only observed for the base material, the XRD pattern for PSiM-NH₂La after 8000 min of BDNPP hydrolysis presented the same behavior (Figure 4.3). The peak at 3.1° related to (1 0 0) Miller reflection is also conserved after 8000 min of reaction with a slight intensity lost. As before (section 3.1.9) the d_{100} and a_0 were calculated and reported on table 4.1. The d_{100} and a_0 values are constant during all reaction time, showing that no major structural changes occur on the material.

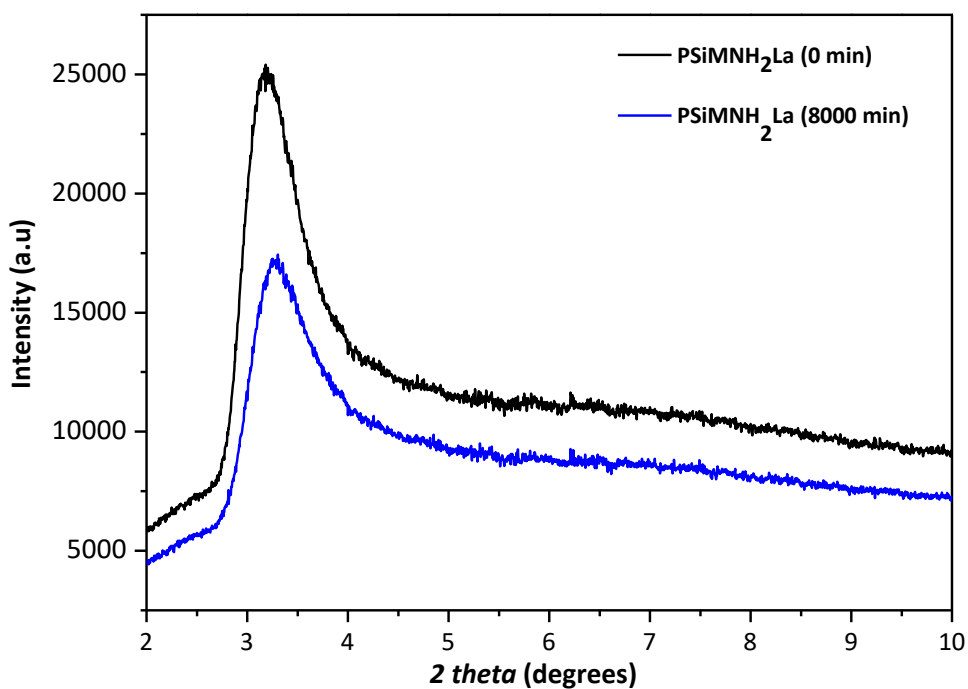


Figure 4. 3. XRD for PSiM-NH₂La before and after its use in the hydrolysis of BDNPP.

Table 4. 1. Structural parameters determined from XRD data (Figure 4.2 and Figure 4.3).

Sample	2 θ	d_{100} (nm)	a_0 (nm)
PSiM (0 min)	3.07	2.88	3.32
PSiM (160 min)	3.17	2.78	3.21
PSiM (4000 min)	3.07	2.88	3.32
PSiM (5785 min)	3.07	2.88	3.32
PSiM (7950 min)	3.05	2.90	3.35
PSiM-NH ₂ La (0 min)	3.19	2.78	3.21
PSiM-NH ₂ La (8000 min)	3.25	2.72	3.14

4.1.2 Transmission electron microscopy

The TEM images for PSiM and PSiM-NH₂La obtained at different reaction times confirm that the original hexagonal ordering is maintained after its use (Figure 4.4). The TEM images for the

recovered materials after 8000 min of reaction (hydrolysis of BDNPP), figures 4.4d (PSiM) and 4.4f (PSiM-NH₂La), display the same structural pattern of the base material. Although, this observation is not conclusive about the occurrence of surface changes on PSiM or PSiM-NH₂La structures. Pham et al.¹¹³ found that TEM and SEM micrographs, and the XRD pattern of a mesoporous silica material that underwent physical changes were similar to those of the original.

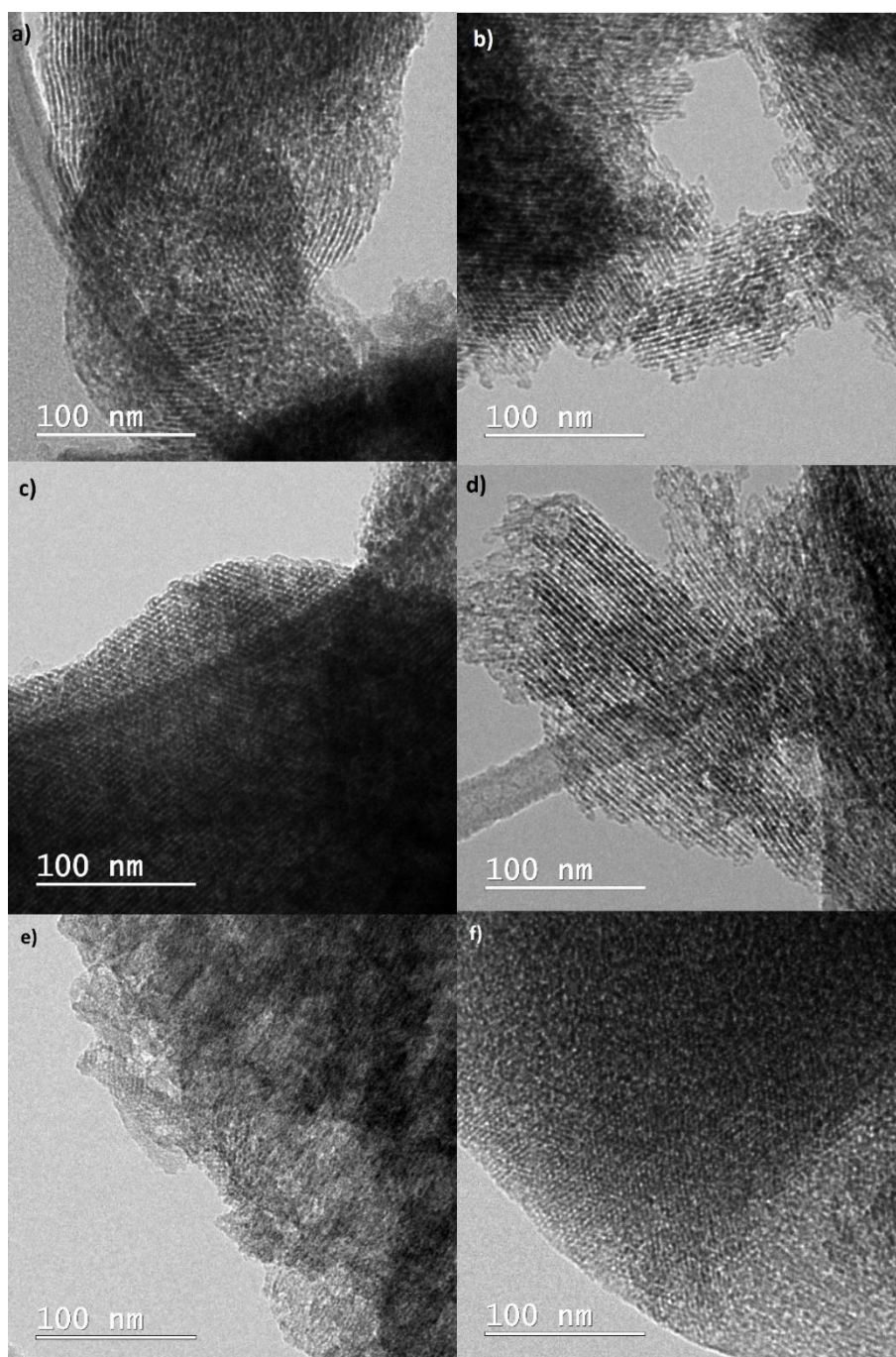


Figure 4. 4. Transmission electron microscopy (TEM) at different reaction times a) PSiM 160 min, b) PSiM 1230 min, c) PSiM 2560 min, d) PSiM 8000 min, e) PSiM-NH₂La 0 min and f) PSiM-NH₂La 8000 min.

4.1.3 Determination of the surface area by adsorption of N₂ using the BET method

The N₂ adsorption-desorption isotherms for PSiM and PSiM-NH₂La (Figure 4.5) before and after its use present an isotherm type IV for the PSiM as-synthesized, for the others a type II b with a hysteresis loop H4 is observed. The BET surface area (Table 4.2) decrease significantly after use, suggesting that structural changes occur in the sample which affect the microstructural arrangement in PSiM and PSiM-NH₂La. The BET surface area decreases by 51 % for PSiM and 28 % for PSiM-NH₂La, confirming that the incorporation of organic groups alters surface reactivity and protects the surface from chemical attack. Functionalization increases hydrophobization of the surface by silylation, modifying the bulk properties of the materials while at the same time preclude water attack stabilizing the materials in relation to hydrolysis.⁸⁰ The micropore area of the recover materials (Table 4.2) decrease in concordance with the total surface area, a remarkable decrease for the PSiM is found with a total collapse of the micropores. Although, as previously observed by TEM, the morphology of the materials is not significantly changed (D_p value).

Table 4. 2. Surface area, Micropore area and D_p for PSiM and PSiM-NH₂La at different reaction times as measured from the adsorption-desorption of N₂ at 77 K.

	PSiM (0 min)	PSiM (5790 min)	PSiM-NH ₂ La (0 min)	PSiM-NH ₂ La (8000 min)
Surface area (m ² g ⁻¹)	991	484	432	312
Micropore area (t-Plot method m ² g ⁻¹)	99	0	63	44
D_p (nm)	3.6	3.6	3.6	3.6

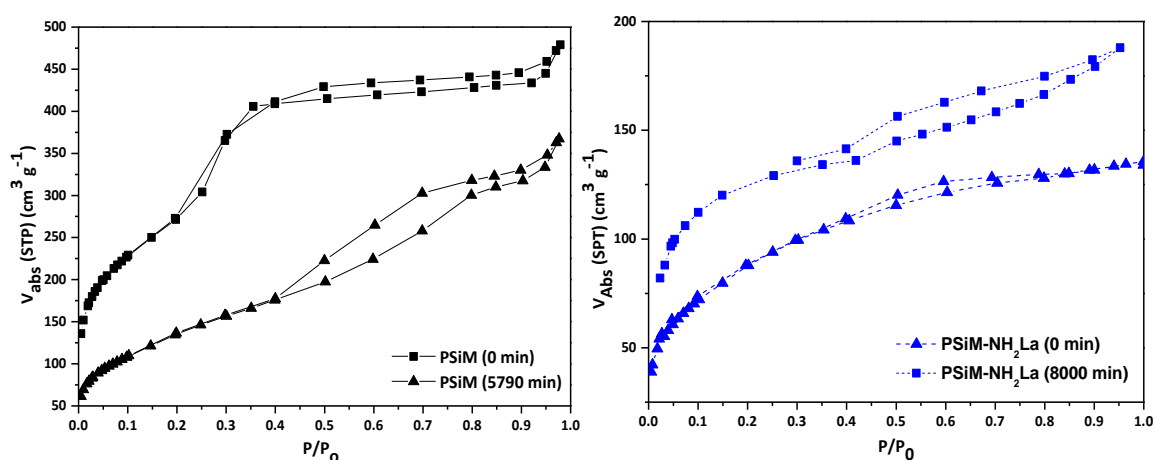
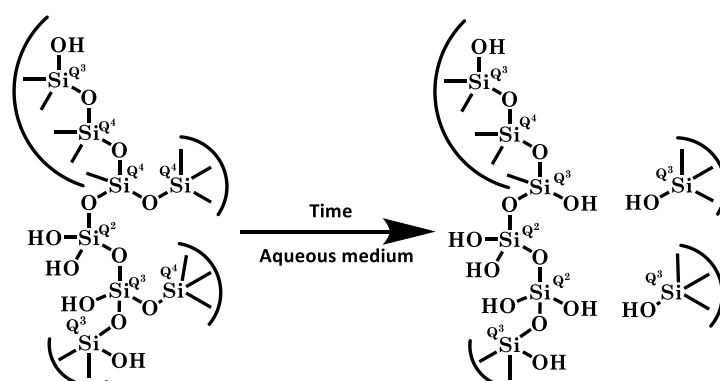


Figure 4. 5. Nitrogen adsorption-desorption isotherms for PSiM (black) and PSiM-NH₂La (blue) as-synthesized and recovered after the hydrolysis of BDNPP at pH 8.0 and 25°C.

4.1.4 Solid-State Nuclear Magnetic Resonance (NMR)

The chemical and physical information that is currently available for the majority of silicon structures has been achieved mainly through two different approaches:¹⁵¹ first, the study of ultra-low surface-area materials ($\approx 10^{-4} \text{ m}^2\text{g}^{-1}$), using ultra-high vacuum (UHV) instrumentation and techniques of “surface science”, that is, infrared (IR) spectroscopy,¹⁵² scanning tunneling microscopy (STM),¹⁵³ atomic force microscopy (ATM),¹⁵⁴ transmission electron microscopy (TEM),¹⁵⁵ high-resolution electron energy loss spectroscopy (HREELS)¹⁵⁶ or X-ray photoelectron spectroscopy (XPS),¹⁵⁵ etc.; and, second, the study of high-surface-area materials ($100\text{-}1200 \text{ m}^2\text{g}^{-1}$) by solid-state nuclear magnetic resonance (NMR).^{151,157,117,158} We used the second approach to evaluate the chemical composition of the catalyst upon hydration (Figure 4.6). This data reveals that hydration of PSiM affects not only the physical characteristics of the material but also the chemical nature of the silicon atoms that form the material network.

Three resonance peaks at -109 , -101 , and -91 ppm were observed for PSiM, which were assigned to the silicon sites of $\text{Si}(\text{OSi})_4$ (Q^4), $\text{HO-Si}(\text{OSi})_3$ (Q^3), and $(\text{HO})_2\text{Si}(\text{OSi})_2$ (Q^2) (Scheme 4.1), respectively. The Q^3 sites are SiOH groups (i.e., free and hydrogen-bonded), and the Q^2 sites correspond to geminal silanols. Varache et al.¹¹⁸ reported that the hydroxylation relates to Q^4/Q^3 ratio. PSiM as-synthesized has a $\text{Q}^4/\text{Q}^3 = 0.61$ and the PSiM aged in an aqueous solution has a $\text{Q}^4/\text{Q}^3 = 0.43$ (Figure 4.6). This change in ratio is explained due to the relative intensity of the Q^4 silicons decreases in profit for Q^3 silicons because the Q^4 silicon sites are hydroxylated during the induction period as shown in figure 4.1. This behavior has been observed for Si NPs that become less branched upon hydration.^{159,83} The structural changes associated with the induction time in the use of PSiM produce more active active surfaces for catalysis of BDNPP hydrolysis.



Scheme 4. 1. Hydroxylation processes during which new silanol groups are generated.

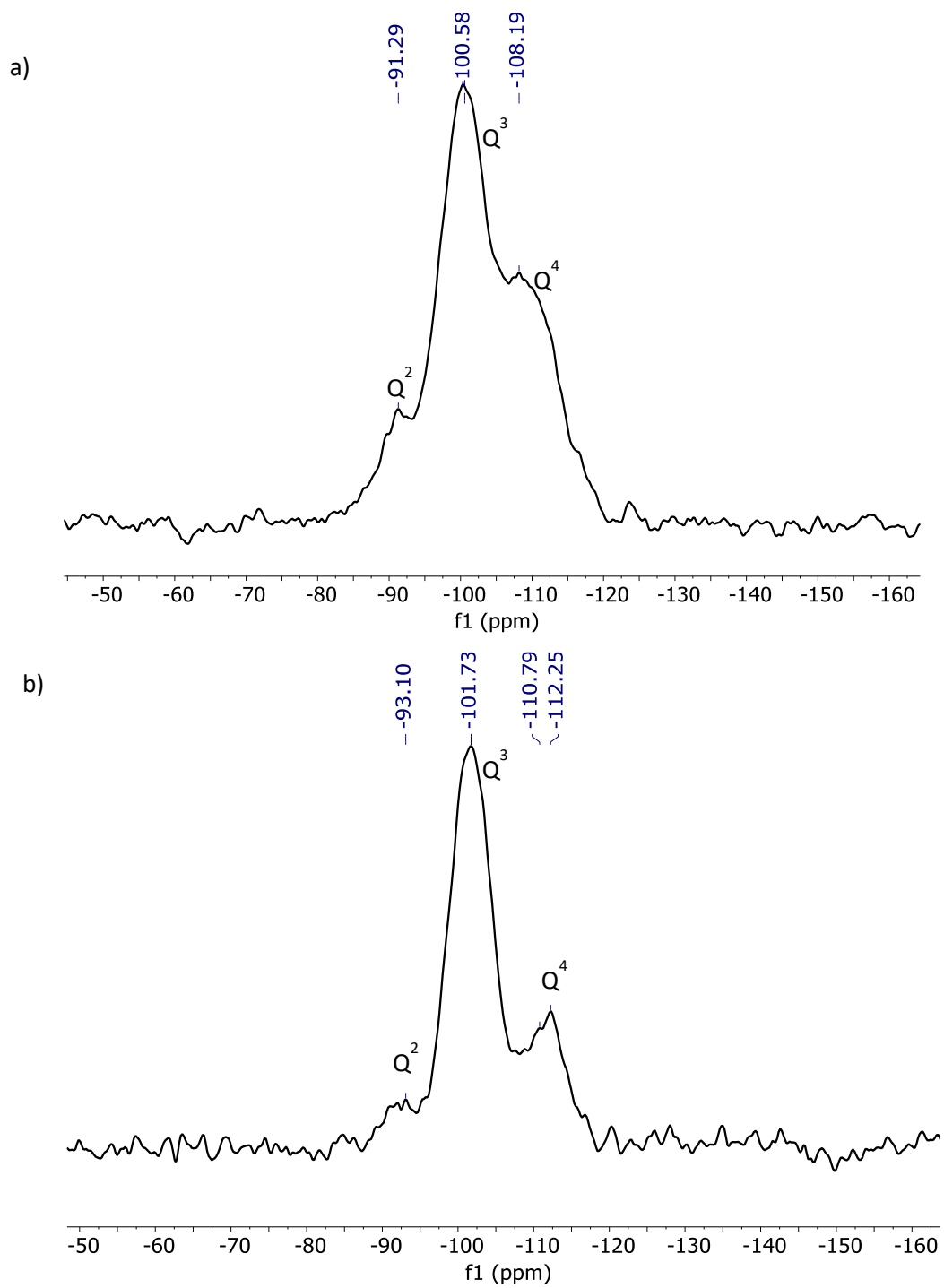


Figure 4. 6. Solid-state MAS ²⁹Si-NMR spectra for PSiM before (a) and after (b) use as catalyst on the hydrolysis of BDNPP at pH 8.0 and 25°C.

4.1.5 Zeta potential

Figure 4.7 shows the values of the zeta potential measured as function of time. PSiM and PSiM-NH₂La were incubated in the buffer solution (HEPES 0.1 molL⁻¹, pH 8) and the zeta potential was measured at different time intervals. The potential of both materials, base and modified, increase over time, although at different rates. The zeta potential of PSiM increases faster than observed for PSiM-NH₂La and stabilizes after five hours of incubation. As mentioned before, the ZP is determined at the boundary between the compact inner layer of ions and the diffuse outer layer. This means that the ZP is related with the mobility of the ions at the surface of each material.¹⁶⁰

Therefore, PSiM-NH₂La requires more time to get to an equilibrium, because mobility of the ions is slow due to interactions with the amino group and lanthanide ions. Therefore, the amino group and the lanthanum ion act as stabilizers and maintain the initial state for a longer time.

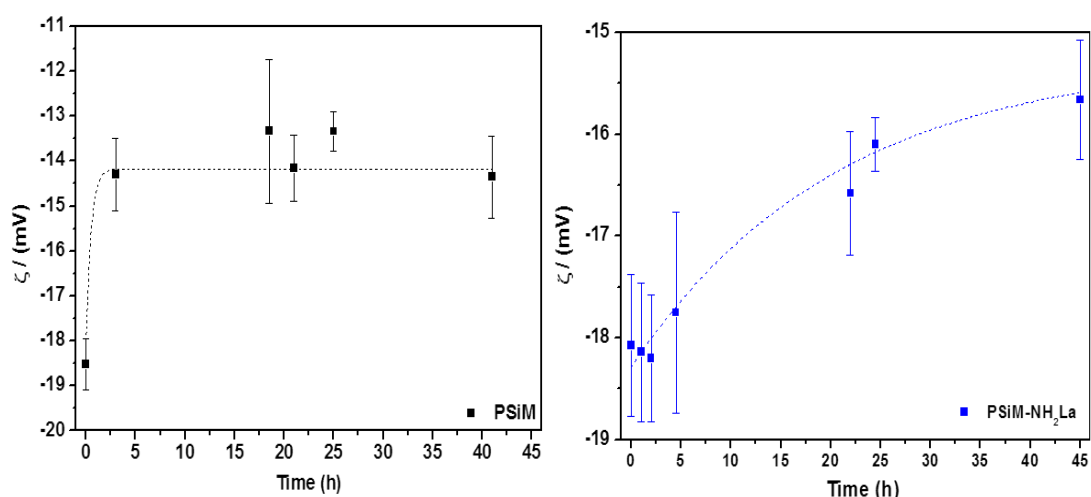


Figure 4. 7. Zeta potential as function of time for the PSiM (a) and the PSiM-NH₂La (b) at pH 8.0 and 25°C

4.2 Kinetic studies

On chapter three was shown that the reuse of PSiM-NH₂La after the induction period present higher activity for BDNPP hydrolysis than in the first use. We propose that the structural changes described above modify the nature of the active-sites. The concept of “active-sites” in heterogeneous catalysis is attributed to Taylor,¹⁶¹ who proposed that the concentration of sites where rate-determining catalytic reaction steps occur is much smaller than the total concentration of available surface sites. A relationship of the catalyst *surface structure* with rates

of different reactions indicated that the nature of the active-site where bond breaking occurs, for example, diverge for different chemical bonds. In our cases the catalytic sites are related to the breakdown of the phosphodiester bond, which is favored by the increase of the silanol population involved in the stabilization of a charged transition-state.

Below we detail our efforts to evaluate the impact of the hydration conditions on the development of PSiM active site better suited for the hydrolysis of BDNPP.

4.2.1 Use and reuse of PSiM as catalyst on the hydrolysis of BDNPP

PSiM was reused under the same conditions of PSiM-NH₂La to determine if the boost on the catalytic activity occurs only for PSiM-NH₂La or is a characteristic of PSiM materials. Figure 4.8 presents the kinetic profiles obtained for the use and reuse of PSiM as catalyst on the hydrolysis of BDNPP at pH 8.0 and 25°C. An induction period represented by a drastic change in the slope of the curve is observed on the first use at 1500 min, when the DNP⁻ formation becomes faster. The same boost on the catalytic activity found for PSiM-NH₂La is observed for PSiM, which implies that this behavior is general for mesoporous materials.

In table 4.3 are reported k_{obs} determined by the initial velocities for the BDNPP hydrolysis in the first use and reuse. These values reveal that the structural changes are fundamental to the catalytic activity. However, it is important to observe that the catalytic activity for the hydrated material is not as high as shown for PSiM-NH₂La under the same conditions, which confirm the importance of the lanthanide ion for catalysis.

Table 4. 3. Kinetic parameters for cleavage of *bis*(2,4-dinitrophenyl) phosphate (BDNPP) in the presence of PSiM at pH 8.0 and 25 °C. The catalytic factor (*f*) is calculated in relation to the spontaneous hydrolysis (table 3.5).

Conditions	$10^4 k_{obs}$ (min ⁻¹)	<i>f</i>
PSiM, pH 8.0 – 1 st use	0.42	3.03
PSiM, pH 8.0 – 2 nd use	36.2	262

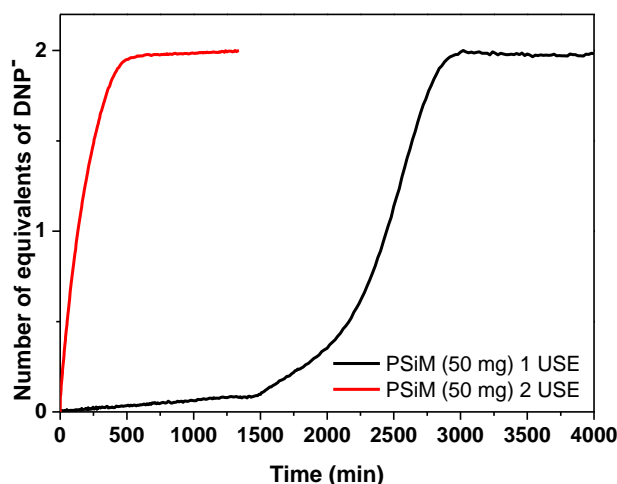


Figure 4. 8. Absorbance at 360nm as a function of time for the hydrolysis of BDNPP in the presence of PSiM at pH 8.0 and 25 °C, first and second uses using reactor 1 (Figure 2.3).

4.2.2 Activation of PSiM prior its use on the hydrolysis of BDNPP

In order to evaluate the influence of the substrate in the induction period of PSiM, two different kinetic experiments were carried out at pH 8.0 (HEPES 0.1 mol L⁻¹) and 25°C. A previous study reported that interactions between the substrate and silica based catalyst can induce the formation of better active site.¹⁶² In the first experiment, PSiM was let to hydrate with 20 mL of buffer solution in a 50 mL conical tube. On the second, to evaluate the influence of phosphate ion (product of complete BDNPP hydrolysis), PSiM was let to hydrate with 20 mL of buffer solution in the presence of 2.0 mmolL⁻¹ phosphate ion. Figure 4.9 presents the kinetic profiles for each of these experiments and the rate constants are reported in Table 4.4.

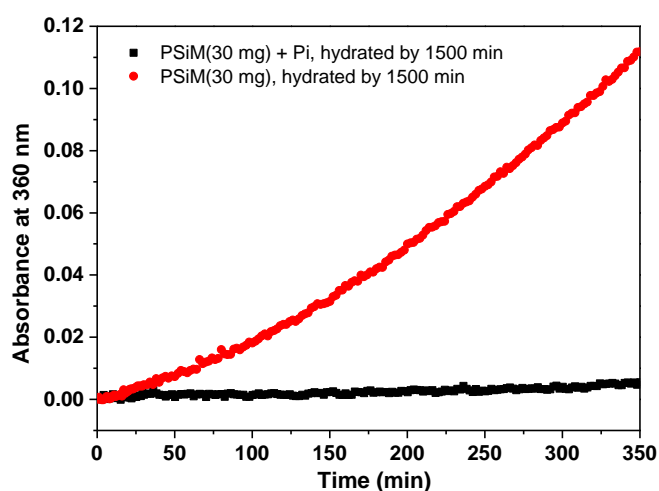


Figure 4. 9. Kinetic profiles for the hydrolysis of BDNPP [12.5 mM] using a previous hydrated PSiM (30mg, on a 20 mL buffer solution by 1500 min) in the absence and presence of 2.0 mmolL⁻¹ phosphate ion (Pi) at pH 8.0 and 25°C using reactor 2 (Figure 2.4).

Table 4. 4. Kinetic parameters for cleavage of *bis*(2,4-dinitrophenyl) phosphate (BDNPP) in the presence of hydrated PSiM in absence and presence of 2.0 mmolL⁻¹ phosphate ion at pH 8.0 and 25 °C. The catalytic factor (*f*) is calculated in relation to the spontaneous hydrolysis (table 3.5).

Conditions	10 ⁴ <i>k</i> _{obs} (min ⁻¹)	<i>f</i>
PSiM, hydrated for 1500 min, pH 8.0	6.5	47
PSiM, hydrated for 1500 min, pH 8.0 in the presence of phosphate ion	0.201	1.45

As these kinetic data above suggest, the presence of phosphate ion or the hydration under steady-state conditions does not respond for the catalytic activity, suggesting that another factor may influence the activation of the surface of the PSiM.

4.2.3 Activation of the PSiM on the flow system

The effect of pressure in gas state is well known, increasing the pressure on a reaction involving reacting gases increases the rate of reaction. On the other hand, changing the pressure on a reaction which involves only solids or liquids has a small effect on the rate. Weale *et al.*¹⁶³ describes the role of pressure on reactions at liquid state, according to him: “At hydrostatic pressures of several thousand atmospheres the rates of many liquid-phase reactions are considerably increased.” To validate the influence of the flow and the pressure in our catalytic system, 10 mg of catalyst were placed on the flow system and let to hydrate for 1500 min. Then, the substrate was added to initiate the BDNPP hydrolysis. Figure 4.10 shows the kinetic profile for the BDNPP hydrolysis reaction (absorbance at 360 nm vs. time) for this reaction. Clearly, hydrated PSiM presents a kinetic profile in agreement with the reuse on hydrated conditions (see figures 3.16 and 4.8). This observation suggests that a more active surface was created upon hydration, which does not depend on BDNPP hydrolysis itself and is facilitated under high pressure achieved in the PSiM pores.

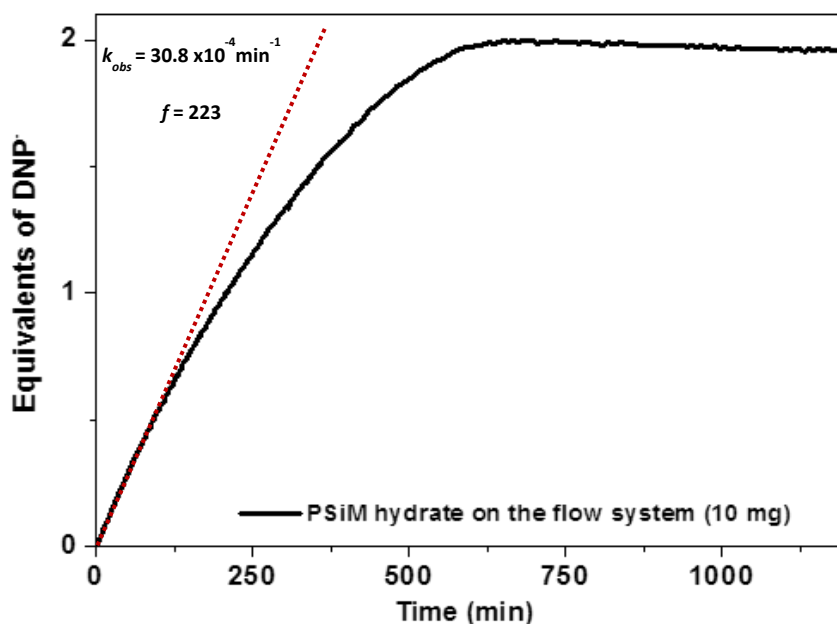


Figure 4. 10. Kinetic profile for the hydrolysis of BDNPP using PSiM hydrated on flow reactor 2(Figure 2.4) at pH 8.0 and 25°C.

Several factors can affect the rate of chemical reactions, according to Avnir et al.¹⁶⁴ chemical reactions respond to three major parameters: the nature of the chemical bond which is formed (or/and broken) in the reacting molecules; the stereochemical conditions which dictate this molecular change; and the energy profile of the reaction. Avnir¹⁶⁴ also describe that when studying heterogeneous systems, a new factor has to be considered: the structure and the geometry of the environment in which the reaction takes place. This factor is as significant as the three others to the extent that can behest whether a reaction will take place. Despite to this, the quantitative treatment of this aspect and its relation to the other reaction parameters is poorly understood. The main reason for this struggle has been the nature of the structures involved in the majority of materials and because their surfaces show extremely complex geometries and sometimes, as in our case, the surface is not static but dynamic, complicating even more the analysis. In general, the geometry problem has two important consequences: first, on the basic level, it is quite difficult to study geometry-efficiency relationships, both phenomenologically and in a predictive fashion. And second, on the applied side, quality control has usually focused on parameters such as particle size, surface area and pore size^{165,166} but ignored the geometric parameter.

In our case the surface of the heterogeneous catalysts (PSiM) is dynamic creating a metastate.¹⁶⁷ This fluctuation is related to the chemical and physical changes that occur on the

surface of PSiM. Previously was mention that both the PSiM and PSiM-NH₂La increase its ZP values in contact with the buffer solution. This increase is related to the formation of the metastate.

The use of external forces also influences the formation of more active surfaces. Hydrodynamics¹⁶⁸ is a fundamental aspect in systems involving the transport of water molecules in mesoporous silica.¹⁶⁹ It seems that the molecular configuration of water adsorbed on the hydrophilic PSiM surface affects the catalytic activities. Asay and Kim¹¹² reported the evolution of the adsorbed water layer structure on silicon oxide at room temperature. They report the formation of three layers: “ice-like”, transitional and liquid water. They concluded that “hydrogen bonding with immobilized surface hydroxyl groups (Si-OH) affects the molecular configuration of the adsorbed water at ambient conditions. The equilibrium structure of the outermost layer varies in three different regions of the adsorption isotherm. In low humidity (relative humidity below 30%), the adsorbed water forms an ice-like layer on the surface at room temperature. The hydrogen bonding network on the silicon oxide surface that propagates up to ~3 network structure competes with the liquid water structure in the RH range of 30-60%, above which the liquid structure dominates. These structural transitions have profound effects on the adsorption isotherm of water and the behavior of the silicon oxide surface in different environments.” Therefore, the nature of the water layers formed on the *static* surface of PSiM and PSiM-NH₂La may affect the catalytic activity.

4.2.4 Development of a mathematic model to describe the effect of the structural changes of PSiM-NH₂La on the hydrolysis of BDNPP

As the BDNPP catalyzed-hydrolysis is an indirect measure of the overall change on the surface of PSiM-NH₂La, is necessary to treat the system in terms of dispersive kinetics. Plonka¹⁷⁰ defined dispersive kinetics as dynamical processes in which many timescales coexist. This is the case for the hydrolysis of the BDNPP and the surface changes on the PSiM-NH₂La and PSiM. The rate constants for dispersive processes are influenced by time. In the case of a chemical reaction, the time dependency of the rate coefficient, $k(t)$ (termed the specific reaction rate) is describe in the following way. Reactions by their nature have to excite “reactivity distributions” of the reactants in the medium, as the most reactive species are the first ones to disappear from the system. The amount of this disruption is on the ratio of reaction rates to the rate of inner reorganizations (mixing or in our case develop of a most active surface) in the system bringing back the original distribution of reactants. If the rates of chemical reactions exceed the rates of internal rearrangements, then the initial distributions in reactant reactivity are not preserved

during the course of reactions and the specific reaction rates depend on time. Otherwise the extent of disturbance is negligible and classical kinetics, with a constant specific reaction rate (k) may be valid as an approximation.

To gain further insight into the mechanism, we fit the kinetic data to a kinetic model that consider the structural changes that occur in PSiM and PSiM-NH₂La. The Avrami equation is a useful tool, used to describe how solids transform from one phase to another at constant temperature.¹¹⁹ It has been used to explain the nucleation processes that lead to the formation of mesoporous silica.¹⁷¹ For this reason we found it a valuable tool to explain the “reverse” process. The structural change in PSiM and PSiM-NH₂La occurs as consequence of its hydration in aqueous systems. The kinetic profile for the PSiM-NH₂La (Figure 4.1) seems to follow two consecutive first-order kinetics. One stage occurs in the beginning of the reaction, at which no structural change is expected. The other apparent stage is observed after 1500 min when the catalytic activity increases considerably. The kinetic behavior for integrated rate laws is discussed in many physical chemistry textbooks,^{172,173} viz:



in which an initial reactant A reacts to give the intermediate B, which then reacts to the final product D (Scheme 4.2). Furthermore, it is commonly presumed that each step is first order with respect to the reactant:

$$\text{rate (reaction 1)} = k_1[A] \quad (4.2)$$

$$\text{rate (reaction 2)} = k_2[B] \quad (4.3)$$

By setting up differential forms for the change in concentrations of A, B, and D, these differential forms can be manipulated and ultimately integrated to get expressions for three time-dependent concentrations. These expressions are:

$$[A]_t = [A]_0 e^{-k_1 t} \quad (4.4)$$

$$[B]_t = \frac{k_1[A]_0}{k_2 - k_1} (e^{-k_1 t} - e^{-k_2 t}) \quad (4.5)$$

$$[D]_t = [A]_0 \left[1 + \frac{1}{k_1 - k_2} (k_2 e^{-k_1 t} - k_1 e^{-k_2 t}) \right] \quad (4.6)$$

These equations are taken as premise for our system and comparison to the approach used next. In order to take into consideration, the change in the structure of the catalyst, we applied the Avrami equation to describes how solids transform from one phase (state of matter) to another at constant temperature. This equation was originally applied to describe the kinetics of crystallization but has also been used for other changes of phase in materials, like chemical

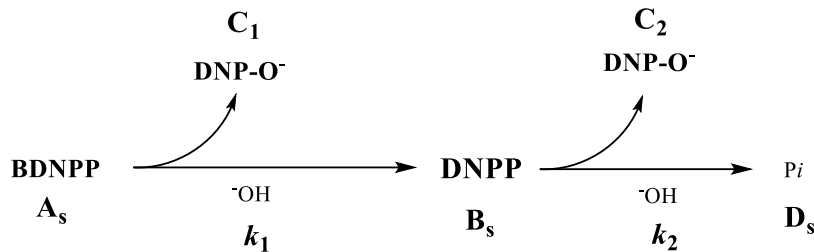
reaction rates, and even for analyses of environmental systems. According to the original paper by Avrami¹²⁰ a relationship for a phase change at a constant temperature is described as follow:

$$1 - V = e^{-Bk^t} \quad (4.7)$$

where V is the fraction transformed at time t , B is a temperature dependent constant, k is a constant varying between 1 and 4 that depends on nucleation and growth mechanisms. Since its conception, the Avrami equation has been applied by many workers^{122,123} and is commonly written as:

$$F = 1 - e^{-(Kt)^n} \quad (4.8)$$

Adding this equation to the two consecutive first-order kinetic model scheme 4.2,¹⁷⁴ the following set of equations is obtained:



Scheme 4. 2. Hydrolysis reaction of BDNPP, showing the representation used in the analysis.

$$[C] = [C]_o + [C_1] + [C_2] \quad (4.9)$$

$$[C_2] = [D] \quad (4.10)$$

$$a_1 = k_1 + k_{1\alpha}F \quad (4.11)$$

$$a_2 = k_2 + k_{2\alpha}F \quad (4.12)$$

$$[D] = A \left(1 - \left(\frac{a_2 * e^{-a_1 t} - a_1 * e^{-a_2 t}}{a_2 - a_1} \right) \right) \quad (4.13)$$

$$[C_1] = A(1 - e^{-a_1 t}) \quad (4.14)$$

where $[C]$ is the total concentration of DNP-O^- , $[D]$ is the concentration of phosphate ion formed as final product, a_1 and a_2 are the rate constants of the overall system. Equations 4.15 is the rate law for a consecutive reaction that considers the rate constants of each step and the function (F) of the Avrami Equation (Eq. 4.8). Parameters a_1 and a_2 are the respective rate constants for cleavage of BDNPP and DNPP, which are affected by the phase change in the catalyst, controlled by K , so that $a_1 = k_1 + k_{1\alpha}F$ and $a_2 = k_2 + k_{2\alpha}F$. Abs_t , Abs_o and Abs_{eq} represent the absorbances at time t , zero and required to give one equivalent of DNP, respectively. Eq.

4.15 was used to fit the kinetic data for PSiM-NH₂La in pH 8.1 obtaining the graphic shown on figure 4.11.

$$Abs_t = Abs_o + Abs_{eq} (1 - e^{-a_1 t}) + Abs_{eq} \left(1 - \frac{1}{a_2 - a_1} (a_2 e^{-a_1 t} - a_1 e^{-a_2 t}) \right) \quad (4.15)$$

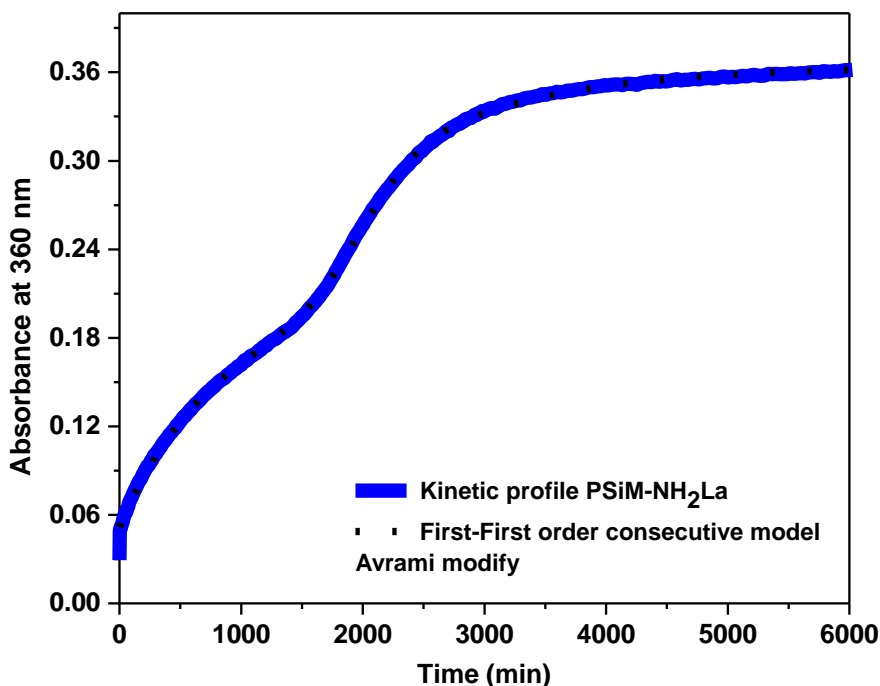


Figure 4. 11. Absorbance at 360nm as a function of time for the hydrolysis reaction of BDNPP in the presence of PSiM-NH₂La pH 8.14 and 25 °C, showing the fit obtained using the Avrami equation and the parameters shown in Table 4.5.

Table 4. 5. Kinetic parameters found for the data fit using the modify consecutive kinetic model (equation 4.15).

Parameter	Value
Absorbance one equivalent of DNP	$0.15 \pm 2.22 \times 10^{-4}$
Initial Absorbance	$0.05 \pm 3.52 \times 10^{-4}$
n (Avrami exponent)	5.44 ± 0.081
	$10^4 k_{obs} \text{ (min}^{-1}\text{)}$
k_1	12.2 ± 0.07
k_{1a}	0
k_2	0
k_{2a}	9.33 ± 0.11
K	4.54 ± 0.17

The data fit in Figure 4.11 and table 4.5 agrees quite well to the experimental data. A is the absorbance for one equivalent of DNP, $k_1 = 12.2 \times 10^{-4} \text{ min}^{-1}$ is the kinetic constant for the first step of the reaction, a value close to the one mentioned before (table 3.5, pag.61). k_{1a} is near

zero and tells how much the change in the PSiM-NH₂La structure influences the first reaction step, a zero value obviously indicates that the change in structure is not large enough to influence k_1 . $k_2=0$ and $k_{2a}=9.33 \times 10^{-4} \text{min}^{-1}$ are the estimated rate constants for the second step of the reaction, which difference from k_1 , have magnitudes indicative that changes in the PSiM structure is quite determinant at the second reaction step. The K is the Avrami constant for the structural change and n is the Avrami exponent. The value of $n = 5.4$, indicates that the loss of structure is a three-dimensional process, and because is over 4, implicates that an autocatalytic process occurs.^{175,176} This phenomenon is expected by rationalizing the cooperative forces involved in the stabilization of the PSiM.

4.3 Conclusion

The observations in this chapter show the intrinsic relationship between the structural and surface characteristics of PSiM and PSiM-NH₂La with its catalytic activity. A decrease on the surface area of PSiM and PSiM-NH₂La materials recovered after its use in aqueous medium indicate partial loss in the arrangement of the porous network. The physical characteristics are affected by chemical changes (confirmed by ²⁹Si MAS NMR) that occur on the PSiM surface. The induction period is associated to the creation of more or better suited active sites that catalyze the BDNPP hydrolysis, formation of the silanol groups from the siloxane groups. But it was found that external physical factors can accelerate this induction period on the surface of the material. Imbibition of liquids in porous hosts is driven by capillarity invasion and dynamics of water. We propose the existence of a paranematic phase due to the molecular alignment induced by the pore walls, constructing a metastable and more catalytically active sites.

A mathematical model was developed to describe the kinetic profile observed for the hydrolysis of BDNPP in the presence of PSiM-NH₂La. Avrami kinetics was used in the form of the Avrami equation, which described properly the kinetic data. Because in the system a transformation of the siloxane groups to the silanol groups, adjust to the conditions of the Avrami equation (that describes how solids transform from one phase to another at constant temperature). The Avrami constant ($n = 5.4$) indicates that the hydration involves autocatalysis, as observed BDNPP hydrolysis catalyzed by as-synthesized PSiM, the burst in the catalytic activity after the induction time suggests that silanol groups neighboring siloxane groups favors the hydroxylation in a cooperative manner. Therefore, when silanol groups aids the hydroxylation of remaining siloxane groups, the population growth and the catalytic power for both siloxane and BDNPP hydrolyses increase quickly.

5 PSiM FUNCTIONALIZED WITH CARBOXYL GROUP ADORNED WITH LN (III)

In order to evaluate the importance of the functional group on the PSiM surface for binding of lanthanide ions and the importance of the lanthanide ions added, we built new materials

containing carboxyl ligands that were adorned with La^{3+} (PSiM-COOLa), Eu^{3+} (PSiM-COOEu), and Ho^{3+} (PSiM-COOHo). Therefore, this chapter presents the characterization of PSiM-COOH and its lanthanide bound forms PSiM-COOLn, which were applied for catalysis of the BDNPP hydrolysis.

5.1 Characterization of the PSiM-COOH and PSiM-COOLn.

As done before for the amino based materials, PSiM-COOH and PSiM-COOLn were characterized in relation to composition, morphology, and properties.

5.1.1 Infrared spectroscopy

Figure 5.1 presents the FT-IR spectra of PSiM and PSiM carboxyl hybrid materials. As observed for the amino based materials, the asymmetric (ν_{as} , Si–O–Si) stretching vibration at 1080 cm^{-1} for the mesoporous framework is the strongest band, while the symmetric characteristic band (ν_s , Si–O–Si) is found at 795 cm^{-1} . The asymmetric and symmetric stretching vibrations of the methylene groups are shown near 2950 cm^{-1} for the modified PSiMs (Figure 5.1b green, red, and blue). The FT-IR spectrum of PSiM-CN presents a band near 2500 cm^{-1} assigned to the CN stretching¹⁷⁷ (Figure 5.1d), which after hydrolysis to PSiM-COOH disappear to afford the band near 1720 cm^{-1} for the C=O stretching peak (Figure 5.1c).

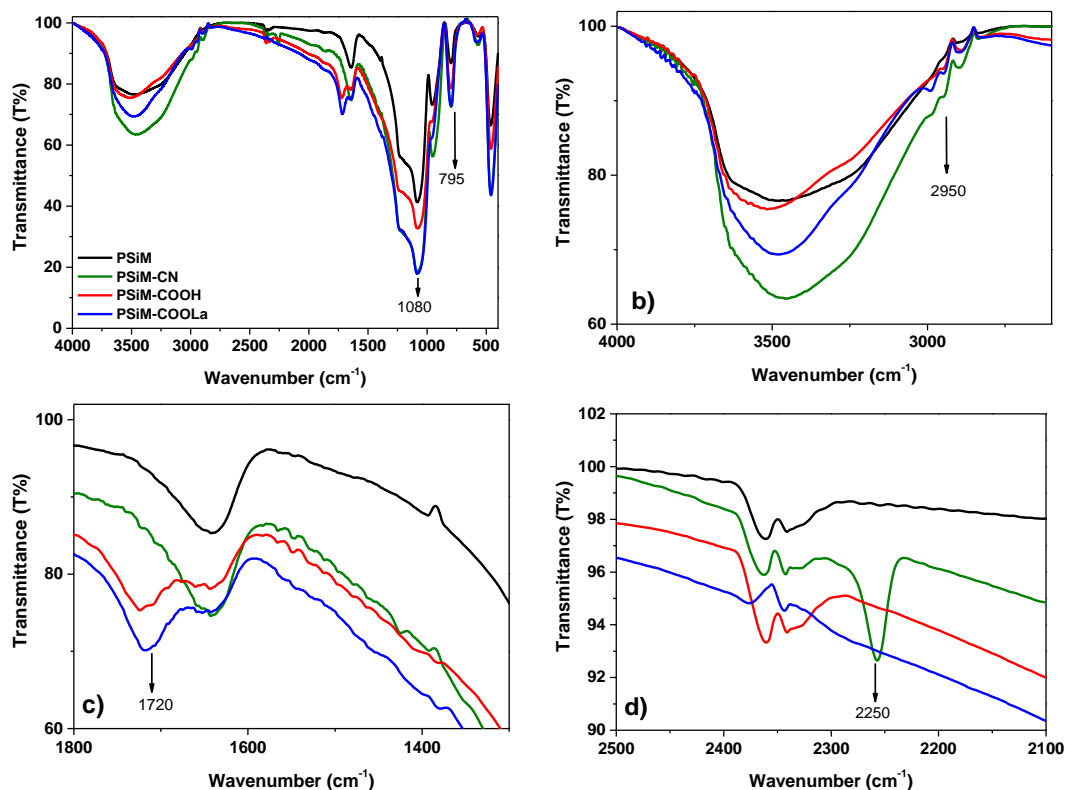


Figure 5. 1. The FT-IR spectra of PSiM in black, functionalized with cyano and carboxyl acid groups in green and red, respectively, and the lanthanide complex with carboxyl groups in blue.

5.1.2 Thermo gravimetric analysis (TGA)

Figure 5.2a shows the TGA for PSiM and its functionalized forms in air. As discussed previously, PSiM presents two distinct stages of weight loss related to water desorption (25-140°C) and water loss via condensation of silanol groups to form siloxane bonds (>250°C). The functionalized materials show two or three distinct stages of weight loss. The PSiM-CN presents two thermal events, 25-190°C and 200-600°C, due to water desorption and combustion of the organic moiety, which indicates the successful incorporation of the aliphatic chain on the silica surface. For PSiM-COOH and the PSiM-COOLa, the combustion of the organic moiety (200-600°C) is divided in two stages which is a common behavior for carboxyl containing materials (Figure 5.2b).^{178,179} In all cases combustion occurs concomitantly with the water loss via condensation of silanol groups to form siloxane bonds.

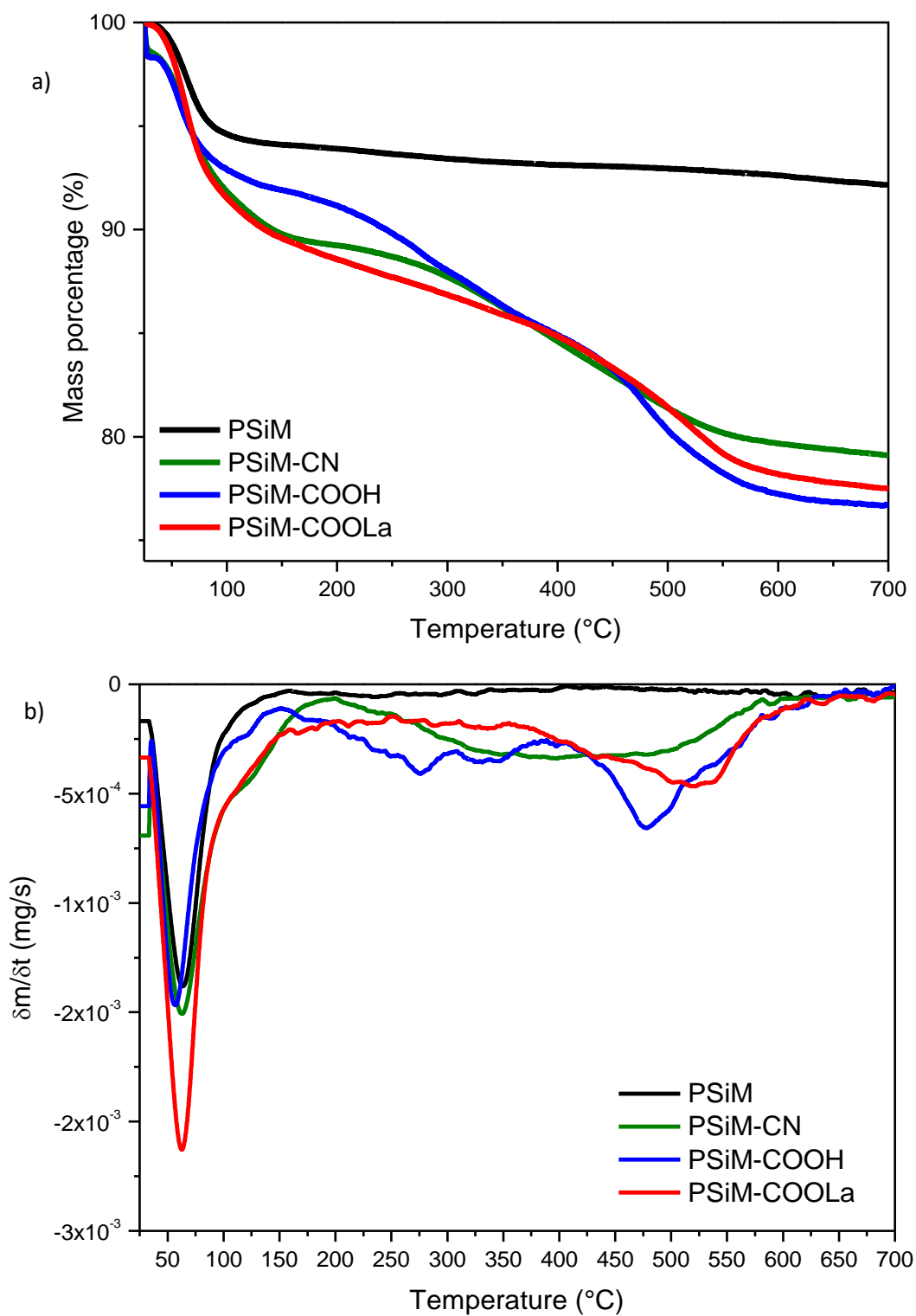


Figure 5. 2. a) TGA and b) first derivate of TGA for PSiM (black), PSiM-CN (green), PSiM-COOH (blue), and PSiM-COOLa (red).

5.1.3 Elemental analysis

Table 5.1 presents the results for elemental analysis of PSiM and its functionalized forms. An increase in the percentage of carbon and nitrogen in each of the modified samples was observed as expected. For PSiM-CN was found 3.01% of carbon and 0.60% nitrogen in a molar relationship of $6.0 \frac{\text{mol C}}{\text{mol N}}$, which is higher than expected ($4.0 \frac{\text{mol C}}{\text{mol N}}$). This result implies a small contamination ($\approx 0.6\%$) of organic matter. Since contamination relies on nitrogen-free organic solvents used in the synthetic procedures (e.g. toluene and ethyl ether), the nitrogen content was considered to determine the degree of functionalization as 2.9%, which was calculated from the amount of 4.28×10^{-2} mol N (calculated as shown below) and the molecular formulae for the organic moiety ($\text{C}_4\text{H}_6\text{N}$, M.W. 68.09).

$$\frac{0.6 \text{ g N}}{14.01 \text{ g mol}^{-1}} = 4.28 \times 10^{-2} \text{ mol}$$

0.428 mmol of N per gram of material

Table 5. 1. Mass percentages from elemental analysis for PSiM and its functionalized forms

Sample	%C	%H	%N
PSiM-CN	3.09 ± 0.17	0.69 ± 0.01	0.60 ± 0.03
PSiM-COOH	3.16 ± 0.05	1.35 ± 0.49	0.16 ± 0.04
PSiM-COOLa	3.73 ± 0.06	0.67 ± 0.50	0.23 ± 0.07
PSiM-COOEu	4.91 ± 0.16	0.65 ± 0.21	0.28 ± 0.24
PSiM-COOHo	4.1 ± 0.02	1.04 ± 0.20	0.14 ± 0.02

5.1.4 Total-reflection X-ray fluorescence (TXRF)

Figure 5.3 depicts the TXRF spectra for PSiM-COOLn. The La^{3+} cation of PSiM-COOLa (Figure 5.3a) shows signals for $L_{\alpha 1}$ and $L_{\beta 1}$ emissions at 4.65 and 5.04 keV, respectively. The Eu^{3+} cation of PSiM-COOEu (Figure 5.3b) shows signal for $L_{\alpha 1}$ emission at 5.75 keV, seen at 6.68 keV for the Ho^{3+} cation in PSiM-COOEu (Figure 5.3c). Table 5.2 reports the quantitative results the three samples, providing amounts of 1.5% of La, 0.05% of Eu and 0.09% of Ho for the corresponding PSiM-COOLn. Other elements were found in trace quantities.

Table 5. 2. Amounts of Ln in PSiM-COOLn (triplicate) as determined using TXRF

Sample	% <i>m/m</i> Ln
PSiM-COOLa	1.40 ± 0.13
PSiM-COOEu	0.05 ± 0.01
PSiM-COOHo	0.09 ± 0.01

The amount in moles of lanthanide ions were calculated assuming 1 g of material and the atomic weight of each lanthanide, the quantity in moles of Ln³⁺ in the samples was:

$$\frac{0.014 \text{ g}}{138.91 \text{ gmol}^{-1}} = 0.101 \text{ mmol of La}^{3+}$$

$$\frac{0.005 \text{ g}}{151.97 \text{ gmol}^{-1}} = 0.033 \text{ mmol of Eu}^{3+}$$

$$\frac{0.009 \text{ g}}{164.96 \text{ gmol}^{-1}} = 0.054 \text{ mmol of Ho}^{3+}$$

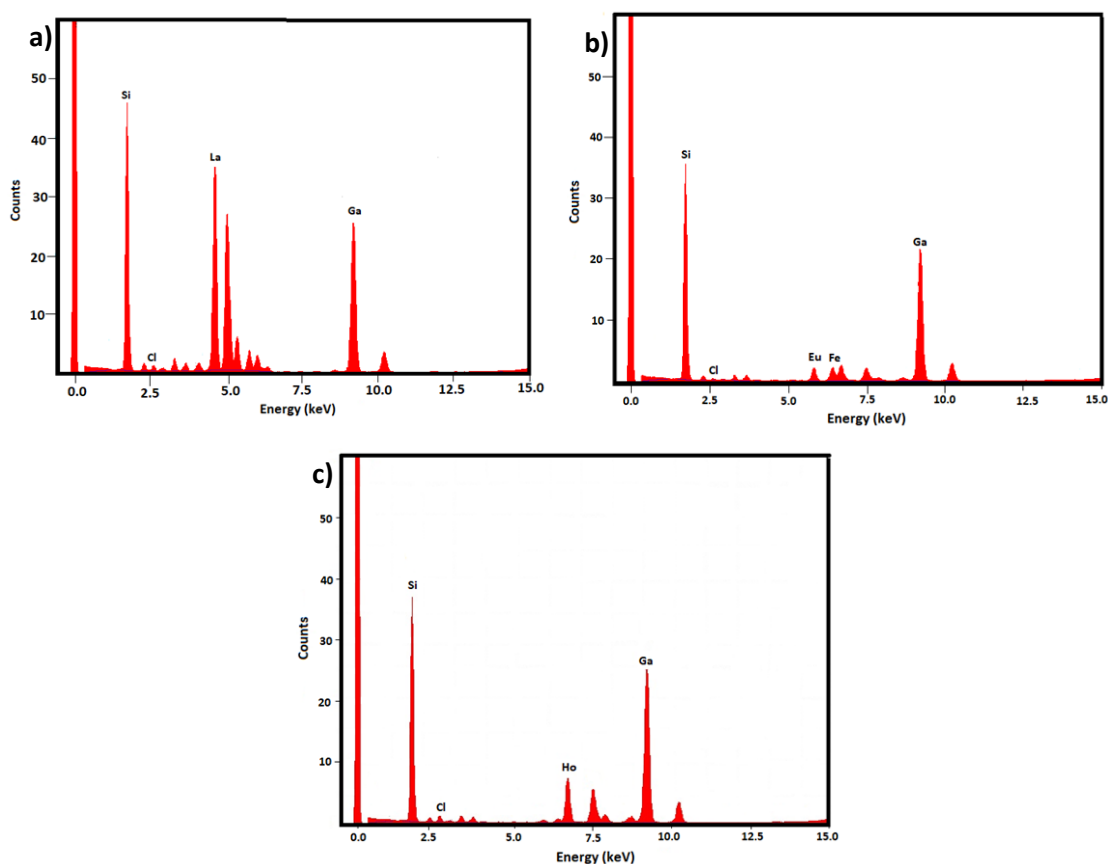


Figure 5. 3. Total-reflection X-ray fluorescence spectra of PSiM-COOLa (a), PSiM-COOEu (b), and PSiM-COOHo (c).

5.1.5 Determination of the surface area by adsorption of N₂ using the BET method

The N₂ adsorption-desorption isotherms obtained for PSiM-COOLn materials (Figure 5.4) present an isotherm type II with a hysteresis loop H3. The BET surface areas (Table 5.3) present small to non-variations in relation to the identity of the metal ion. Isotherms of all materials present a hysteresis loop H3 and do not display any restrictive adsorption at high P/P₀. This behavior can, for instance, be caused by the presence of non-rigid aggregates of plate-like silicates or association of slit-shaped pores. In our case, the generation of aggregates seems to be the cause of the presence of the H3 hysteresis loop. In the next topic this behavior will be discussed deeply.

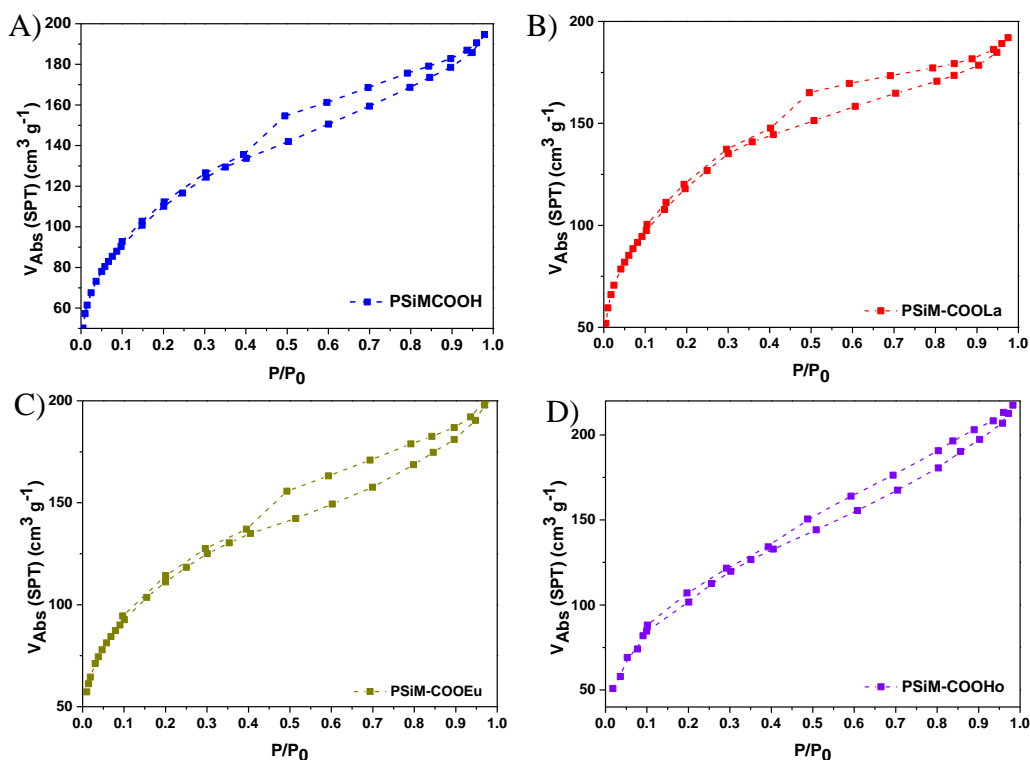


Figure 5. 4. Nitrogen adsorption-desorption isotherms for PSiM-COOLn as synthesized.

Table 5. 3. Structural properties of PSiM-COOLn, as determined from the adsorption-desorption of N₂ at 77 K).

	PSiM-COOH	PSiM-COOLa	PSiM-COOEu	PSiM-COOHo
<i>Texture parameters</i>				
Surface area (m ² g ⁻¹)	423	388	394	383
Pore Volume (cm ³ g ⁻¹)	0.16	0.14	0.15	0.19
Mean pore diameter (Å)	36.2	35.8	35.8	35.5

5.1.6 Transmission electron microscopy for the PSiM-COOH_n

Figure 5.5 presents TEM images for the PSiM-COOH_n materials. At relatively low magnification are observed the presence of extended cavities randomly distributed in the silica network, while at higher magnification, channels typical of mesoporous silica are clearly visible. Besides, the presence of multiple layers of material is observed. The pore wall size estimated by TEM is roughly 0.8 nm and the pore size is on average 2.6 nm. The porous structure observed by TEM is in agreement with the physisorption data (Fig. 5.2), which point out the occurrence of a secondary mesoporosity responsible for the capillary condensation at high relative pressure in addition to the ordered mesostructured.

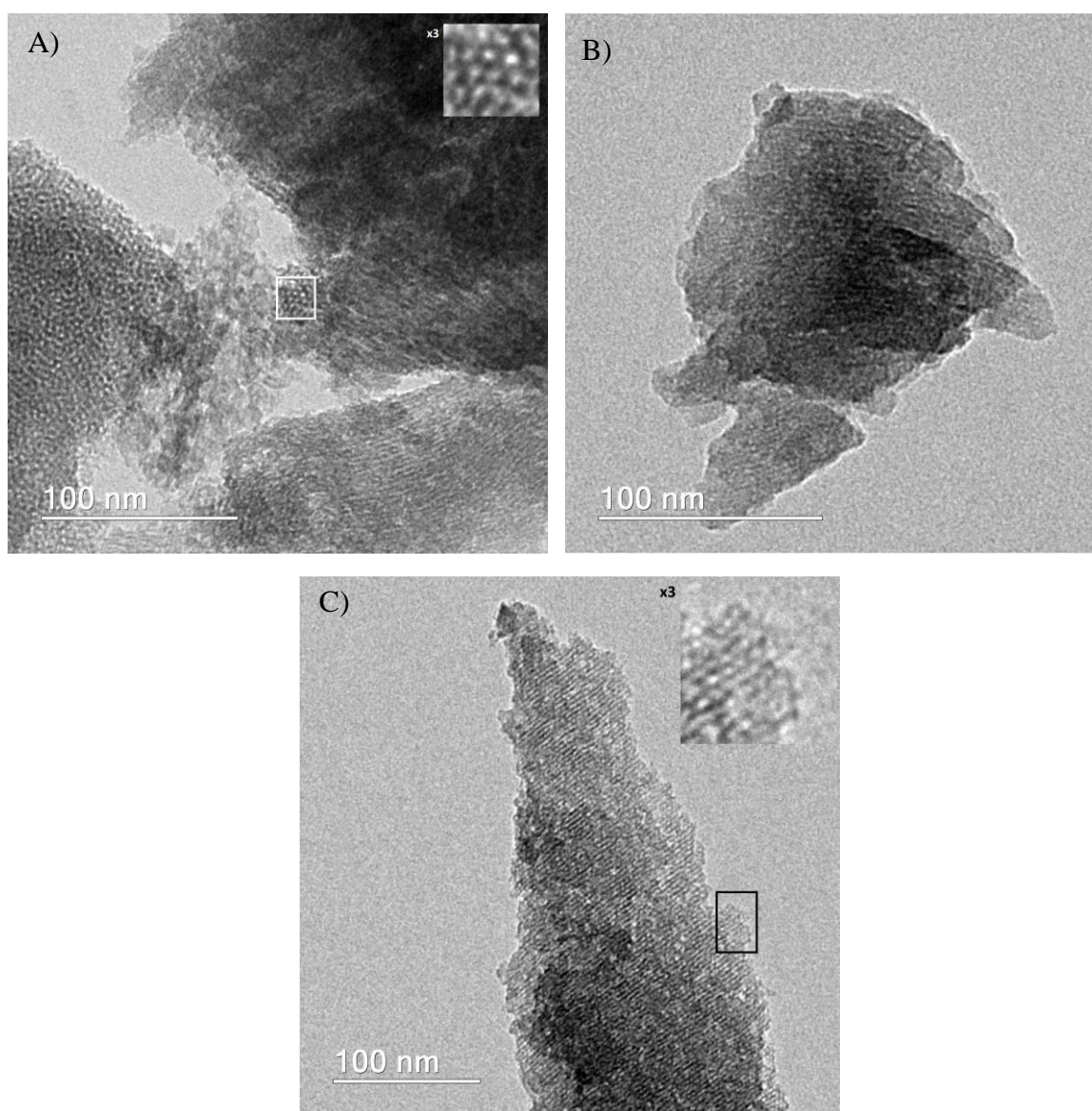


Figure 5. 5. Transmission electron microscopy (TEM) for A) PSiM-COOLa, B) PSiM-COOEu, and C) PSiM-COOHo.

5.1.7 Zeta potential and particles size

Figure 5.6 presents zeta potential and size particle for PSiM and its derivatives as a function of pH. In general, the interaction of H^+ and OH^- ions on the material surface change its charge and zeta potential. In acidic solutions, protonation of neutral sites and interaction of hydronium ions increase the zeta potential value. In basic solutions, OH^- deprotonates neutral sites and interacts with the surface lowering the zeta potential.¹⁸⁰

The unexpected behavior of the ZP values close to neutrality can be explained by analyzing the data on figure 5.6. An aggregation of the particles goes along with the increase in the zeta potential. As the size of the particles increases the ability to interact with ions from the medium decreases. Besides, the chemical nature of the functional groups and the presence of the lanthanide ions on the surface of the material creates species that may create a different double layer in each case. Another factor that can increase the ZP value on the materials is the water uptake capability of material surfaces, especially of bulk materials as in our case. When the pH is increased, acid surface groups dissociate to give negative charges. Adjacent and equally charged groups experience electrostatic repulsive forces, which provoke an expansion in the PSiM structure coating and increases the ionic conductance.

The catalytic studies presented ahead display an increase on the catalytic activity at pH above 7. Although, the activity shows a maximum at different pHs depending on the metal, which suggest the formation of different complexes on the surface of the material. In agreement, the ZP values for PSiM-COOLn also do not follow the same tendency of the material without bound lanthanides, which is also associated with the formation of different species.

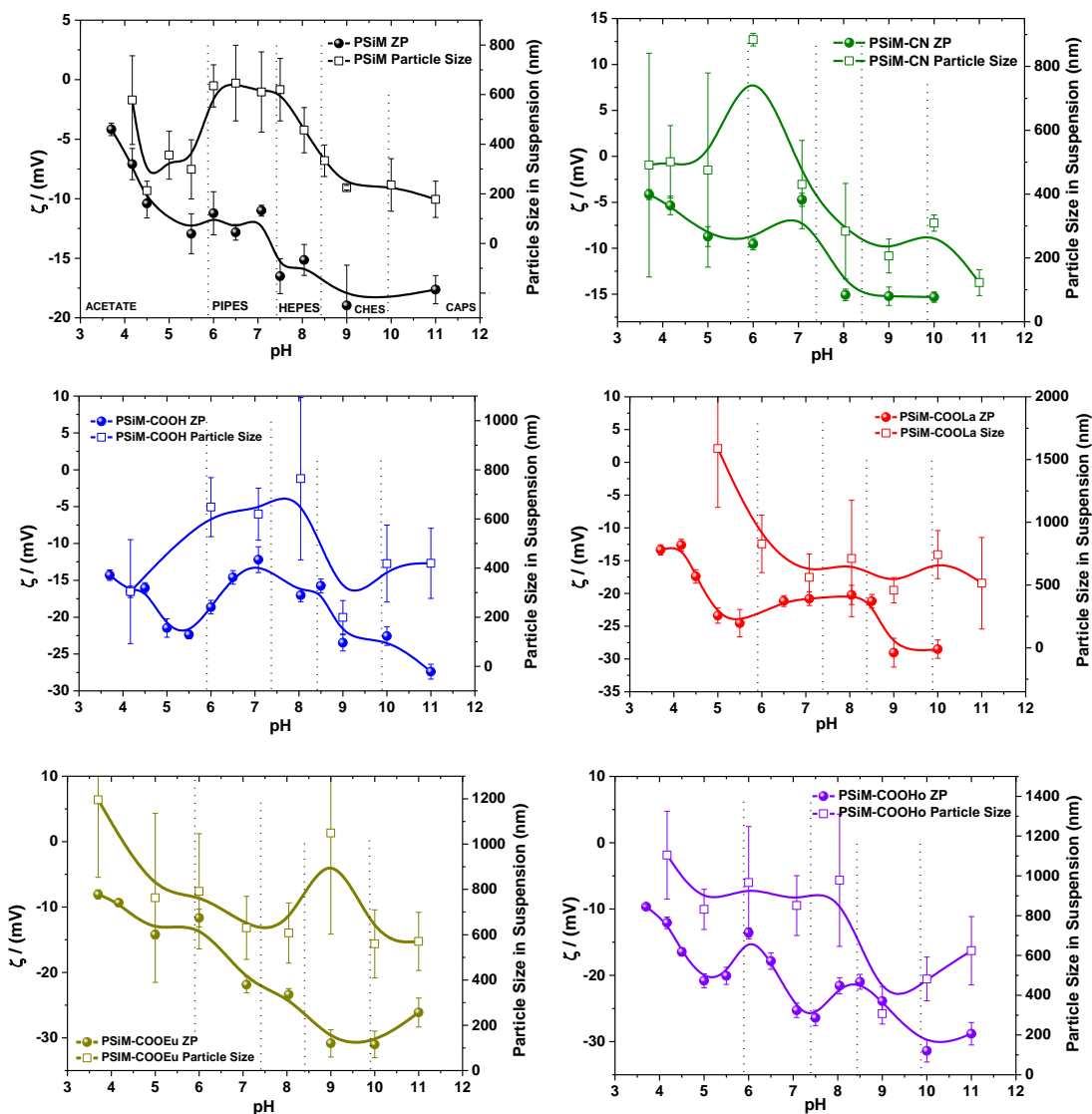


Figure 5. 6. Zeta potential and particle size as a function of pH for PSiM and its functionalized forms at 25°C. Measured in different buffer solutions (0.1 mol L^{-1}) as a dispersion of 1 mg mL^{-1} of material.

5.2 Catalytic studies

The catalytic properties of the PSiM-COOH and PSiM-COOLn materials were evaluated for the BDNPP hydrolysis, which was followed by UV-Vis spectroscopy using a flow system. The reactions were started in a thermostated water-jacketed cell containing the catalyst that had its contents pumped through a paper filter and a quartz flow cuvette. Figure 5.7 shows successive spectra overtime obtained for the BDNPP hydrolysis in the presence of each one of the materials at pH 8.0, which shows the formation of DNP at 360 nm for all the materials. The increase in absorbance at 360 nm as a function of the reaction time is presented in the figure 5.8. The kinetic

profiles follow a similar pattern obtained to PSiM and PSiM-NH₂La, which shows an induction period after which the DNP appearance speeds up. This observation also implies the formation of more active sites as seen before for PSiM-NH₂La.

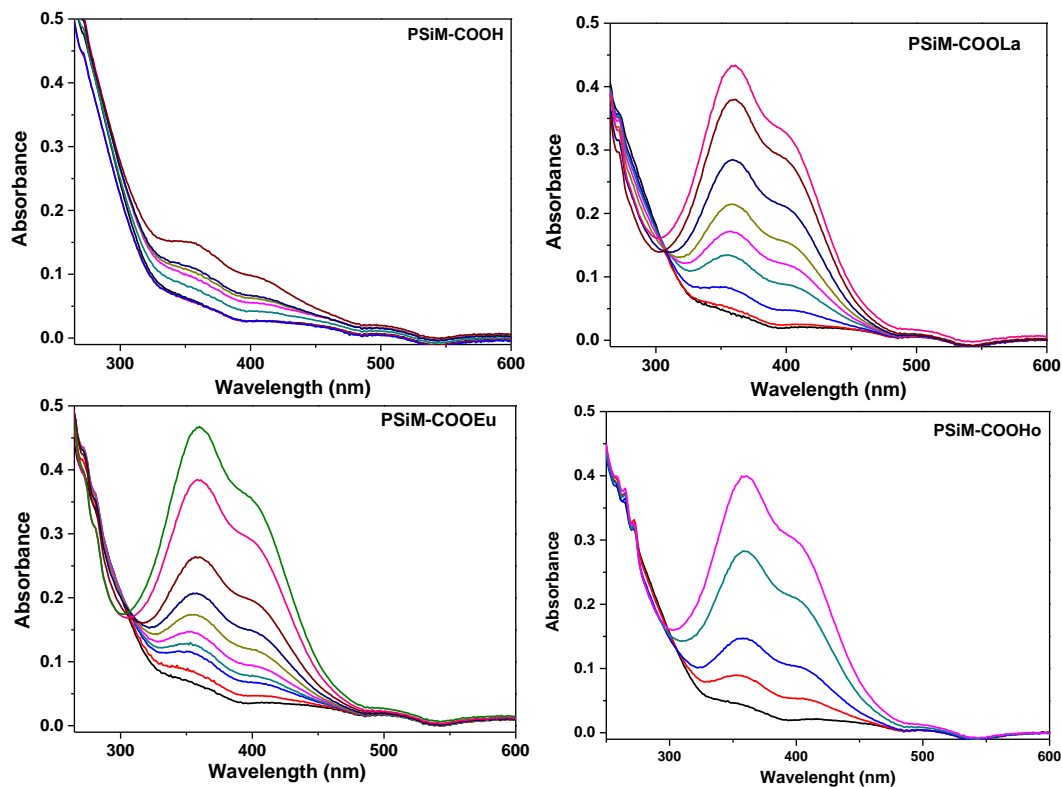


Figure 5. 7. Successive UV-Vis spectra over time for BDNPP hydrolysis catalyzed by PSiM-COOH and PSiM-COOLn.

Figure 5.8 shows that the induction time is present for all materials, although PSiM-COOEu exhibit a longer induction time. Table 5.4 reports that all three-lanthanide catalyst have more or less the same catalytic activity, with a catalytic effect varying from 31 for PSiM-COOHo to 50 for PSiM-COOLa. Therefore, the half-life of 35 days ($k_{\text{obs}}=1.38 \times 10^{-5} \text{ min}^{-1}$) for the uncatalyzed hydrolysis decreases to about 17 h ($k_{\text{obs}}=7.01 \times 10^{-4} \text{ min}^{-1}$) in the presence of PSiM-COOLa in pH 8.0 at 25 °C.

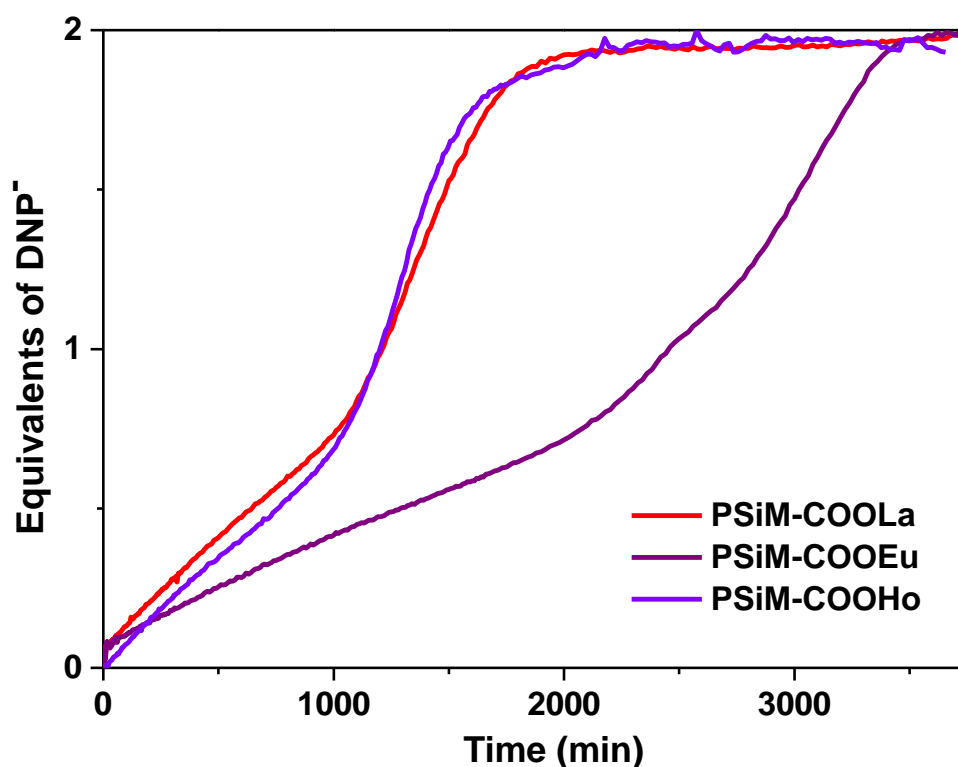


Figure 5. 8. Absorbance at 360 nm versus time for first use of the materials (PSiM-COOLn) on the BDNPP hydrolysis, at pH 8.0 and 25 °C.

5.2.1 Reuse and thermal resilience of PSiM-COOLn on the hydrolysis of BDNPP

In order to evaluate the capacity of reuse of the catalyst, 20 mg of each material were used in a buffer solution at pH 8.0 (HEPES 0.1 molL⁻¹) and washed until the signal of product of the reaction was not observed. Then, the catalysts were put in an oven to dry at 70°C for 12h. After that, the material was used for the BDNPP by 500 min of reaction to ensure that no activation would occur, this procedure was needed to evaluate only the inner activity of the catalyst. The same procedure was used in each cycle. Table 5.4 reports the rate constants for cleavage of BDNPP at each cycle as determined by initial rates according to the following equation:

$$k_{obs} = \frac{(\Delta Abs / \Delta t)}{2\epsilon b [BDNPP]} \quad (5.1)$$

The catalytic activity decreases after each cycle (Figure 5.9). However, even after four cycles of reuse the catalytic effect is still above 8-fold. This indicate that the good catalytic activity even after all the mechanical and thermal stress that the material underwent.

Table 5. 4. Kinetic parameters for reuse of PSiM-COOLn on the cleavage of *bis*-(2,4-dinitrophenyl) phosphate (BDNPP), pH 8.0 at 25 °C. The catalytic factor (*f*) was calculated in relation to the uncatalyzed reaction.¹²⁵

	PSiM-COOLa	<i>f</i>	PSiM-COOEu	<i>f</i>	PSiM-COOHo	<i>f</i>
USE	$10^4 k_{obs}(\text{min}^{-1})$					
1	7.01	51	4.88	35	4.29	31
2	4.67	34	5.25	38	2.65	19
3	1.15	8.3	1.38	10	1.17	8.5
4	1.34	9.7	1.09	8	3.11	23

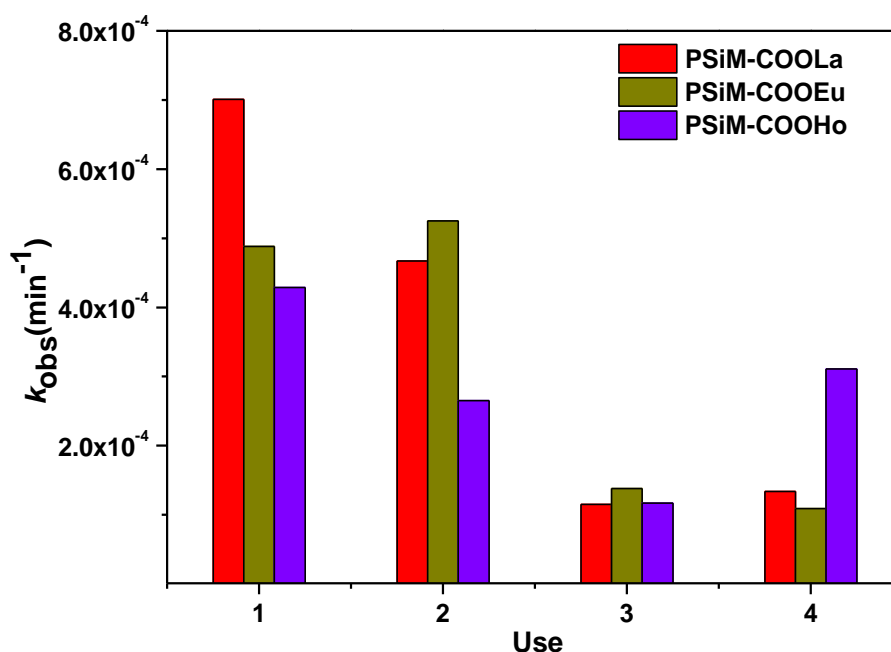


Figure 5. 9. Rate constants obtained for each use using PSiM-COOLn on the hydrolysis of BDNPP, at pH 8.0 and 25 °C

5.2.2 pH-rate profile for the catalytic activity of PSiM-COOLn on the hydrolysis of BDNPP

The catalytic activity of PSiM-COOH and PSiM-COOLn (10 mg) for the hydrolysis of BDNPP was studied in different pHs (Table 5.5). PSiM-COOH profile follows a similar profile compared to the uncatalyzed BDNPP hydrolysis (Figure 5.10)¹²⁵, nevertheless, a catalytic effect of about 6-fold is observed. This effect is twice as high as observed for the non-functionalized PSiM (Table 3.5), suggesting that the pending carboxyl group is directly involved in catalysis, very likely as a basic catalyst. The lanthanide complexes are more active than the PSiM-COOH base material.

Table 5. 5. Observed rate constants for BDNPP hydrolysis in the presence of PSiM-COOH and its lanthanide forms at different pH (buffer solution 0.1 mol L⁻¹). The catalytic factor in parenthesis (*f*) was calculated in relation to the uncatalyzed reaction.¹²⁵

Material	PSiM-COOH	PSiM-COOLa	PSiM-COOEu	PSiM-COOHo
pH	10 ⁴ k _{obs} (min ⁻¹), <i>f</i>			
6.0	0.63	3.67		3.13
7.0	0.87 (7.7)	3.24 (29)	1.09 (9.6)	1.08 (9.5)
7.5	-	-	-	6.64 (61)
8.0	0.95 (6.9)	4.15 (30)	1.07 (7.8)	-
9.0	0.92 (3.9)	10.6 (45)	2.56 (11)	10.8 (46)
9.5	-	1.47	2.37	6.86
10.0	3.13 (5.7)	1.44 (2.6)	1.02 (2.2)	1.38 (2.5)

The pH-rate profile for the PSiM-COOLn materials can be divided in three regions: *i.* a pH-independent region below pH about 7; *ii.* a pH-dependent region between pH 7 and 9, in which a catalytic effect is observed; and, *iii.* a pH-dependent region at pH > 9 characterized by a decrease on the catalytic activity. The pH-dependent regions below pH 9 show slopes of 0.3 for PSiM-COOLa, 0.2 for PSiM-COOEu and 0.4 for PSiM-COOHo. Above pH 9, are observed slopes of -0.8 for PSiM-COOLa, -0.3 for PSiM-COOEu and -0.9 for PSiM-COOHo. These behaviors do not indicate a single acid-base equilibrium that would give a slope of 1, but rather suggests complex equilibria involving multiple sites near each other. This behavior is typical of solid matrixes, in which acidity of surface groups are affected by interactions with neighboring groups.¹⁸¹ It is worth mentioning that species distributions for lanthanide complexes in homogeneous conditions are characterized by complex behaviors of many acid/base forms.^{182, 46, 183, 184} The shape of the graphic presented in Figure 5.10 indicates an environment dependent on the concentration of ⁻OH above pH 9, where a decrease on the catalytic activity is observed. We consider two different species population to explain this behavior (Figure 5.11). Between pH 7 and 9, deprotonation of water molecules bound to Ln³⁺ form more catalytic active species. However, above pH 9, the formation of Ln³⁺ species containing more hydroxide bound ions result in less active species with lack of vacancies for coordination of the substrate.

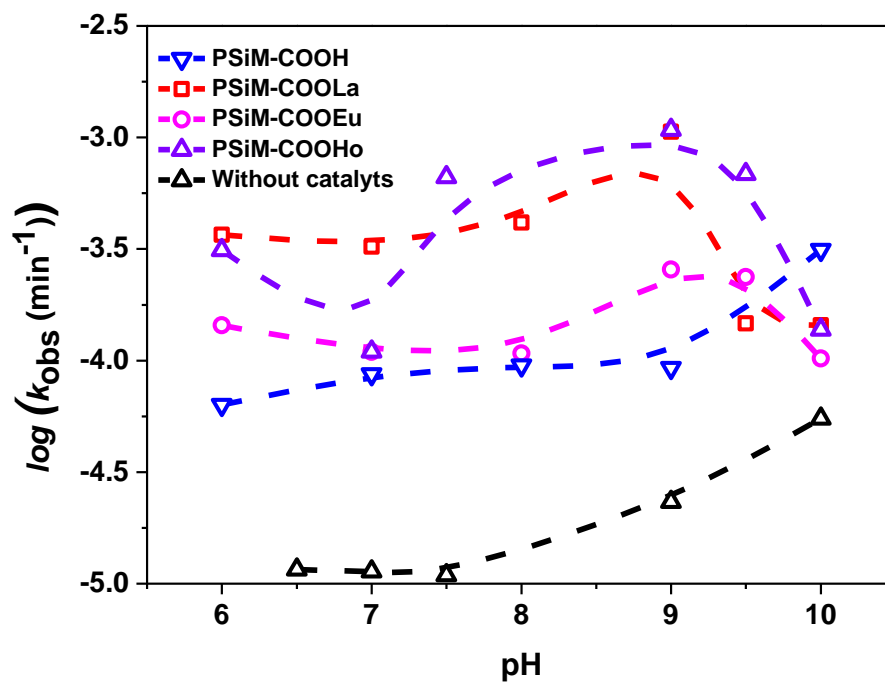
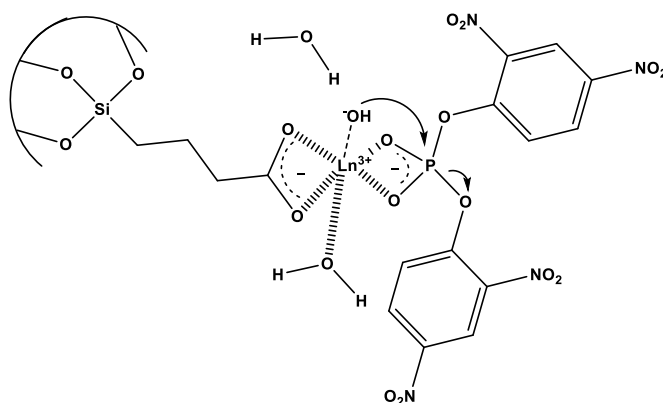


Figure 5. 10. pH-Rate profile for *bis*(2,4-dinitrophenyl)phosphate (BDNPP) hydrolysis in the presence of PSiM-COOH and PSiM-COOH_{Ln} at 25 °C.

Below pH 9



Above pH 9

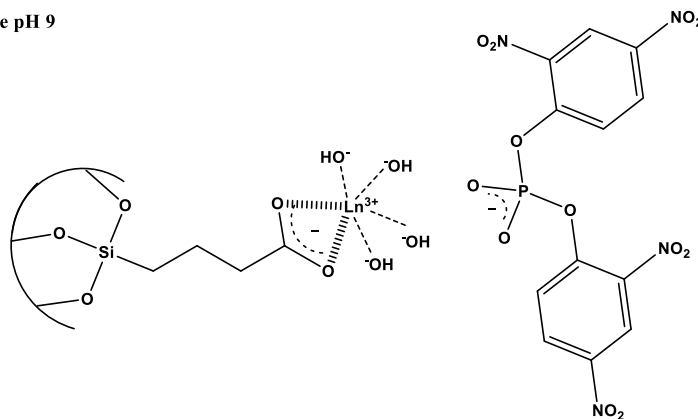


Figure 5. 11. Proposed species for the BDNPP cleavage by PSiM-COOL_n at different pH below and above pH 9.

5.3 Conclusion

In summary, new porous silica materials with high surface area ($S_{\text{BET}} \approx 390 \text{ m}^2 \text{ g}^{-1}$), functionalized with carboxyl groups and coordinated to lanthanide ions were synthesized and used as catalyst for BDNPP hydrolysis. In the first use of the catalyst at pH 8.0, catalysis was on the range of 30 to 50-fold faster than observed for the uncatalyzed hydrolysis. The PSiM-COOLn was resilient to thermal stress presenting good activities after four cycles of use. Lanthanide ion activated metal bound hydroxide ions, involved in the nucleophilic attack on the electrophilic substrate. Optimal catalysis is observed at pH near to 9 due to the formation of a species that may both activate the hydroxide ions and bind the substrate.

6 GENERAL CONCLUSION AND PERSPECTIVES

New carboxyl and amine-based Porous Silica Materials (PSiM) were synthesized. The organic groups allowed the inclusion of lanthanide ions that afforded Lewis acid features to the PSiM surface. This characteristic enhanced the catalytic activity of the materials for the hydrolysis of a model phosphodiester: BDNPP. The catalytic effect (f) for first use at pH 8.1 and 25°C varied from 8 for PSiM-COOEu to 38 for PSiM-NH₂La. Surprisingly, activities during reuse were considerably higher ($f = 612$). The catalytic behavior is pH-dependent on surface chemical speciation that differs depending on the nature of the organic moiety and metal. In the case of PSiM-NH₂La a bifunctional action is observed, the amine groups attracted BDNPP from the solution and a water molecule coordinated to a lanthanum ion attack the BDNPP. Besides, the results show that the presence of any lanthanide ion on the surface of PSiM-COOLn accelerate BDNPP cleavage, independent of the lanthanide nature.

An interesting feature in the use of PSiM and its functionalized forms was an induction period, after it the reaction rate for BDNPP hydrolysis increases substantially. The growth in the catalytic activity and the induction period itself suggests changes on the surface physical-chemical characteristic of PSiM and its derivatives. Solid state NMR data suggest that catalysis depends on interconversion from siloxane to silanol groups, which form a more active surface for BDNPP hydrolysis. A kinetic model based on the Avrami equation was developed to fit the experimental data. The Avrami constant, n of 5.4 implied autocatalytic effects, which silanol hydroxylation favors the hydroxylation of remaining siloxane groups in a cooperative fashion. As result, silanol population growth and the catalytic power for both siloxane and BDNPP hydrolyses increase quickly.

The mechanism by which the reaction occur is highly dependent on the chemical nature of the functionalization, but the catalytic activities are intriguingly similar despite of the organic moiety. An unexpected performance ($f = 612$ for PSiM-NH₂La at pH 8.1 and 25°C) was found during the reuse of the materials, this increase in activity was associated to the structural changes describe above, which create a better suited catalytic matrix for the BDNPP hydrolysis.

It is remarkable that there are so few reports about the role of structural changes in silicas for catalysis of phosphate ester cleavage. Further studies can rely on these phenomena in order to develop systems with interesting applications. It is worth remembering in those studies other silica and hydroxylated materials to determinate how morphology, crystallinity, isomorphism, and chemical composition can affect catalysis. In addition, engineering, physics and chemical

studies may be done in sync to develop a silica-flow system for clearance of phosphoester compounds in aqueous media. It would be quite interesting to determinate if the induction period occurs for other class of compounds and materials.

7 REFERENCES

- (1) Domingos, J. B.; Longhinotti, E.; Gageiro, V.; Nome, F. A Química Dos Ésteres de Fosfato. *Quim. Nova* **2003**, *26* (5), 745–753.
- (2) Schroeder, G. K.; Lad, C.; Wyman, P.; Williams, N. H.; Wolfenden, R. The Time Required for Water Attack at the Phosphorus Atom of Simple Phosphodiester and of DNA. *Proc. Natl. Acad. Sci. U. S. A.* **2006**, *103* (11), 4052–4055.
- (3) Hird, F. J. R.; McLean, R. M. Synthesis of Phosphocreatine and Phosphoarginine by Mitochondria from Various Sources. *Comp. Biochem. Physiol.* **1983**, *76B* (1), 41–46.
- (4) Yang, Y. C.; Baker, J. a; Ward, J. R. Decontamination of Chemical Warfare Agents. *Chem. Rev.* **1992**, *92* (8), 1729–1743.
- (5) Vijaya, S.; Sudhakar, Y.; Venkateswarlu, B. Current Review on Organophosphorus Poisoning. *Arch. Appl. Sci. Res.* **2010**, *2* (4), 199–215.
- (6) Eddleston, M.; Buckley, N. A.; Eyer, P.; Dawson, A. H. Management of Acute Organophosphorus Pesticide Poisoning. *Lancet* **2008**, *371* (9612), 597–607.
- (7) Cowan, J. A. Chemical Nucleases. *Curr. Opin. Chem. Biol.* **2001**, *5* (6), 634–642.
- (8) Zhang, L.; Li, B.; Meng, X.; Huang, L.; Wang, D. Degradation of Four Organophosphorous Pesticides Catalyzed by Chitosan-Metal Coordination Complexes. *Environ. Sci. Pollut. Res.* **2015**, *22* (19), 15104–15112.
- (9) Muxel, A. A.; Neves, A.; Camargo, M. A.; Bortoluzzi, A. J.; Szpoganicz, B.; Castellano, E. E.; Castilho, N.; Bortolotto, T.; Terenzi, H. New La(III) Complex Immobilized on 3-Aminopropyl-Functionalized Silica as an Efficient and Reusable Catalyst for Hydrolysis of Phosphate Ester Bonds. *Inorg. Chem.* **2014**, *53* (6), 2943–2952.
- (10) Beck, J. S.; Vartuli, J. C.; Roth, W. J.; Leonowicz, M. E.; Kresge, C. T.; Schmitt, K. D.; Chu, C. T.-W.; Olson, D. H.; Sheppard, E. W.; McCullen, S. B.; et al. A New Family of Mesoporous Molecular Sieves Prepared with Liquid Crystal Templates. *J. Am. Chem. Soc.* **1992**, *114* (27), 10834–10843.
- (11) Kresge, C. T.; Leonowicz, M. E.; Roth, W. J.; Vartuli, J. C.; Beck, J. S. Ordered Mesoporous Molecular Sieves Synthesized by a Liquid-Crystal Template Mechanism. *Nature* **1992**, *359* (22), 710–712.
- (12) Gómez-Tagle, P.; Yatsimirsky, A. K. Phosphodiester Hydrolysis by Lanthanide Complexes of Bis-Tris Propane. *Inorg. Chem.* **2001**, *40* (15), 3786–3796.
- (13) Tsubouchi, A.; Bruice, T. C. Phosphonate Ester Hydrolysis Catalyzed by Two Lanthanum Ions. Intramolecular Nucleophilic Attack of Coordinated Hydroxide and Lewis Acid Activation. *J. Am. Chem. Soc.* **1995**, *117* (28), 7399–7411.
- (14) Oh, S. J.; Song, K. H.; Whang, D.; Kim, K.; Yoon, T. H.; Moon, H.; Park, J. W.; August, R. V. Catalytic Hydrolysis of Phosphate Diesters by Lanthanide (III) Cryptate (2.2.1) Complexes. *Inorg. Chem.* **1996**, *35* (13), 3780–3785.
- (15) Levason, W.; Schoonman, J.; Krebs, B. *Studies in Inorganic Chemistry 6 Phosphorus An Outline of Its Chemistry, Biochemistry and Technology*, Third Edit.; Elsevier B.V: New York, 1982.

- (16) Cowan, J. Metal Activation of Enzymes in Nucleic Acid Biochemistry. *Chem. Rev.* **1998**, *98* (3), 1067–1088.
- (17) Wilcox, D. E. Binuclear Metallohydrolases. *Chem. Rev.* **1996**, *96* (7), 2435–2458.
- (18) Cox, J. R.; Ramsay, O. B. Mechanisms of Nucleophilic Substitution in Phosphate Esters. *Chem. Rev.* **1964**, *64* (4), 317–352.
- (19) Westheimer, F. H. Pseudo-Rotation in the Hydrolysis of Phosphate Esters. *Acc. Chem. Res.* **1968**, *1* (3), 70–78.
- (20) Oivanen, M.; Kuusela, S.; Lönnberg, H. Kinetics and Mechanisms for the Cleavage and Isomerization of the Phosphodiester Bonds of RNA by Bronsted Acids and Bases. *Chem. Rev.* **1998**, *98* (3), 961–990.
- (21) Orth, E. S.; Brandão, T. A. S.; Milagre, H. M. S.; Eberlin, M. N.; Nome, F. Intramolecular Acid-Base Catalysis of a Phosphate Diester: Modeling the Ribonuclease Mechanism. *J. Am. Chem. Soc.* **2008**, *130* (8), 2436–2437.
- (22) Westheimer, F. H. Monomeric Metaphosphates. *Chem. Rev.* **1981**, *81* (4), 313–326.
- (23) Florián, J.; Warshel, A. Phosphate Ester Hydrolysis in Aqueous Solution: Associative versus Dissociative Mechanisms. *J. Phys. Chem. B* **1998**, *102* (4), 719–734.
- (24) Yu, L.; Li, F. Z.; Wu, J. Y.; Xie, J. Q.; Li, S. Development of the Aza-Crown Ether Metal Complexes as Artificial Hydrolase. *J. Inorg. Biochem.* **2016**, *154*, 89–102.
- (25) Franklin, S. J. Lanthanide-Mediated DNA Hydrolysis. *Curr. Opin. Chem. Biol.* **2001**, *5* (2), 201–208.
- (26) Blaskó, A.; Bruice, T. C. Recent Studies of Nucleophilic, General-Acid, and Metal Ion Catalysis of Phosphate Diester Hydrolysis. *Acc. Chem. Res.* **1999**, *32* (6), 475–484.
- (27) Edwards, D. R.; Brown, R. S. Development of Metal-Ion Containing Catalysts for the Decomposition of Phosphorothioate Esters. *Biochim. Biophys. Acta - Proteins Proteomics* **2013**, *1834* (1), 433–442.
- (28) Zhao, M.; Wang, H.-B.; Ji, L.-N.; Mao, Z.-W. Insights into Metalloenzyme Microenvironments: Biomimetic Metal Complexes with a Functional Second Coordination Sphere. *Chem. Soc. Rev.* **2013**, *42* (21), 8360–8375.
- (29) Chin, J.; Banaszczyk, M.; Jubian, V.; Zou, X. Co(III) Complex Promoted Hydrolysis of Phosphate Diesters: Comparison in Reactivity of Rigid Cis-Diaquotetraazacobalt(III) Complexes. *J. Am. Chem. Soc.* **1989**, *111* (3), 186–190.
- (30) Williams, N. H.; Takasaki, B.; Wall, M.; Chin, J. Structure and Nuclease Activity of Simple Dinuclear Metal Complexes: Quantitative Dissection of the Role of Metal Ions. *Acc. Chem. Res.* **1999**, *32* (6), 485–493.
- (31) Fothergill, M.; Goodman, M. F.; Petruska, J.; Warshel, A. Structure-Energy Analysis of the Role of Metal Ions in Phosphodiester Bond Hydrolysis by DNA Polymerase I. *J. Am. Chem. Soc.* **1995**, *117* (47), 11619–11627.
- (32) Browne, K. A.; Bruice, T. C. Chemistry of Phosphodiesters, DNA and Models. 2. The Hydrolysis of Bis(8-Hydroxyquinoline) Phosphate in the Absence and Presence of Metal Ions. *J. Am. Chem. Soc.*

- 1992**, *114* (13), 4951–4958.
- (33) Bruice, T. C.; Tsubouchi, A.; Dempcy, R. O.; Olson, L. P. One- and Two-Metal Ion Catalysis of the Hydrolysis of Adenosine 3'-Alkyl Phosphate Esters. Models for One- and Two-Metal Ion Catalysis of RNA Hydrolysis. *J. Am. Chem. Soc.* **1996**, *118* (41), 9867–9875.
- (34) Moss, R. A.; Zhang, J.; Ragunathan, K. G. Zirconium and Hafnium Cations Rapidly Cleave Model Phosphodiester in Acidic Aqueous Solutions. *Tetrahedron Lett.* **1998**, *39* (12), 1529–1532.
- (35) Bracken, K.; Moss, R. A.; Ragunathan, K. G. Remarkably Rapid Cleavage of a Model Phosphodiester by Complexed Ceric Ions in Aqueous Micellar Solutions. *J. Am. Chem. Soc.* **1997**, *119* (39), 9323–9324.
- (36) Moss, R. A.; Morales-Rojas, H. Loci of Ceric Cation Mediated Hydrolyses of Dimethyl Phosphate and Methyl Methylphosphonate. *Org. Lett.* **1999**, *1* (11), 1791–1793.
- (37) Wang, Z.; Ming, L. J.; Que, L.; Vincent, J. B.; Crowder, M. W.; Averill, B. A. ¹H NMR and NOE Studies of the Purple Acid Phosphatases from Porcine Uterus and Bovine Spleen. *Biochemistry* **1992**, *31* (23), 5263–5268.
- (38) Chandra, M.; Sachdeva, A.; Silverman, S. K. DNA-Catalyzed Sequence-Specific Hydrolysis of DNA. *Nat. Chem. Biol.* **2009**, *5* (10), 718–720.
- (39) Hegg, E. L.; Burstyn, J. N. Toward the Development of Metal-Based Synthetic Nucleases and Peptidases: A Rationale and Progress Report in Applying the Principles of Coordination Chemistry. *Coord. Chem. Rev.* **1998**, *173* (1), 133–165.
- (40) Knöfel, T.; Sträter, N. Mechanism of Hydrolysis of Phosphate Esters by the Dimetal Center of 5'-Nucleotidase Based on Crystal Structures. *J. Mol. Biol.* **2001**, *309* (1), 239–254.
- (41) Das, P.; Chandar, N. B.; Chourey, S.; Agarwalla, H.; Ganguly, B.; Das, A. Role of Metal Ion in Specific Recognition of Pyrophosphate Ion under Physiological Conditions and Hydrolysis of the Phosphoester Linkage by Alkaline Phosphatase. *Inorg. Chem.* **2013**, *52* (19), 11034–11041.
- (42) Zhang, Z. Chemical and Mechanistic Approaches to the Study of Protein Tyrosine Phosphatases. *Acc. Chem. Res.* **2003**, *36* (6), 385–392.
- (43) Klabunde, T.; Sträter, N.; Fröhlich, R.; Witzel, H.; Krebs, B. Mechanism of Fe(III)-Zn(II) Purple Acid Phosphatase Based on Crystal Structures. *J. Mol. Biol.* **1996**, *259* (4), 737–748.
- (44) Schenk, G.; Mitic, N.; Hanson, G. R.; Comba, P. Purple Acid Phosphatase: A Journey into the Function and Mechanism of a Colorful Enzyme. *Coord. Chem. Rev.* **2013**, *257* (2), 473–482.
- (45) Åqvist, J.; Kolmodin, K.; Florian, J.; Warshel, A. Mechanistic Alternatives in Phosphate Monoester Hydrolysis: What Conclusions Can Be Drawn from Available Experimental Data? *Chem. Biol.* **1999**, *6* (3), 71–80.
- (46) Cotton, S. *Lanthanide and Actinide Chemistry*; John Wiley & Sons, Ltd: West Sussex, England, 2006.
- (47) Tyler, G. Rare Earth Elements in Soil and Plant Systems - A Review. *Plant and Soil.* **2004**, *267* (1), 191–206.
- (48) Lin, K. S.; Chowdhury, S. Synthesis, Characterization, and Application of 1-D Cerium Oxide Nanomaterials: A Review. *Int. J. Mol. Sci.* **2010**, *11* (9), 3226–3251.

- (49) Longhinotti, E.; Domingos, J. B.; Da Silva, P. L. F.; Szpoganicz, B.; Nome, F. Bis(2,4-Dinitrophenyl) Phosphate Hydrolysis Mediated by Lanthanide Ions. *J. Phys. Org. Chem.* **2005**, *18* (2), 167–172.
- (50) Li, F. Z.; Feng, F.; Yu, L.; Xie, J. Q. The Metallomicelle of Lanthanide Metal (Ce, La) Aza-Macrocyclic Complexes with a Carboxyl Branch: The Catalytic Activity and Mechanism in the Hydrolysis of a Phosphate Diester. *J. Solution Chem.* **2014**, *43* (8), 1331–1343.
- (51) Morrow, J. R.; Buttrey, L. A.; Berback, K. A. Transesterification of a Phosphate Diester by Divalent and Trivalent Metal Ions. *Inorg. Chem.* **1992**, *31* (1), 16–20.
- (52) Bünzli, J. G. .; Choppin, G. R.; Cotton, S.; Bünzli, J. G. .; Choppin, G. R. Lanthanide Probes in Life, Chemical and Earth Sciences Theory and Practice. *Spectrochim. Acta Part A Mol. Spectrosc.* **1990**, *46* (12), 1797.
- (53) Aspinall, H. C. Chiral Lanthanide Complexes: Coordination Chemistry and Applications. *Chem. Rev.* **2002**, *102* (6), 1807–1850.
- (54) Bünzli, J.-C. G. Benefiting from the Unique Properties of Lanthanide Ions. *Acc. Chem. Res.* **2006**, *39* (1), 53–61.
- (55) Mejía-Radillo, Y.; Yatsimirsky, A. K. Complex Formation and Kinetics of Phosphodiester Cleavage in the Hydrogen Peroxide-Lanthanide(III) System. *Inorganica Chim. Acta* **2003**, *351* (1), 97–106.
- (56) Takasaki, B. K.; Chin, J. La(III)-Hydrogen Peroxide Cooperativity in Phosphate Diester Cleavage: A Mechanistic Study. *J. Am. Chem. Soc.* **1995**, *117* (33), 8582–8585.
- (57) Takasaki, B. K.; Chin, J. Synergistic Effect between La(III) and Hydrogen Peroxide in Phosphate Diester Cleavage. *J. Am. Chem. Soc.* **1993**, *115* (20), 9337–9338.
- (58) Molenveld, P.; Engbersen, J. F. J.; Reinhoudt, D. N. Dinuclear Metallo-Phosphodiesterase Models: Application of Calix[4]Arenes as Molecular Scaffolds. *Chem. Soc. Rev.* **2000**, *29* (2), 75–86.
- (59) Ott, R.; Krämer, R. Rapid Phosphodiester Hydrolysis by Zirconium (IV). *Angew. Chem. Int. Ed. Engl.* **1998**, *297* (88), 1957–1960.
- (60) Oh, S. J.; Choi, Y.; Hwangbo, S.; Bae, S. C.; Ku, J. K.; Park, J. W. Structure and Phosphodiesterase Activity of Bis-Tris Coordinated Lanthanide (III) Complexes. *Chem. Commun.* **1998**, *515* (14), 2189–2190.
- (61) Gómez-Tagle, P.; Yatsimirsky, A. K. Kinetics of Phosphodiester Hydrolysis by Lanthanide Ions in Weakly Basic Solutions. *J. Chem. Soc. Dalton Trans.* **1998**, *18*, 2957–2959.
- (62) Souza, B. S.; Brandão, T. A. S.; Orth, E. S.; Roma, A. C.; Longo, R. L.; Bunton, C. A.; Nome, F. Hydrolysis of 8-Quinolyl Phosphate Monoester: Kinetic and Theoretical Studies of the Effect of Lanthanide Ions. *J. Org. Chem.* **2009**, *74* (3), 1042–1053.
- (63) Kirk, B. A.; Cusack, C. L.; Laager, E.; Rochlis, E.; Thomas, T.; Cassano, A. G. Mononuclear and Dinuclear Mechanisms for Catalysis of Phosphodiester Cleavage by Alkaline Earth Metal Ions in Aqueous Solution. *J. Inorg. Biochem.* **2010**, *104* (2), 207–210.
- (64) Butcher, W. W.; Westheimer, F. H. The Lanthanum Hydroxide Gel Promoted Hydrolysis of Phosphate Esters. *J. Am. Chem. Soc.* **1955**, *77* (9), 2420–2424.
- (65) Kamitani, J.; Sumaoka, J.; Asanuma, H.; Komiyama, M. Efficient RNA Hydrolysis by Lanthanide (III)–

- Hydrogen Peroxide Combinations . Novel Aggregates as the Catalytic Species. *J. Chem. Soc. Perkin Trans. 2* **1998**, 3, 523–527.
- (66) Takasaki, B.; Chin, J. Synergistic Effect between Lanthanum (III) and Hydrogen Peroxide in Phosphate Diester Cleavage. *J. Am. Chem. Soc.* **1993**, 115 (20), 9337–9338.
- (67) Bodsgard, B. R.; Burstyn, J. N. Silica-Bound Copper (II) Triazacyclononane: A Robust Material for the Heterogeneous Hydrolysis of a Phosphodiester. *Chem. Commun.* **2001**, 647–648.
- (68) Lykourinou-tibbs, V.; Ercan, A.; Ming, L. J. Iron(III)-Chelex Resin Complex as a Prototypical Heterogeneous Catalyst for Phosphodiester Hydrolysis. *Catal. Commun.* **2003**, 4 (10), 549–553.
- (69) Hussain, N.; Joshi, P.; Ali, S. R.; Bhardwaj, V. K. Comparative Structure Activity Relationship for Heterogeneous Phosphatase-like Catalytic Activities of One-Dimensional Cu(II) Coordination Polymers. *RSC Adv.* **2016**, 6 (66), 61528–61535.
- (70) Hanafy, A. I.; Lykourinou-Tibbs, V.; Bisht, K. S.; Ming, L. J. Effective Heterogeneous Hydrolysis of Phosphodiester by Pyridine-Containing Metallopolymers. *Inorganica Chim. Acta* **2005**, 358 (4), 1247–1252.
- (71) Katz, M. J.; Mondloch, J. E.; Totten, R. K.; Park, J. K.; Nguyen, S. T.; Farha, O. K.; Hupp, J. T. Simple and Compelling Biomimetic Metal-Organic Framework Catalyst for the Degradation of Nerve Agent Simulants. *Angew. Chemie - Int. Ed.* **2014**, 53 (2), 497–501.
- (72) Luong, T. K. N.; Mihaylov, T. T.; Absillis, G.; Shestakova, P.; Pierloot, K.; Parac-Vogt, T. N. Phosphate Ester Bond Hydrolysis Promoted by Lanthanide-Substituted Keggin-Type Polyoxometalates Studied by a Combined Experimental and Density Functional Theory Approach. *Inorg. Chem.* **2016**, 55 (19), 9898–9911.
- (73) Gibson, L. T. Mesosilica Materials and Organic Pollutant Adsorption: Part A Removal from Air. *Chem. Soc. Rev.* **2014**, 43 (15), 5163–5172.
- (74) Monnier, A.; Schüth, F.; Huo, Q.; Kumar, D.; Margolese, D.; Maxwell, R. S.; Stucky, G. D.; Krishnamurty, M.; Petroff, P.; Firouzi, A.; et al. Cooperative Formation of Inorganic-Organic Interfaces in the Synthesis of Silicate Mesostructures. *Science* **1993**, 261 (5126), 1299–1303.
- (75) Vallet-Regi, M.; Rámila, A.; Del Real, R. P.; Pérez-Pariente, J. A New Property of MCM-41: Drug Delivery System. *Chem. Mater.* **2001**, 13 (2), 308–311.
- (76) Skorupska, E.; Jeziorna, A.; Paluch, P.; Potrzebowski, M. Ibuprofen in Mesopores of Mobil Crystalline Material 41(MCM-41): A Deeper Understanding. *Mol. Pharm.* **2014**, 11 (5), 1512–1519.
- (77) Anbia, M.; Neyzehdar, M.; Ghaffarinejad, A. Humidity Sensitive Behavior of Fe(NO₃)₃-Loaded Mesoporous Silica MCM-41. *Sensors Actuators, B Chem.* **2014**, 193 (3), 225–229.
- (78) Lin, J.; Zhao, B.; Cao, Y.; Xu, H.; Ma, S.; Guo, M.; Qiao, D.; Cao, Y. Rationally Designed Fe-MCM-41 by Protein Size to Enhance Lipase Immobilization, Catalytic Efficiency and Performance. *Appl. Catal. A Gen.* **2014**, 478, 175–185.
- (79) Meynen, V.; Cool, P.; Vansant, E. F. Verified Syntheses of Mesoporous Materials. *Microporous Mesoporous Mater.* **2009**, 125 (3), 170–223.
- (80) Alothman, Z. A. A Review: Fundamental Aspects of Silicate Mesoporous Materials. *Materials*

- (Basel). **2012**, 5 (12), 2874–2902.
- (81) Burhan, M.; Shahzad, M. W.; Ng, K. C. Energy Distribution Function Based Universal Adsorption Isotherm Model for All Types of Isotherm. *Int. J. Low-Carbon Technol.* **2018**, 13 (3), 292–297.
- (82) Thommes, M.; Kaneko, K.; Neimark, A. V.; Olivier, J. P.; Rodriguez-Reinoso, F.; Rouquerol, J.; Sing, K. S. W. Physisorption of Gases, with Special Reference to the Evaluation of Surface Area and Pore Size Distribution (IUPAC Technical Report). *Pure Appl. Chem.* **2015**, 87 (9–10), 1051–1069.
- (83) Zhao, X. S.; Lu, G. Q. Modification of MCM-41 by Surface Silylation with Trimethylchlorosilane and Adsorption Study. *J. Phys. Chem. B.* **1998**, 102 (9), 1556–1561.
- (84) Barrett, E. P.; Joyner, L. G.; Halenda, P. P. The Determination of Pore Volume and Area Distributions in Porous Substances. I. Computations from Nitrogen Isotherms. *J. Am. Chem. Soc.* **1951**, 73 (1), 373–380.
- (85) Grün, M.; Unger, K. K.; Matsumoto, A.; Tsutsumi, K. Novel Pathways for the Preparation of Mesoporous MCM-41 Materials: Control of Porosity and Morphology. *Microporous Mesoporous Mater.* **1999**, 27 (2–3), 207–216.
- (86) Pasqua, L.; Procopio, A.; Oliverio, M.; Paonessa, R.; Prete, R.; Nardi, M.; Casula, M. F.; Testa, F.; Nagy, J. B. Hybrid MCM-41 Grafted by a General Microwave-Assisted Procedure: A Characterization Study. *J. Porous Mater.* **2013**, 20 (4), 865–873.
- (87) Melo, R. A. A.; Giotto, M. V.; Rocha, J.; Urquieta-González, E. A. MCM-41 Ordered Mesoporous Molecular Sieves Synthesis and Characterization. *Mater. Res.* **1999**, 2 (3), 173–179.
- (88) Luštická, I.; Vrbková, E.; Vyskočilová, E.; Paterová, I.; Červený, L. Acid Functionalized MCM-41 as a Catalyst for the Synthesis of Benzal-1,1-Diacetate. *React. Kinet. Mech. Catal.* **2013**, 108 (1), 205–212.
- (89) Williams, S.; Neumann, A.; Bremer, I.; Su, Y.; Drager, G.; Kasper, C.; Behrens, P. Nanoporous Silica Nanoparticles as Biomaterials: Evaluation of Different Strategies for the Functionalization with Polysialic Acid by Step-by-Step Cytocompatibility Testing. *J. Mater. Sci. Mater. Med.* **2015**, 26 (3), 1–16.
- (90) Feng, X.; Fryxell, G. E.; Wang, L.-Q.; Kim, A. Y.; Liu, J.; Kemner, K. M. Functionalized Monolayers on Ordered Mesoporous Supports. *Science.* **1997**, 276 (5314), 923–926.
- (91) Basu, S. High Enantioselectivity in the Asymmetric Hydrogenation of Ketones by a Supported Pt Nanocatalyst on a Mesoporous Modified MCM-41 Support. *Chinese J. Catal.* **2015**, 36 (4), 634–638.
- (92) Selvaraj, M.; Pandurangan, A.; Seshadri, K. S.; Sinha, P. K.; Lal, K. B. Synthesis, Characterization and Catalytic Application of MCM-41 Mesoporous Molecular Sieves Containing Zn and Al. *Appl. Catal. A Gen.* **2003**, 242 (2), 347–364.
- (93) Kim, J. M.; Kwak, J. H.; Jun, S.; Ryoo, R. Ion Exchange and Thermal Stability of MCM-41. *J. Phys. Chem.* **1995**, 99 (45), 16742–16747.
- (94) Kim, J. M.; Ryoo, R. Disintegration of Mesoporous Structures of MCM-41 and MCM-48 in Water. *Bulletin of the Korean Chemical Society.* 1996, pp 66–68.

- (95) Croissant, J. G.; Fatieiev, Y.; Almalik, A.; Khashab, N. M. Mesoporous Silica and Organosilica Nanoparticles: Physical Chemistry, Biosafety, Delivery Strategies, and Biomedical Applications. *Adv. Healthc. Mater.* **2018**, *7* (4), 1–75.
- (96) Croissant, J. G.; Fatieiev, Y.; Khashab, N. M. Degradability and Clearance of Silicon, Organosilica, Silsesquioxane, Silica Mixed Oxide, and Mesoporous Silica Nanoparticles. *Adv. Mater.* **2017**, *29* (9).
- (97) Soo Choi, H.; Liu, W.; Misra, P.; Tanaka, E.; Zimmer, J. P.; Iyiti Ipe, B.; Bawendi, M. G.; Frangioni, J. V. Renal Clearance of Quantum Dots. *Nat. Biotechnol.* **2007**, *25* (10), 1165–1170.
- (98) Croissant, J. G.; Cattoën, X.; Durand, J.-O.; Wong Chi Man, M.; Khashab, N. M. Organosilica Hybrid Nanomaterials with High Organic Content: Syntheses and Applications of Silsesquioxanes. *Nanoscale* **2016**, *8* (48), 19945–19972.
- (99) Ray, S.; Bhaumik, A.; Pramanik, M.; Mukhopadhyay, C. Covalently Anchored Carboxylic Acid on Uniform Spherical Silica Nanoparticles with Narrow Slit like Mesopores for the Synthesis of Pyrroloacridinones: CuI-Catalyzed Further C(Sp³)–H Oxyfunctionalization for C=O Formation. *RSC Adv.* **2014**, *4* (30), 15441.
- (100) Fontecave, T.; Clément, S.; Thierry, A.; Cédric, B. Chemical Modification As a Versatile Tool for Tuning Stability of Silica Based Mesoporous Carriers in Biologically Relevant Conditions. *Chem. Mater.* **2012**, *24*, 4326–4336.
- (101) Rim, H. P.; Min, K. H.; Lee, H. J.; Jeong, S. Y.; Lee, S. C. PH-Tunable Calcium Phosphate Covered Mesoporous Silica Nanocontainers for Intracellular Controlled Release of Guest Drugs. *Angew. Chemie - Int. Ed.* **2011**, *50* (38), 8853–8857.
- (102) Peng, Y. K.; Liu, C. L.; Chen, H. C.; Chou, S. W.; Tseng, W. H.; Tseng, Y. J.; Kang, C. C.; Hsiao, J. K.; Chou, P. T. Antiferromagnetic Iron Nanocolloids: A New Generation in Vivo T1mri Contrast Agent. *J. Am. Chem. Soc.* **2013**, *135* (49), 18621–18628.
- (103) Peng, Y.-K.; Tseng, Y.-J.; Liu, C.-L.; Chou, S.-W.; Chen, Y.-W.; Tsang, S. C. E.; Chou, P.-T. One-Step Synthesis of Degradable T₁-FeOOH Functionalized Hollow Mesoporous Silica Nanocomposites from Mesoporous Silica Spheres. *Nanoscale* **2015**, *7* (6), 2676–2687.
- (104) Omar, H.; Croissant, J. G.; Alamoudi, K.; Alsaiani, S.; Alradwan, I.; Majrashi, M. A.; Anjum, D. H.; Martins, P.; Laamarti, R.; Eppinger, J.; et al. Biodegradable Magnetic Silica@Iron Oxide Nanovectors with Ultra-Large Mesopores for High Protein Loading, Magnetothermal Release, and Delivery. *J. Control. Release* **2017**, *259* (November), 187–194.
- (105) Physical Chemistry - American Chemical Society
<https://www.acs.org/content/acs/en/careers/college-to-career/areas-of-chemistry/physical-chemistry.html> (accessed Sep 27, 2018).
- (106) Fogler, S. External Diffusion Effects on Heterogeneous Reactions. In *Chemical Engineering*; 2008; pp 757–811.
- (107) Collard, X.; Li, L.; Lueangchaichaweng, W.; Bertrand, A.; Aprile, C.; Pescarmona, P. P. Ga-MCM-41 Nanoparticles: Synthesis and Application of Versatile Heterogeneous Catalysts. *Catal. Today* **2014**,

- 235, 184–192.
- (108) Andrea, T.; Neverov, A. A.; Brown, R. S. Efficient Methanolytic Cleavage of Phosphate, Phosphonate, and Phosphonothioate Esters Promoted by Solid Supported Lanthanide Ions. *Ind. Eng. Chem. Res.* **2010**, *49* (15), 7027–7033.
- (109) Rimsza, J. M.; Du, J. Nanoporous Silica Gel Structures and Evolution from Reactive Force Field-Based Molecular Dynamics Simulations. *npj Mater. Degrad.* **2018**, *2* (1), 18.
- (110) Renou, R.; Szymczyk, A.; Ghoufi, A. Water Confinement in Nanoporous Silica Materials. *J. Chem. Phys.* **2014**, *140* (4).
- (111) Ohkubo, T.; Gin, S.; Collin, M.; Iwadate, Y. Molecular Dynamics Simulation of Water Confinement in Disordered Aluminosilicate Subnanopores. *Sci. Rep.* **2018**, *8* (1), 1–11.
- (112) Asay, D. B.; Kim, S. H. Evolution of the Adsorbed Water Layer Structure on Silicon Oxide at Room Temperature. *J. Phys. Chem. B* **2005**, *109* (35), 16760–16763.
- (113) Pham, A. L. T.; Sedlak, D. L.; Doyle, F. M. Dissolution of Mesoporous Silica Supports in Aqueous Solutions: Implications for Mesoporous Silica-Based Water Treatment Processes. *Appl. Catal. B Environ.* **2012**, *126*, 258–264.
- (114) Gin, S.; Guittonneau, C.; Godon, N.; Neff, D.; Rebiscoul, D.; Cabí, M.; Mostefaoui, S. Nuclear Glass Durability: New Insight into Alteration Layer Properties. *J. Phys. Chem. C* **2011**, *115* (38), 18696–18706.
- (115) Bodsgard, B. R.; Clark, R. W.; Ehrbar, A. W.; Burstyn, J. N. Silica-Bound Copper(II)Triazacyclononane as a Phosphate Esterase: Effect of Linker Length and Surface Hydrophobicity. *Dalt. Trans.* **2009**, 2365–2373.
- (116) Duncan, C. T.; Flitsch, S.; Asefa, T. Aminotroponimate-Zinc Complex-Functionalized Mesoporous Materials: Efficient and Recyclable Intramolecular Hydroamination Catalysts. *ChemCatChem* **2009**, *1* (3), 365–368.
- (117) Landau, M. V.; Varkey, S. P.; Herskowitz, M.; Regev, O.; Pevzner, S.; Sen, T.; Luz, Z. Wetting Stability of Si-MCM-41 Mesoporous Material in Neutral, Acidic and Basic Aqueous Solutions. *Microporous Mesoporous Mater.* **1999**, *33* (1–3), 149–163.
- (118) Varache, M.; Bezverkhy, I.; Bouyer, F.; Chassagnon, R.; Baras, F.; Bouyer, F. Improving Structural Stability of Water-Dispersed MCM-41 Silica Nanoparticles through Post-Synthesis PH Aging Process. *J. Nanoparticle Res.* **2015**, *17* (9).
- (119) Avrami, M. Kinetics of Phase Change. I: General Theory. *J. Chem. Phys.* **1939**, *7* (12), 1103–1112.
- (120) Avrami, M. Kinetics of Phase Change. II - Transformation-Time Relations for Random Distribution of Nuclei. *J. Chem. Phys.* **1940**, *8* (1940), 212–224.
- (121) Avrami, M. Granulation, Phase Change, and Microstructure Kinetics of Phase Change. III. *J. Chem. Phys.* **1941**, *9* (2), 177–184.
- (122) Li, X.; Yin, X.; Zhang, L.; He, S. The Devitrification Kinetics of Silica Powder Heat-Treated in Different Conditions. *J. Non. Cryst. Solids* **2008**, *354* (28), 3254–3259.
- (123) Liu, F.; Sommer, F.; Bos, C.; Mittemeijer, E. J. Analysis of Solid State Phase Transformation Kinetics:

- Models and Recipes. *Int. Mater. Rev.* **2007**, *52* (4), 193–212.
- (124) Finney, E. E.; Finke, R. G. Is There a Minimal Chemical Mechanism Underlying Classical Avrami-Erofe'ev Treatments of Phase-Transformation Kinetic Data. *Chem. Mater.* **2009**, *21* (19), 4692–4705.
- (125) Buntun, C. A.; Farber, S. J. The Hydrolysis of Bis (2,4-Dinitrophenyl) Phosphate. *J. Org. Chem.* **1969**, *34* (4), 767–772.
- (126) Amaya, C. A.; Joel, I.; Nascentes, C. C.; Denadai, Â. M. L.; Helena, M.; Brandão, T. A. S. Phosphate Ester Cleavage by a Positively Charged Porous Silica Adorned with Lanthanum (III). *Microporous Mesoporous Mater.* **2018**, *268*, 144–152.
- (127) XRD1 – LNLS <https://www.lnls.cnpem.br/linhas-de-luz/xrd1-en/overview/> (accessed Dec 2, 2018).
- (128) Ribeiro-Santos, T. A.; Henriques, F. F.; Villarroel-Rocha, J.; de Castro, M. C. M.; Magalhães, W. F.; Windmüller, D.; Sapag, K.; Lago, R. M.; Araujo, M. H. Hydrophobic Channels Produced by Micelle-Structured CTAB inside MCM-41 Mesopores: A Unique Trap for the Hazardous Hormone Ethinyl Estradiol. *Chem. Eng. J.* **2016**, *283*, 1203–1209.
- (129) Vunain, E.; Opembe, N. N.; Jalama, K.; Mishra, A. K.; Meijboom, R. Thermal Stability of Amine-Functionalized MCM-41 in Different Atmospheres. *J. Therm. Anal. Calorim.* **2014**, *115* (2), 1487–1496.
- (130) Fellenz, N.; Martin, P.; Marchetti, S.; Bengoa, F. Aminopropyl-Modified Mesoporous Silica Nanospheres for the Adsorption of Cr(VI) from Water. *J. Porous Mater.* **2015**, *22* (3), 729–738.
- (131) Zhao, X. S.; Lu, G. Q.; Whittaker, a K.; Millar, G. J.; Zhu, H. Y. Comprehensive Study of Surface Chemistry of MCM-41 Using Si-29 CP/MAS NMR, FTIR, Pyridine-TPD, and TGA. *J. Phys. Chem. B* **1997**, *101* (33), 6525–6531.
- (132) Klockenkämper, R.; Von Bohlen, A. Total-Reflection X-Ray Fluorescence Moving towards Nanoanalysis: A Survey. *Spectrochim. Acta - Part B At. Spectrosc.* **2001**, *56* (11), 2005–2018.
- (133) Towett, E. K.; Shepherd, K. D.; Cadisch, G. Quantification of Total Element Concentrations in Soils Using Total X-Ray Fluorescence Spectroscopy (TXRF). *Sci. Total Environ.* **2013**, *463–464*, 374–388.
- (134) Brunauer, S.; Emmett, P. H.; Teller, E. Adsorption of Gases in Multimolecular Layers. *J. Am. Chem. Soc.* **1938**, *60* (1), 309–319.
- (135) Suganuma, T. Measurement of Surface Topography Using SEM with Two Secondary Electron Detectors. *J. Electron Microsc. (Tokyo)*. **1986**, *34* (4), 328–337.
- (136) Joy, D. C.; Prasad, M. S.; Meyer, H. M. Experimental Secondary Electron Spectra under SEM Conditions. *J. Microsc.* **2004**, *215* (1), 77–85.
- (137) Mokhonoana, M. P.; Coville, N. J. Synthesis of [Si]-MCM-41 from TEOS and Water Glass: The Water Glass-Enhanced Condensation of TEOS under Alkaline Conditions. *J. Sol-Gel Sci. Technol.* **2010**, *54* (1), 83–92.
- (138) Meléndez-Ortiz, H. I.; Perera-Mercado, Y.; Mercado-Silva, J. A.; Olivares-Maldonado, Y.; Castruita, G.; García-Cerda, L. A. Functionalization with Amine-Containing Organosilane of Mesoporous Silica MCM-41 and MCM-48 Obtained at Room Temperature. *Ceram. Int.* **2014**, *40*, 9701–9707.

- (139) Talavera-Pech, W. A.; Esparza-Ruiz, A.; Quintana-Owen, P.; Vilchis-Nestor, A. R.; Carrera-Figueiras, C.; Ávila-Ortega, A. Effects of Different Amounts of APTES on Physicochemical and Structural Properties of Amino-Functionalized MCM-41-MSNs. *J. Sol-Gel Sci. Technol.* **2016**, *80* (3), 697–708.
- (140) Abe, T. Electronic Spectra of Polynitrophenols and Their Anions. *Bull. Chem. Soc. Jpn.* **1962**, *35* (2), 318–322.
- (141) Diez-Castellnou, M.; Mancin, F.; Scrimin, P. Efficient Phosphodiester Cleaving Nanozymes Resulting from Multivalency and Local Medium Polarity Control. *J. Am. Chem. Soc.* **2014**, *136* (4), 1158–1161.
- (142) McKay, C. S.; Finn, M. G. Polyvalent Catalysts Operating on Polyvalent Substrates: A Model for Surface-Controlled Reactivity. *Angew. Chemie - Int. Ed.* **2016**, *55* (41), 12643–12649.
- (143) Bünzli, J. C. G.; Piguet, C. Lanthanide-Containing Molecular and Supramolecular Polymetallic Functional Assemblies. *Chem. Rev.* **2002**, *102* (6), 1897–1928.
- (144) Jencks, W. P. Binding Energy, Specificity, and Enzymic Catalysis: The Circe Effect. *Adv. Enzymol. Relat. Areas Mol. Biol.* **1975**, *43*, 219–410.
- (145) Williams, F. L.; Baron, K. Lead, Sulfur and Phosphorus Interactions with Platinum and Palladium Metal Foils. *J. Catal.* **1975**, *40* (1), 108–116.
- (146) Angelé, B.; Kirchner, K. The Poisoning of Noble Metal Catalysts by Phosphorus Compounds-I. *Chem. Eng. Sci.* **1979**, *35*, 2089–2091.
- (147) He, Q.; Shyam, B.; Nishijima, M.; Ramaker, D.; Mukerjee, S. Mitigating Phosphate Anion Poisoning of Cathodic Pt/C Catalysts in Phosphoric Acid Fuel Cells. *J. Phys. Chem. C.* **2013**, *117* (10), 4877–4887.
- (148) Pan, Y.; Shen, X.; Yao, L.; Bentalib, A.; Peng, Z. Active Sites in Heterogeneous Catalytic Reaction on Metal and Metal Oxide : Theory and Practice. *Catalysts* **2018**, *8*, 478–498.
- (149) Jinschek, J. R. Atomic Scale Structure-Function Relationship of Heterogeneous Catalysts: Investigation of Gas-Solid Interactions by ETEM. *Microsc. Microanal.* **2012**, No. November, 5–10.
- (150) Marler, B.; Oberhagemann, U.; Vortmann, S.; Gies, H. Influence of the Sorbate Type on the XRD Peak Intensities of Loaded MCM-41. *Microporous Mater.* **1996**, *6* (5–6), 375–383.
- (151) Faulkner, R. A.; DiVerdi, J. A.; Yang, Y.; Kobayashi, T.; Maciel, G. E. The Surface of Nanoparticle Silicon as Studied by Solid-State NMR. *Materials (Basel)*. **2013**, *6* (1), 18–46.
- (152) Zhang, X.; Neiner, D.; Wang, S.; Louie, A. Y.; Kauzlarich, S. M. A New Solution Route to Hydrogen-Terminated Silicon Nanoparticles: Synthesis, Functionalization and Water Stability. *Nanotechnology*. **2007**, *18* (9).
- (153) Klauser, F.; Stijepovic, R.; Endstrasser, N.; Jaksch, S.; Memmel, N.; Scheier, P. Oxidation Study of Silicon Nanoparticle Thin Films on HOPG. *Surf. Sci.* **2009**, *603* (19), 2999–3004.
- (154) Khan, Z. H. Electrical and Optical Properties of Thin Film of Amorphous Silicon Nanoparticles. *Appl. Surf. Sci.* **2009**, *255* (21), 8874–8878.
- (155) Zhu, Y.; Wang, H.; Ong, P. P. Preparation and Thermal Stability of Silicon Nanoparticles. *Appl. Surf. Sci.* **2001**, *171* (1–2), 44–48.

- (156) Kuzmin, P. G.; Shafeev, G. A.; Bukin, V. V.; Garnov, S. V.; Farcau, C.; Carles, R.; Warot-Fontrose, B.; Guieu, V.; Viau, G. Silicon Nanoparticles Produced by Femtosecond Laser Ablation in Ethanol: Size Control, Structural Characterization, and Optical Properties. *J. Phys. Chem. C* **2010**, *114* (36), 15266–15273.
- (157) Chen, C. Y.; Xiao, S. Q.; Davis, M. E. Studies on Ordered Mesoporous Materials III. Comparison of MCM-41 to Mesoporous Materials Derived from Kanemite. *Microporous Mater.* **1995**, *4* (1), 1–20.
- (158) Popova, M.; Szegedi, A.; Yoncheva, K.; Konstantinov, S.; Petrova, G. P.; Aleksandrov, H. A.; Vayssilov, G. N.; Shestakova, P. New Method for Preparation of Delivery Systems of Poorly Soluble Drugs on the Basis of Functionalized Mesoporous MCM-41 Nanoparticles. *Microporous Mesoporous Mater.* **2014**, *198*, 247–255.
- (159) Zhao, X. S.; Audsley, F.; Lu, G. Q. Irreversible Change of Pore Structure of MCM-41 upon Hydration at Room Temperature. *J. Phys. Chem. B* **1998**, *102* (21), 4143–4146.
- (160) Lowry, G. V.; Hill, R. J.; Harper, S.; Rawle, A. F.; Hendren, C. O.; Klaessig, F.; Nobbmann, U.; Sayre, P.; Rumble, J. Guidance to Improve the Scientific Value of Zeta-Potential Measurements in NanoEHS. *Environ. Sci. Nano* **2016**, *3* (5), 953–965.
- (161) Taylor, H. S. A Theory of the Catalytic Surface. *Proc. R. Soc. London A* **1925**, *15* (108), 105–111.
- (162) Diagboya, P. N. E.; Dikio, E. D. Silica-Based Mesoporous Materials; Emerging Designer Adsorbents for Aqueous Pollutants Removal and Water Treatment. *Microporous Mesoporous Mater.* **2018**, *266* (November 2017), 252–267.
- (163) Weale, K. E. Liquid-Phase Reactions at High Pressures. Part VIII.* The Kinetics of an “Ortho-Effect” Reaction at High Pressures. *J. Chem. Soc.* **1952**, *0*, 2959–2962.
- (164) Avnir, D.; Gutfraind, R.; Farin, D. Fractal Analysis in Heterogeneous Chemistry. In *Fractals in Science*; Springer Berlin Heidelberg: Berlin, Heidelberg, 1994; pp 229–256.
- (165) Narayan, R.; Nayak, U. Y.; Raichur, A. M.; Garg, S. Mesoporous Silica Nanoparticles: A Comprehensive Review on Synthesis and Recent Advances. *Pharmaceutics* **2018**, *10* (3), 1–49.
- (166) Mehmood, A.; Ghafar, H.; Yaqoob, S.; Gohar, U. F.; Ahmad, B. Mesoporous Silica Nanoparticles: A Review. *J. Dev. Drugs* **2017**, *06* (02).
- (167) Newman, C. M.; Stein, D. L. Metastate Approach to Thermodynamic Chaos. *Phys. Rev. E - Stat. Physics, Plasmas, Fluids, Relat. Interdiscip. Top.* **1997**, *55* (5), 5194–5211.
- (168) Fan, L. S. Summary Paper on Fluidization and Transport Phenomena. *Powder Technol.* **1996**, *88* (3), 245–253.
- (169) Petrov, L. A.; Alhamed, Y.; Daous, M.; Catalysis, S.; Box, P. O.; Arabia, S. Role of Chemical Kinetics in the Heterogeneous Catalysis Studies. *Chinese J. Catal.* **2011**, *32* (7).
- (170) Plonka, A. Dispersive Kinetics. *Annual Reports on the Progress of Chemistry - Section C*. Springer Netherlands 2001, pp 91–147.
- (171) Yang, S. M.; Yang, H.; Coombs, N.; Sokolov, I.; Kresge, C. T.; Ozin, G. a. Morphokinetics: Growth of Mesoporous Silica Curved Shapes. *Adv. Mater.* **1999**, *11* (1), 52–55.
- (172) Clark, I. D.; Harrison, L. G.; Kondretiev, V. N.; Szabó, Z. G.; Wayne, R. P. *Comprehensive Chemical*

- Kinetics - V02 The Theory of Kinetics*, First Edit.; Bamford, C. H., Tipper, C. F. H., Eds.; Elsevier B.V: New York, 1969; Vol. 2.
- (173) Yablonskii, G.; Bykov, V.; Gorban, A.; Elokhin, V. *Comprehensive Chemical Kinetics - V32 Kinetic Models of Catalytic Reactions*, First edit.; Compton, R. G., Ed.; Elsevier B.V: New York, 1991.
- (174) Ball, D. Kinetics of Consecutive Reactions: First Reaction, First-Order; Second Reaction, Zeroth Order. *J. Chem. Educ.* **1998**, *75* (7), 917.
- (175) Irzhak, T. F.; Mezhikovskii, S. M.; Irzhak, V. I. The Physical Meaning of the Avrami Equation in Oligomer Curing Reactions. *Polym. Sci. Ser. B* **2008**, *50* (7–8), 201–203.
- (176) Khanna, Y. P.; Taylor, T. J. Comments and Recommendations on the Use of the Avrami Equation for Physico-Chemical Kinetics. *Polym. Eng. Sci.* **1988**, *28* (16), 1042–1045.
- (177) Elazazy, M. S.; Issa, A. A.; Al-Mashreky, M.; Al-Sulaiti, M.; Al-Saad, K. Application of Fractional Factorial Design for Green Synthesis of Cyano-Modified Silica Nanoparticles: Chemometrics and Multifarious Response Optimization. *Adv. Powder Technol.* **2018**, *29* (5), 1204–1215.
- (178) Bahrami, Z.; Badieli, A.; Ziarani, G. M. Carboxylic Acid-Functionalized SBA-15 Nanorods for Gemcitabine Delivery. *J. Nanoparticle Res.* **2015**, *17* (3).
- (179) Yu, X.; Yu, X.; Wu, S.; Liu, B.; Liu, H.; Guan, J.; Kan, Q. The Effect of the Distance between Acidic Site and Basic Site Immobilized on Mesoporous Solid on the Activity in Catalyzing Aldol Condensation. *J. Solid State Chem.* **2011**, *184* (2), 289–295.
- (180) Luxbacher, T. *The Zeta Potential for Solid Surface Analysis - A Practical Guide to Streaming Potential Measurement*, First Edit.; Anton Paar: Graz, 2014.
- (181) Stumm, W.; Morgan, J. J. *Aquatic Chemistry : Chemical Equilibria and Rates in Natural Waters*; Wiley, 1996.
- (182) Xu, J.; Zhou, M. Reactions of Early Lanthanide Metal Atoms (Nd, Sm, Eu) with Water Molecules. A Matrix Isolation Infrared Spectroscopic and Theoretical Study. *J. Phys. Chem. A* **2006**, *110* (36), 10575–10582.
- (183) Bentouhami, E.; Bouet, G. M.; Meullemeestre, J.; Vierling, F.; Khan, M. A. Physicochemical Study of the Hydrolysis of Rare-Earth Elements (III) and Thorium (IV). *Comptes Rendus Chim.* **2004**, *7* (5), 537–545.
- (184) Bentouhami, E.; Bouet, G. M.; Khan, M. A. A Comparison of the Acidity and the Complexing Ability of (o-Hydroxyphenyl) Bis- and (o-Hydroxyphenyl) Mono-Methylenephosphonic Acids towards Lanthanide(III) Ions. *Talanta* **2002**, *57* (3), 545–554.